JGR Planets

RESEARCH ARTICLE
10.1029/2022JE007700

Poroviscoelastic Gravitational Dynamics

S. Kamata[1]

[1]Department of Earth and Planetary Sciences, Hokkaido University, Sapporo, Japan

Key Points:

- The theory for periodic deformation of a planetary body with a global, fluid-saturated porous layer is established
- The procedure to make numerical calculations accurate and stable is given
- The importance of the direct calculation of the fluid flow and that of the radial porosity profile are demonstrated

Correspondence to:
S. Kamata,
kamata@sci.hokudai.ac.jp

Citation:
Kamata, S. (2023). Poroviscoelastic gravitational dynamics. *Journal of Geophysical Research: Planets*, *128*, e2022JE007700. https://doi.org/10.1029/2022JE007700

Received 30 NOV 2022
Accepted 6 JUL 2023

Abstract Global-scale periodic deformation has been studied using the (visco)elastic gravitational theory, which assumes a planetary body consists of solid or liquid layers. Recent planetary exploration missions, however, suggest that a global layer of a mixture of solid and liquid exists in several planetary bodies. This study provides a theory of periodic deformation of such a layer unifying the viscoelastic gravitational theory with the theory of poroelasticity without introducing additional constraints. The governing equation system and a formulation suitable for numerical calculation are given. Equations used to calculate the energy dissipation rate are also given. The analytical solutions for a homogeneous sphere are obtained using an eigenvalue approach. Simple numerical calculations assuming a homogeneous sphere reveal that a numerical instability occurs if a thick porous layer, a low permeability, or a high frequency is assumed. This instability can be avoided by choosing an appropriate interior structure model that is numerically equivalent. Different simple numerical calculations adopting a multilayered, radially varying interior profile reveal that the radial profile of the tidal heating rate for a fluid-saturated porous layer and that for a low-viscosity solid layer are completely different. In addition, the radial variation in porosity can lead to a factor of ∼100 increase in the local heating rate. These results indicate that future studies should consider a wider variety of detailed interior structure models.

Plain Language Summary Global periodic deformations, such as tidal and seismic motions, are fundamental phenomena that have been studied for a long time. While planetary exploration missions suggest the presence of solid-liquid mixed layers in solar system bodies, a comprehensive theory describing deformation of such a layer has not been established. In this study, a classic geophysical approach and a classic engineering approach are unified to investigate the dynamics of such a layer. A full set of equations as well as analytical solutions are derived. A numerical issue that is likely to be encountered under typical calculation conditions is discussed. A simple calculation assuming tides on the Saturnian satellite Enceladus indicates that the radial variation in porosity can lead to a significant increase in the tidal heating rate in a shallow part of the water-saturated rocky core. The theory established in this study will be valuable for future detailed studies.

1. Introduction

Large-scale deformation is the fundamental dynamics of planetary bodies and is related to many geophysical subjects. Because of its high importance, this deformation has been studied for a long time; the governing equation system and its analytical solution for a homogeneous sphere have already been obtained more than a century ago (Love, 1911), and reformulations more suitable for numerical calculations have also been determined decades ago (e.g., Alterman et al., 1959; Pekeris & Jarosch, 1958; Takeuchi & Saito, 1972). In those studies, a spherically symmetric, nonrotating, elastic, and isotropic (SNREI) Earth model was adopted. This "elastic gravitational theory" can be applied to various types of studies considering seismic frequencies and static deformation (i.e., zero frequency). To describe geophysical phenomena with intermediate timescales, viscoelasticity should be taken into account. The "viscoelastic gravitational theory" adopting a spherically symmetric, nonrotating, viscoelastic, and isotropic (SNRVEI) model has also been applied to various types of studies, including the tidal response of natural satellites (e.g., Harada et al., 2014; Kamata et al., 2015; Tobie et al., 2005).

The tidal response of natural satellites is a major subject in planetary science. A well-known example is the heat budget of a small icy satellite, Enceladus. Cassini observations have revealed that the satellite is very hot; heat flux from its south pole region is very high (Howett et al., 2011; Spencer et al., 2006), and a thick global subsurface ocean exists (e.g., Thomas et al., 2016). Because accretional heating, radiogenic heating, and heating due to chemical reactions would be much smaller than the measured value, tidal heating plays an important role in the heat budget of this small icy satellite (e.g., Roberts & Nimmo, 2008; Travis & Schubert, 2015). If one adopts a simple model in which the satellite is composed of a less viscous pure H_2O outer shell and a highly

viscous monolithic rocky core, tidal heating is expected to occur not in the rocky core but in the ice shell (e.g., Roberts, 2015; Roberts & Nimmo, 2008). However, measurements of plume constituents suggest ongoing hydrothermal activities (Hsu et al., 2015; Waite et al., 2017), indicating heating in the core. This observation could be explained if the core is fragmented and thus highly dissipative (e.g., Choblet et al., 2017; Roberts, 2015). Because the core is overlain by a subsurface ocean, the core can be considered a mixture of rock and water. In fact, such a core model is supported by a low effective density of the core suggested from geodetic measurements (e.g., Čadek et al., 2016; Hemingway & Mittal, 2019; Thomas et al., 2016).

The presence of a layer that is a mixture of solid and liquid is also proposed for other satellites. Specifically, an unusual dependency of the tidal response of the Moon on frequency is explained by the presence of a partially molten layer at the base of the mantle (Harada et al., 2014). Also, the electromagnetic induction response of Io is explained by the presence of a global partially molten subsurface layer (Khurana et al., 2011), and this layer is expected to provide additional heating due to volumetric expansion/contraction (Kervazo et al., 2021). Because the viscoelastic gravitational theory cannot address a solid-fluid mixed layer directly, a phenomenological approach has been adopted; a fluid-saturated porous layer is modeled as a purely solid layer that has an extremely low effective viscosity or quality factor. Such an approach limits our understanding of the nature of a solid-liquid mixed layer.

An innovative, physics-based approach that directly models a solid-fluid mixed layer was proposed by Liao et al. (2020). Using the classic theory of poroelasticity originally developed by Biot (1941), they calculate the permeable flow of pore fluid in a core and show that such a flow may produce a large amount of heat in the core. Nevertheless, the interior structure model adopted in this study is unrealistic; the porous core is floating in a water-saturated universe. In addition, as pointed out by Rovira-Navarro et al. (2022), the amount of heat due to permeable flow in the core is overestimated due to inappropriate boundary conditions.

The objective of this study is (a) to establish a theory that unifies the classic viscoelastic gravitational theory and the poroelastic theory and (b) to clarify numerical issues one would face when it is applied to geophysical studies. This study provides a general theory; assumptions other than those inherited from classic theories are not introduced as much as possible to maximize the applicability. This approach is fundamentally different from a similar but limited method recently proposed by Rovira-Navarro et al. (2022). Specifically, a low frequency, an extremely high permeability, and uniform layer properties are needed. In addition, the gravitation on the fluid is not incorporated correctly. On the other hand, the theory given in this study is free from such limitations and thus should be applicable not only in studies of tides but also in a wide variety of subjects. For example, an applicability to high frequencies of this theory would be beneficial to seismic studies.

In Section 2, the poroviscoelastic gravitational theory is given; the governing equations, the solutions for the homogeneous sphere, the boundary conditions, and the equations describing the energy dissipation rate (i.e., heating rate) are provided. Section 3 provides some numerical calculations. We first adopt a homogeneous sphere model and investigate the behavior of solutions. We find that a numerical instability occurs under typical parameter conditions. A method to overcome the issue is provided. We then adopt a multilayer model and investigate the effect of radial variation in interior properties. Concluding remarks are offered in Section 4.

2. Theory

2.1. Governing Equation System

The governing equation system consists of (a) a constitutive equation, (b) a Poisson equation of gravity, and (c) an equation of motion (i.e., the dynamic equation). These three equations are solved simultaneously in the case of a nonporous solid. However, in the case of fluid-saturated porous materials, Equations 1 and 3 are given for solid and fluid separately; the equation system now consists of five equations. In the following subsection, we derive Fourier transformed equations that are appropriate to describe periodic motions of fluid-saturated porous materials assuming a time factor of $e^{i\omega t}$, where i is an imaginary number, ω is the frequency of forcing, and t is time, respectively. A replacement of $i\omega$ with a Laplace transform variable s enables one to calculate not periodic but exponentially decaying motions, though this is not investigated in this study. Following Love (1911) and Biot (1956a), the Eulerian formulation is adopted. Below, the summation convention is used (i.e., $\sigma_{kk} = \sigma_{11} + \sigma_{22} + \sigma_{33}$), and positive normal stress and strain indicate tensile (i.e., tensor convention), while positive pressure is compressive.

2.1.1. Constitutive Equation

The constitutive equation of an isotropic porous material with a Maxwellian viscoelasticity is given by (e.g., Liao et al., 2020)

$$\frac{\partial \sigma_{ij}}{\partial t} + \frac{\mu}{\eta_s}\left(\sigma_{ij} - \frac{\sigma_{kk}}{3}\delta_{ij}\right) = \left(K_d - \frac{2}{3}\mu\right)\frac{\partial e^s_{kk}}{\partial t}\delta_{ij} + 2\mu\frac{\partial e^s_{ij}}{\partial t} - \alpha\frac{\partial p_f}{\partial t}\delta_{ij}, \tag{1}$$

where the subscripts i and j indicate the direction, σ_{ij} is the stress tensor, e^s_{ij} is the solid strain tensor, p_f is the pore fluid pressure, μ is the shear modulus of the porous material, η_s is the solid viscosity, K_d is the drained bulk modulus, α is the Biot effective stress coefficient, and δ_{ij} is the unit diagonal tensor, respectively. The Biot effective stress coefficient α is given by

$$\alpha = 1 - \frac{K_d}{K'_s}, \tag{2}$$

where K'_s is the unjacketed frame bulk modulus.

The constitutive equation for the pore fluid is given by Biot and Willis (1957).

$$p_f = -M\left[(\alpha - \phi)e^s_{kk} + \phi e^f_{kk}\right] = -M\left(\alpha e^s_{kk} + \phi e^{\mathrm{rel}}_{kk}\right), \tag{3}$$

where e^f_{kk} is the dilatation of the fluid, $e^{\mathrm{rel}}_{kk} = e^f_{kk} - e^s_{kk}$ is the relative fluid dilatation, ϕ is the porosity, and M is the Biot modulus, respectively. The Biot modulus M is given by Biot & Willis (1957), Cheng (2016), and Rice and Cleary (1976).

$$M = \left(\frac{\alpha}{K'_s} - \frac{\phi}{K''_s} + \frac{\phi}{K_f}\right)^{-1}, \tag{4}$$

where K''_s is the unjacketed pore volume bulk modulus and K_f is the fluid bulk modulus, respectively. It should be noted here that while the pore fluid is assumed to be viscous, the shear stress of the pore fluid is not considered in the framework of classic poroelasticity. As discussed in Section 2.1.3, this is not a self-inconsistency but is appropriate when the macroscopic flow of pore fluid is considered.

The Fourier transforms of Equations 1 and 3 are given by (Equations 10.23 and 10.24 of Cheng, 2016).

$$\widetilde{\sigma}_{ij} = \lambda_c \widetilde{e}^s_{kk}\delta_{ij} + 2\mu_c \widetilde{e}^s_{ij} - \alpha\widetilde{p_f}\delta_{ij}, \tag{5}$$

$$\widetilde{p}_f = -M\left(\alpha\widetilde{e}^s_{kk} + \phi\widetilde{e}^{\mathrm{rel}}_{kk}\right), \tag{6}$$

respectively, where Fourier transformed variables are denoted by a tilde, λ_c is the first Lamé parameter given by

$$\lambda_c = K_d - \frac{2\mu_c}{3}, \tag{7}$$

and μ_c is the second Lamé parameter, or the complex shear modulus, given by

$$\mu_c = \left(\frac{1}{\mu} + \frac{1}{i\omega\eta_s}\right)^{-1}. \tag{8}$$

For planetary applications, detailed material properties are often unknown. In such cases, an assumption that the material is microscopically homogeneous as well as isotropic (i.e., an ideal porous medium) may be used as a first step. In this case, two bulk moduli, K'_s and K''_s, for the solid frame satisfy

$$K'_s = K''_s = K_s, \tag{9}$$

where K_s is the bulk modulus of the solid constituent (e.g., Cheng, 2016). Then, we have the following simplified expressions for poroelastic parameters:

$$\alpha = 1 - \frac{K_d}{K_s}, \tag{10}$$

$$M = \left(\alpha - \phi + \frac{\phi K_s}{K_f}\right)^{-1} K_s. \tag{11}$$

On the other hand, the use of rheological models other than the Maxwell model may be desired. This is possible by simply choosing an appropriate complex shear modulus (i.e., Equation 8). For example, $\mu_c = \mu$ is for a purely (poro)elastic model, and

$$\mu_c = \left(\frac{1}{\mu} + \frac{1}{i\omega\eta_s} + \beta(i\omega)^{-m}\Gamma(m+1)\right)^{-1} \tag{12}$$

is for the Andrade rheology model, where β and m are empirical parameters and $\Gamma(m+1)$ is the Gamma function (e.g., McCarthy & Castillo-Rogez, 2013). In addition, the dissipation due to the volume change in the solid (i.e., "bulk dissipation") can be incorporated by replacing bulk moduli. For example, in the case where the volume change is due to the sliding of particles over each other ignoring the viscoelasticity of the solid grain itself, a replacement of

$$K_d \to \left(\frac{1}{K_d} + \frac{1}{i\omega\eta_b}\right)^{-1} \tag{13}$$

where η_b is the bulk viscosity, can be used for an ideal porous medium (Ch. 10 of Cheng, 2016). In this case, α and M, which are given by Equations 10 and 11, respectively, are also complex numbers. If grain viscoelasticity is considered (i.e., K_s' is a complex number), a more detailed treatment is necessary.

2.1.2. Poisson Equation of Gravity

The Poisson equation of the gravitational potential is given by (e.g., Love, 1911)

$$\frac{\partial^2\psi}{\partial x_i \partial x_i}(r) = 4\pi G\rho(r) \tag{14}$$

where ψ is the gravitational potential, G is the gravitational constant, ρ is the density, and r is the radial distance from the center, respectively. It is noted that this study adopts a general notation where the sign of potential is opposite from classic geophysical studies (e.g., Alterman et al., 1959; Love, 1911; Pekeris & Jarosch, 1958; Takeuchi & Saito, 1972). Consider a small perturbation in gravitational potential and density:

$$\psi(r) = \psi_0(r) + \psi_1(r), \tag{15}$$

$$\rho(r) = \rho_0(r) + \rho_1(r), \tag{16}$$

where subscripts 0 and 1 indicate the hydrostatic equilibrium background state and first-order perturbation, respectively. The perturbation ρ_1 of density is given by the time integration of the continuity equation:

$$\begin{aligned}\rho_1 &= \int \frac{\partial\rho}{\partial t}dt = -\int \frac{\partial}{\partial x_i}\left(\rho_0 \frac{\partial u_i}{\partial t}\right)dt = -\frac{\partial}{\partial x_i}(\rho_0 u_i) \\ &= -\left(u_r \frac{d\rho_0}{dr} + \rho_0 e^s_{kk}\right),\end{aligned} \tag{17}$$

where u_i is the i-direction displacement. The Poisson equation for the first-order perturbation is then given by (e.g., Love, 1911)

$$\frac{\partial^2\psi_1}{\partial x_i \partial x_i} = 4\pi G\rho_1 = -4\pi G\left(u_r \frac{d\rho_0}{dr} + \rho_0 e^s_{kk}\right). \tag{18}$$

For a fluid-saturated solid, these perturbations are decomposed into solid and fluid parts. Specifically, they are given by

$$\frac{\partial^2\psi^s_1}{\partial x_i \partial x_i} = -4\pi G\left(u^s_r \frac{d}{dr}[(1-\phi)\rho_{s0}] + (1-\phi)\rho_{s0} e^s_{kk}\right), \tag{19}$$

$$\frac{\partial^2\psi^f_1}{\partial x_i \partial x_i} = -4\pi G\left(u^f_r \frac{d}{dr}(\phi\rho_{f0}) + \phi\rho_{f0} e^f_{kk}\right), \tag{20}$$

where ψ_1^{ξ} is the first-order perturbation of gravitational potential due to displacement and deformation of the component ξ ($\xi = s$ for solid and $\xi = f$ for fluid), u_r^{ξ} is the radial displacement of the component ξ, $\rho_{\xi 0}$ is the equilibrium density of the component ξ, and ϕ is the porosity (i.e., the volume fraction of fluid), respectively. The total first-order perturbation of gravitational potential is given by the sum of each component:

$$\begin{aligned}\frac{\partial^2 \psi_1}{\partial x_i \partial x_i} &= \frac{\partial^2}{\partial x_i \partial x_i}\left(\psi_1^s + \psi_1^f\right) \\ &= -4\pi G\left(u_r^s \frac{d\rho}{dr} + \rho e_{kk}^s + u_r^{\mathrm{rel}} \frac{d}{dr}(\phi\rho_f) + \phi\rho_f e_{kk}^{\mathrm{rel}}\right).\end{aligned} \tag{21}$$

The Fourier transform of this is given by

$$\frac{\partial^2 \widetilde{\psi}_1}{\partial x_i \partial x_i} = -4\pi G\left(\widetilde{u}_r^s \frac{d\rho}{dr} + \rho \widetilde{e}_{kk}^s + \widetilde{u}_r^{\mathrm{rel}} \frac{d}{dr}(\phi\rho_f) + \phi\rho_f \widetilde{e}_{kk}^{\mathrm{rel}}\right). \tag{22}$$

Here,

$$\rho = (1-\phi)\rho_{s0} + \phi\rho_{f0} \tag{23}$$

is the local mean density, $u_i^{\mathrm{rel}} = u_i^f - u_i^s$ is the i-direction fluid displacement relative to the solid, and the subscript 0 for the density is omitted.

2.1.3. Equation of Motion (Dynamic Equation)

Let us first revisit the derivation of the linearized equation of motion for a nonporous solid. The equation of motion is given by

$$\rho \frac{\partial^2 u_i}{\partial t^2} = \frac{\partial \sigma_{ij}}{\partial x_j} + b_i, \tag{24}$$

where b_i is the i-direction component of the body force. At the hydrostatic equilibrium background state (i.e., $u_i = 0$), Equation 24 becomes

$$0 = \frac{\partial \sigma_{ij,0}}{\partial x_j} + b_{i,0}. \tag{25}$$

Here, the background stress tensor $\sigma_{ij,0}$ and body force $b_{i,0}$ satisfy

$$\sigma_{ij,0} = -p_0 \delta_{ij}, \tag{26}$$

$$b_{i,0} = -\rho_0 \frac{\partial \psi_0(r)}{\partial x_i} = -\rho_0 \frac{x_i}{r}\frac{d\psi_0(r)}{dr} = -\frac{\rho_0 g x_i}{r}, \tag{27}$$

respectively, where $p_0 = p_0(r)$ is the hydrostatic pressure and $g = g(r)(>0)$ is gravitational acceleration. Equations 25–27 yield

$$\frac{dp_0}{dr} = -\rho_0 g. \tag{28}$$

At a perturbed state, the stress tensor σ_{ij} and the body force b_i, including their background states, are given by

$$\sigma_{ij} = -\left(p_0 - u_r \frac{dp_0}{dr}\right)\delta_{ij} + \sigma_{ij,1} \;=\; \sigma_{ij,0} - \rho_0 g u_r \delta_{ij} + \sigma_{ij,1}, \tag{29}$$

$$b_i = -(\rho_0 + \rho_1)\frac{\partial}{\partial x_i}(\psi_0 + \psi_1) \;\approx\; b_{i,0} - \rho_0 \frac{\partial \psi_1}{\partial x_i} + \frac{g x_i}{r} u_r \frac{d\rho_0}{dr} + \frac{\rho_0 g x_i}{r} e_{kk}. \tag{30}$$

Then, the equation of motion for the first-order perturbation can be obtained as

$$\rho \frac{\partial^2 u_i}{\partial t^2} = \frac{\partial \sigma_{ij}}{\partial x_j} - \rho \frac{\partial}{\partial x_i}(g u_r) - \rho \frac{\partial \psi_1}{\partial x_i} + \frac{\rho g x_i}{r} e_{kk}, \tag{31}$$

where the subscript 0 for density and the subscript 1 for stress tensor are omitted.

Now let us derive the equations of motion for the first-order perturbation for a fluid-saturated porous-case in the same manner. In this study, a single-phase isotropic solid frame is assumed to be fully saturated with a single-phase single-component fluid. In this case, the equations of motion for solid and fluid parts are given by (e.g., Biot, 1956a, 1956b; Corapcioglu & Tuncay, 1996; Equations 9.41 and 9.42 of Cheng, 2016).

$$\frac{\partial^2}{\partial t^2}\left[(1-\phi)\rho_{s0}u_i^s-(1-\phi)C_a\rho_{f0}u_i^{\mathrm{rel}}\right]=\frac{\partial}{\partial x_j}\left[(1-\phi)\sigma_{ij}^s\right]+(1-\phi)b_i^s-p_f\frac{\partial\phi}{\partial x_i}+\frac{\phi^2\eta_f}{k}\frac{\partial u_i^{\mathrm{rel}}}{\partial t}, \tag{32}$$

$$\frac{\partial^2}{\partial t^2}\left[\phi\rho_{f0}u_i^f+(1-\phi)C_a\rho_{f0}u_i^{\mathrm{rel}}\right]=-\frac{\partial}{\partial x_i}(\phi p_f)+\phi b_i^f+p_f\frac{\partial\phi}{\partial x_i}-\frac{\phi^2\eta_f}{k}\frac{\partial u_i^{\mathrm{rel}}}{\partial t}, \tag{33}$$

respectively, where σ_{ij}^s is the solid partial stress tensor, b_i^ξ is the i-direction body force acting on component ξ, η_f is the fluid viscosity, k is the intrinsic permeability, and C_a is the porous-medium added-mass coefficient, respectively. The factors of $(1-\phi)$ for solid component variables (i.e., σ_{ij}^s and b_i^s) and of ϕ for fluid component variables (i.e., p_f and b_i^f) are introduced to normalize these variables with the volume of each component.

Compared to the classic geodynamic formulation by Love (1911), the solid-fluid interaction terms have been added to the equation for the solid part (Equation 32), and obviously, the equation for the fluid part (i.e., Equation 33) is newly introduced. The added mass is an apparent mass arising due to the fact that an accelerating or decelerating solid body in a fluid must move a volume of surrounding fluid (e.g., Ch. 9 of Cheng, 2016). It is clear that Equation 32 under the limit of $\phi\to 0$ is equivalent to that used by Love (1911). Equations 32 and 33 can also be compared to a two-phase mantle flow model (McKenzie, 1984), where the terms describing the inertial effects have been ignored. On the other hand, compared to the classic poroelastic formulation by Biot (1956a, 1956b), the terms describing the body forces have been added. In addition, a term with pore pressure has also been added to Equation 32 to allow the spatial variation in porosity.

Equations 32 and 33 yield

$$\rho_0\frac{\partial^2 u_i^s}{\partial t^2}=\frac{\partial\sigma_{ij}}{\partial x_j}+(1-\phi)b_i^s+\phi b_i^f-\phi\rho_{f0}\frac{\partial^2 u_i^{\mathrm{rel}}}{\partial t^2}, \tag{34}$$

$$\frac{\phi^2\eta_f}{k}\frac{\partial u_i^{\mathrm{rel}}}{\partial t}=-\phi\frac{\partial p_f}{\partial x_i}+\phi b_i^f-\phi\rho_{f0}\frac{\partial^2}{\partial t^2}\left[\left(1+\frac{1-\phi}{\phi}C_a\right)u_i^{\mathrm{rel}}+u_i^s\right], \tag{35}$$

where

$$\sigma_{ij}=(1-\phi)\sigma_{ij}^s-\phi p_f\delta_{ij} \tag{36}$$

is the total stress tensor and is given by Equation 1 (Cheng, 2016). Equation 34 describes the bulk motion modified for the relative fluid motion, and Equation 35 is Darcy's flow law modified for the inertial effect. Below, we derive the first-order perturbation components for Equations 34 and 35.

At the hydrostatic equilibrium background state (i.e., $u_i^\xi=0$), Equations 34 and 35 become

$$0=\frac{\partial\sigma_{ij,0}}{\partial x_j}+(1-\phi_0)b_{i,0}^s+\phi_0 b_{i,0}^f, \tag{37}$$

$$0=-\phi_0\frac{\partial p_{f0}}{\partial x_i}+\phi_0 b_{i,0}^f. \tag{38}$$

Here, the total stress tensor $\sigma_{ij,0}$ satisfies Equation 26, and the body force $b_{i,0}^\xi$ is given by

$$b_{i,0}^\xi=-\rho_{\xi0}\frac{\partial\psi_0(r)}{\partial x_i}=-\frac{\rho_{\xi0}gx_i}{r}. \tag{39}$$

In addition, the subscript 0 is added to the porosity. Equations 38 and 39 yield

$$\frac{dp_{f0}(r)}{dr}=-\rho_{f0}g. \tag{40}$$

At a perturbed state,

$$\begin{aligned}\sigma_{ij} &= \sigma_{ij,0} - \left[(1-\phi_0)\rho_{s0}gu_r^s + \phi_0\rho_{f0}gu_r^f\right]\delta_{ij} + \sigma_{ij,1}\\ &= \sigma_{ij,0} - \left(\rho_0 gu_r^s + \phi_0\rho_{f0}gu_r^{\mathrm{rel}}\right)\delta_{ij} + \sigma_{ij,1},\end{aligned} \tag{41}$$

$$\begin{aligned}\phi\frac{\partial p_f}{\partial x_i} &= \left(\phi_0 - \left[u_r^s + (1-\phi_0)u_r^{\mathrm{rel}}\right]\frac{d\phi_0}{dr}\right)\frac{\partial}{\partial x_i}\left(p_{f0} - u_r^f\frac{dp_{f0}}{dr} + p_{f1}\right)\\ &\approx \phi_0\frac{\partial p_{f0}}{\partial x_i} + \frac{\partial}{\partial x_i}\left(\phi_0\rho_{f0}gu_r^f\right) - \frac{\phi_0\rho_{f0}gx_i}{r}u_r^{\mathrm{rel}}\frac{d\phi_0}{dr} + \phi_0\frac{\partial p_{f1}}{\partial x_i},\end{aligned} \tag{42}$$

$$(1-\phi)b_i^s = (1-\phi_0)b_{i,0}^s - (1-\phi_0)\rho_{s0}\frac{\partial\psi_1}{\partial x_i} + \frac{gx_i}{r}u_r^s\frac{d}{dr}[(1-\phi_0)\rho_{s0}] + \frac{(1-\phi_0)\rho_{s0}gx_i}{r}e_{kk}^s, \tag{43}$$

$$\phi b_i^f = \phi_0 b_{i,0}^f - \phi_0\rho_{f0}\frac{\partial\psi_1}{\partial x_i} + \frac{gx_i}{r}u_r^f\frac{d}{dr}(\phi_0\rho_{f0}) + \frac{\phi_0\rho_{f0}gx_i}{r}e_{kk}^f. \tag{44}$$

Here, the factors that change the porosity other than radial displacement are ignored. More specifically,

$$\begin{aligned}\phi &= \frac{\left(V_0^f + V_1^f\right)}{\left(V_0^s + V_1^s\right) + \left(V_0^f + V_1^f\right)} \approx \frac{\phi_0\left(r - u_r^f\right)}{1 - \phi_0(r - u_r^s) + \phi_0\left(r - u_r^f\right)} \approx \frac{\phi_0(r) - u_r^f\frac{d\phi_0}{dr}}{1 + u_r^s\frac{d\phi_0}{dr} - u_r^f\frac{d\phi_0}{dr}}\\ &\approx \phi_0 - \left[u_r^s + (1-\phi_0)u_r^{\mathrm{rel}}\right]\frac{d\phi_0}{dr},\end{aligned} \tag{45}$$

where V^ξ is the volume of the component ξ. Then, we have

$$\rho\frac{\partial^2 u_i^s}{\partial t^2} = \frac{\partial\sigma_{ij}}{\partial x_j} - \rho\frac{\partial}{\partial x_i}(gu_r^s) - \phi\rho_f\frac{\partial}{\partial x_i}\left(gu_r^{\mathrm{rel}}\right) - \rho\frac{\partial\psi_1}{\partial x_i} + \frac{gx_i}{r}\left(\rho e_{kk}^s + \phi\rho_f e_{kk}^{\mathrm{rel}}\right) - \phi\rho_f\frac{\partial^2 u_i^{\mathrm{rel}}}{\partial t^2}, \tag{46}$$

$$\begin{aligned}\frac{\phi\eta_f F_f}{k}\frac{\partial u_i^{\mathrm{rel}}}{\partial t} &= -\frac{\partial p_f}{\partial x_i} - \rho_f\frac{\partial}{\partial x_i}\left[g\left(u_r^{\mathrm{rel}} + u_r^s\right)\right] - \rho_f\frac{\partial\psi_1}{\partial x_i}\\ &\quad + \frac{\rho_f gx_i}{r}\left(u_r^{\mathrm{rel}}\frac{d\phi}{dr} + e_{kk}^{\mathrm{rel}} + e_{kk}^s\right) - \rho_f\frac{\partial^2}{\partial t^2}\left[\left(1 + \frac{1-\phi}{\phi}C_a\right)u_i^{\mathrm{rel}} + u_i^s\right],\end{aligned} \tag{47}$$

and their Fourier transforms are given by

$$-\omega^2\rho\widetilde{u}_i^s = \frac{\partial\widetilde{\sigma}_{ij}}{\partial x_j} - \rho\frac{\partial}{\partial x_i}\left(g\widetilde{u}_r^s\right) - \phi\rho_f\frac{\partial}{\partial x_i}\left(g\widetilde{u}_r^{\mathrm{rel}}\right) - \rho\frac{\partial\widetilde{\psi}_1}{\partial x_i} + \frac{gx_i}{r}\left(\rho\widetilde{e}_{kk}^s + \phi\rho_f\widetilde{e}_{kk}^{\mathrm{rel}}\right) + \omega^2\phi\rho_f\widetilde{u}_i^{\mathrm{rel}}, \tag{48}$$

$$\begin{aligned}i\frac{\omega\phi\eta_f F_f}{k}\widetilde{u}_i^{\mathrm{rel}} &= -\frac{\partial\widetilde{p}_f}{\partial x_i} - \rho_f\frac{\partial}{\partial x_i}\left[g\left(\widetilde{u}_r^{\mathrm{rel}} + \widetilde{u}_r^s\right)\right] - \rho_f\frac{\partial\widetilde{\psi}_1}{\partial x_i}\\ &\quad + \frac{\rho_f gx_i}{r}\left(\widetilde{u}_r^{\mathrm{rel}}\frac{d\phi}{dr} + \widetilde{e}_{kk}^{\mathrm{rel}} + \widetilde{e}_{kk}^s\right) + \omega^2\rho_f\left[\left(1 + \frac{1-\phi}{\phi}C_a\right)\widetilde{u}_i^{\mathrm{rel}} + \widetilde{u}_i^s\right].\end{aligned} \tag{49}$$

Here, the subscript 0 for the density and porosity and the subscript 1 for the stress tensor and pore pressure are omitted. In addition, the fluid viscosity η_f, which appears on the left-hand sides of Equations 47 and 49, is replaced with $\eta_f F_f$, where F_f is the viscosity correction factor (Biot, 1956b; Cheng, 2016). See Appendix A for details of F_f as well as C_a, two parameters that become important when the frequency is high. Equations 46 and 47 correspond to Equations 29a and 29b of Rovira-Navarro et al. (2022) with some additional terms: describing the effects of inertia, of radial variation in porosity, and of gravity on the fluid motion.

In the classic poroelastic formulation, the fluid is assumed to be viscous. In general, the motion of a viscous fluid can be described by the Navier-Stokes equation, which contains a term with the Laplacian of the velocity that originates from shear stress in the fluid. However, Equation 33 does not contain such a term; instead, the fluid viscosity appears in a term linear with the velocity (i.e., the fourth term of the right-hand side), leading to Darcy's law. In other words, shear stress in the fluid is not explicitly incorporated in our formulation, as mentioned in Section 2.1.1. The relation between the Navier-Stokes equation and Darcy's law for porous media has already been investigated in detail, and it is known that the volume averaging of the Navier-Stokes equation

leads to Darcy's law. This indicates that Darcy's law is appropriate to describe the macroscopic motion of the pore fluid (e.g., Neuman, 1977; Whitaker, 1986). It is possible to consider an extension of Darcy's law to include a term with the Laplacian of the velocity (i.e., the Brinkman correction). However, this is appropriate only for fluid-dominated conditions, which is not the case for most geologic material (e.g., Allen, 2021; Auriault, 2009).

2.2. Ordinary Differential Equation System Using y Functions

Periodic spheroidal deformation of a poroviscoelastic planetary body can be calculated by solving Equations 5, 6, 22, 48, and 49. By assuming small amplitudes, deformation due to multiple forcing components can be described as a superposition of deformation due to each component; a spherical harmonic expansion in the spatial domain is applicable. Following Takeuchi and Saito (1972), we define y_i ($i = 1, 2, \ldots, 5$) as follows:

$$\widetilde{u}_i^s = \sum_{\ell,m} U_{\ell m}\left(\frac{x_i}{r} y_1(\ell, r) Y_\ell^m + r y_3(\ell, r)\frac{\partial Y_\ell^m}{\partial x_i}\right), \tag{50}$$

$$\widetilde{\sigma}_{ri} = \sum_{\ell,m} U_{\ell m}\left(\frac{x_i}{r} y_2(\ell, r) Y_\ell^m + r y_4(\ell, r)\frac{\partial Y_\ell^m}{\partial x_i}\right), \tag{51}$$

$$\widetilde{\psi}_1 = -\sum_{\ell,m} U_{\ell m} y_5(\ell, r) Y_\ell^m, \tag{52}$$

where Y_ℓ^m is the unnormalized spherical harmonic function of the degree ℓ and of the order m, and $U_{\ell m}$ is the forcing amplitude of the same degree and order. The minus sign appeared in Equation 52 represents the aforementioned difference in the sign of gravitational potential between geophysical and general conventions. Consequently, y_5 defined by Equation 52 is the same as that defined by Takeuchi and Saito (1972). The unnormalized spherical harmonic function Y_ℓ^m is given by

$$Y_\ell^m(\theta, \varphi) = P_\ell^m(\cos\theta) e^{im\varphi}, \tag{53}$$

where P_ℓ^m is the associated Legendre function, θ is colatitude, and φ is longitude, respectively. It is noted that the y functions are independent of the spherical harmonic order m. We define y_6 after new variables (i.e., y_8, y_9, and y_{10}) are introduced because our y_6 contains one of these new variables.

To describe the motion of the pore fluid (relative to the solid frame), we define $y_8(\ell, r)$, $y_9(\ell, r)$, and $y_{10}(\ell, r)$ as follows:

$$\widetilde{u}_i^{\mathrm{rel}} = \sum_{\ell,m} U_{\ell m}\left(\frac{x_i}{r} y_8(\ell, r) Y_\ell^m + r y_{10}(\ell, r)\frac{\partial Y_\ell^m}{\partial x_i}\right), \tag{54}$$

$$\widetilde{p}_f = \sum_{\ell,m} U_{\ell m} y_9(\ell, r) Y_\ell^m. \tag{55}$$

Equations 54 and 55 are counterparts of Equations 50 and 51, respectively. Equation 55, however, does not contain a term with the partial differential of Y_ℓ^m because shear stress in the fluid does not appear in the governing equation (i.e., Equation 33). It is noted that we do not use y_7 here to avoid confusion with y_7 that has been used by previous studies to describe the motion of a pure liquid layer (Saito, 1974).

Using the newly defined y_8, we define $y_6(r)$ as follows:

$$y_6(r) = \frac{dy_5}{dr} - 4\pi G(\rho y_1 + \phi\rho_f y_8) + \frac{\ell + 1}{r} y_5. \tag{56}$$

Compared to y_6 defined for the nonporous case (e.g., Takeuchi & Saito, 1972), ρy_1, a term accounting for the mass surface density induced by deformation, has been replaced with $\rho y_1 + \phi\rho_f y_8$. This replacement leads to the same boundary conditions for y_6 (i.e., a continuity in y_6 at boundaries).

Substitution of the definitions of y functions to the Fourier transformed governing equations (i.e., Equations 5, 6, 22, 48, and 49) leads to the following eight-component ordinary differential equation system:

$$\frac{dy_1}{dr} = -\frac{2\lambda_c}{(\lambda_c + 2\mu_c)r} y_1 + \frac{1}{\lambda_c + 2\mu_c} y_2 + \frac{\ell(\ell + 1)\lambda_c}{(\lambda_c + 2\mu_c)r} y_3 + \frac{\alpha}{\lambda_c + 2\mu_c} y_9, \tag{57}$$

$$\frac{dy_2}{dr} = \left(-\omega^2\rho - \frac{4\rho g}{r} + \frac{12K_d\mu_c}{(\lambda_c+2\mu_c)r^2} + \frac{\ell(\ell+1)\phi\rho_f^2 g^2}{\omega^2\rho_e r^2}\right)y_1 - \frac{4\mu_c}{(\lambda_c+2\mu_c)r}y_2 + \frac{\ell(\ell+1)}{r}\left[\left(\rho - \frac{\phi\rho_f^2}{\rho_e}\right)g - \frac{6K_d\mu_c}{(\lambda_c+2\mu_c)r}\right]y_3 + \frac{\ell(\ell+1)}{r}y_4 + \frac{\ell+1}{r}\left(\rho - \frac{\ell\phi\rho_f^2 g}{\omega^2\rho_e r}\right)y_5 - \rho y_6 + \left(-\omega^2\phi\rho_f - \frac{4\phi\rho_f g}{r} + \frac{\ell(\ell+1)\phi\rho_f^2 g^2}{\omega^2\rho_e r^2}\right)y_8 + \left(-\frac{4\alpha\mu_c}{(\lambda_c+2\mu_c)r} + \frac{\ell(\ell+1)\phi\rho_f g}{\omega^2\rho_e r^2}\right)y_9, \tag{58}$$

$$\frac{dy_3}{dr} = -\frac{1}{r}y_1 + \frac{1}{r}y_3 + \frac{1}{\mu_c}y_4, \tag{59}$$

$$\frac{dy_4}{dr} = \left[\left(\rho - \frac{\phi\rho_f^2}{\rho_e}\right)\frac{g}{r} - \frac{6K_d\mu_c}{(\lambda_c+2\mu_c)r^2}\right]y_1 - \frac{\lambda_c}{(\lambda_c+2\mu_c)r}y_2 + \left[-\omega^2\left(\rho - \frac{\phi\rho_f^2}{\rho_e}\right) + \frac{2\mu_c}{r^2}\left(\frac{2\ell(\ell+1)(\lambda_c+\mu_c)}{\lambda_c+2\mu_c} - 1\right)\right]y_3 - \frac{3}{r}y_4 - \left(\rho - \frac{\phi\rho_f^2}{\rho_e}\right)\frac{1}{r}y_5 + \left(1 - \frac{\rho_f}{\rho_e}\right)\frac{\phi\rho_f g}{r}y_8 + \left(\frac{2\alpha\mu_c}{\lambda_c+2\mu_c} - \frac{\phi\rho_f}{\rho_e}\right)\frac{1}{r}y_9, \tag{60}$$

$$\frac{dy_5}{dr} = 4\pi G\rho y_1 - \frac{\ell+1}{r}y_5 + y_6 + 4\pi G\phi\rho_f y_8, \tag{61}$$

$$\frac{dy_6}{dr} = \frac{4\pi(\ell+1)G}{r}\left(\rho - \frac{\ell\phi\rho_f^2 g}{\omega^2\rho_e r}\right)y_1 - \frac{4\pi\ell(\ell+1)G}{r}\left(\rho - \frac{\phi\rho_f^2}{\rho_e}\right)y_3 + \frac{4\pi\ell(\ell+1)G\phi\rho_f^2}{\omega^2\rho_e r^2}y_5 + \frac{\ell-1}{r}y_6 + \frac{4\pi(\ell+1)G\phi\rho_f}{r}\left(1 - \frac{\ell\rho_f g}{\omega^2\rho_e r}\right)y_8 - \frac{4\pi\ell(\ell+1)G\phi\rho_f}{\omega^2\rho_e r^2}y_9, \tag{62}$$

$$\frac{dy_8}{dr} = \frac{1}{r}\left(-\frac{4\alpha\mu_c}{\phi(\lambda_c+2\mu_c)} + \frac{\ell(\ell+1)\rho_f g}{\omega^2\rho_e r}\right)y_1 - \frac{\alpha}{\phi(\lambda_c+2\mu_c)}y_2 + \frac{\ell(\ell+1)}{r}\left(\frac{2\alpha\mu_c}{\phi(\lambda_c+2\mu_c)} - \frac{\rho_f}{\rho_e}\right)y_3 - \frac{\ell(\ell+1)\rho_f}{\omega^2\rho_e r^2}y_5 + \left(-\frac{2}{r} + \frac{\ell(\ell+1)\rho_f g}{\omega^2\rho_e r^2}\right)y_8 - \left[\frac{1}{\phi}\left(\frac{1}{M} + \frac{\alpha^2}{\lambda_c+2\mu_c}\right) - \frac{\ell(\ell+1)}{\omega^2\rho_e r^2}\right]y_9, \tag{63}$$

$$\frac{dy_9}{dr} = \left[\omega^2\rho_f + \left(4 - \frac{\ell(\ell+1)\rho_f g}{\omega^2\rho_e r}\right)\frac{\rho_f g}{r}\right]y_1 - \frac{\ell(\ell+1)\rho_f g}{r}\left(1 - \frac{\rho_f}{\rho_e}\right)y_3 \frac{(\ell+1)\rho_f}{r}\left(1 - \frac{\ell\rho_f g}{\omega^2\rho_e r}\right)y_5 + \rho_f y_6 + \left[\omega^2\rho_e + \left(4 - \frac{\ell(\ell+1)\rho_f g}{\omega^2\rho_e r} + r\frac{d\phi}{dr}\right)\frac{\rho_f g}{r} - 4\pi G\rho_f(\rho - \phi\rho_f)\right]y_8 - \frac{\ell(\ell+1)\rho_f g}{\omega^2\rho_e r^2}y_9, \tag{64}$$

where

$$\rho_e = \rho_f\left(1 + \frac{1-\phi}{\phi}C_a\right) - i\frac{\phi\eta_f F_f}{\omega k}, \tag{65}$$

and

$$y_{10} = \frac{1}{\omega^2\rho_e r}\left(\rho_f g y_1 - \omega^2\rho_f r y_3 - \rho_f y_5 + \rho_f g y_8 + y_9\right). \tag{66}$$

See Appendix B1 for the derivation and Appendix C for the differential equation system under some limiting conditions.

While the above equation system is for compressible materials, only slight changes are needed for incompressible materials. Specifically, if the solid (but not the fluid) is incompressible (i.e., $K_s', K_s'' \to \infty$), $\alpha = 1$, and $1/\mathrm{M} = \phi/K_f$. If the fluid (but not the solid) is incompressible (i.e., $K_f \to \infty$), $1/M = \alpha/K_s' - \phi/K_s''$. If both the solid and fluid are incompressible, $\alpha = 1$, and $1/\mathrm{M} = 0$. Thus, material incompressibility does not simplify the equation system largely, which contrasts with the nonporous case, which has $\lambda_c, K_s', K_s'' \to \infty$. This is because the porous

material is compressible (i.e., λ_c and K_d do not diverge) even if the constituent is incompressible unless the undrained condition is applied (e.g., Cheng, 2016; Fjær et al., 2008).

Notably, this equation system is not applicable for static deformation (i.e., $\omega = 0$). Nevertheless, this does not mean that one cannot calculate the static deformation of a porous layer. At $\omega = 0$, if the solid is a Maxwellian material, the porous layer behaves as a pure liquid layer. On the other hand, if the solid is an elastic material (i.e., $\eta_s \to \infty$), the porous layer behaves as an elastic layer with drained moduli. In either case, the system no longer requires an eight-component system and can be solved using a classic method involving either a two- or six-component equation system (Saito, 1974; Takeuchi & Saito, 1972). See Appendix D for further details.

2.3. Solution for the Homogeneous Sphere

Although the deformation of a planetary body with radially varying interior properties is considered, the solution for a homogeneous sphere is important because it is used for the initial values for the numerical integration of the ordinary differential equations of y functions (Takeuchi & Saito, 1972). Love (1911) and Pekeris and Jarosch (1958) provide methods to derive the solution for the homogeneous sphere involving a fourth-order differential equation and the quadratic formula. If the same approach is adopted here, a sixth-order differential equation and a cubic formula will be involved, and this is not practical. Instead, we obtain the solutions adopting an eigenvalue approach.

2.3.1. Compressible Case

Let us define

$$X^s = \frac{dy_1}{dr} + \frac{2}{r}y_1 - \frac{\ell(\ell+1)}{r}y_3, \tag{67}$$

$$Z^s = \frac{dy_3}{dr} + \frac{1}{r}y_3 - \frac{1}{r}y_1, \tag{68}$$

$$X^{\mathrm{rel}} = \frac{dy_8}{dr} + \frac{2}{r}y_8 - \frac{\ell(\ell+1)}{r}y_{10}, \tag{69}$$

$$Z^{\mathrm{rel}} = \frac{dy_{10}}{dr} + \frac{1}{r}y_{10} - \frac{1}{r}y_8, \tag{70}$$

$$\gamma = \frac{g}{r} = \frac{4\pi G\rho}{3}. \tag{71}$$

Then, Equation 48 leads to

$$\left(\mu_c\nabla^2 + \omega^2\rho\right)Z^s + \omega^2\phi\rho_f Z^{\mathrm{rel}} = \gamma\left(\rho X^s + \phi\rho_f X^{\mathrm{rel}}\right), \tag{72}$$

$$\left[\left(\lambda_c + 2\mu_c + \alpha^2 M\right)\nabla^2 + \omega^2\rho + 4\rho\gamma\right]X^s + \phi\left(\alpha M\nabla^2 + \omega^2\rho_f + 4\rho_f\gamma\right)X^{\mathrm{rel}} = \ell(\ell+1)\gamma\left(\rho Z^s + \phi\rho_f Z^{\mathrm{rel}}\right), \tag{73}$$

while Equation 49 leads to

$$\omega^2\left(\rho_f Z^s + \rho_e Z^{\mathrm{rel}}\right) = \rho_f\gamma\left(X^s + X^{\mathrm{rel}}\right), \tag{74}$$

$$\left[\alpha M\nabla^2 + \omega^2\rho_f + 4\rho_f\gamma\right]X^s + \left[\phi M\nabla^2 + \omega^2\rho_e + \left(1 + \frac{3\phi\rho_f}{\rho}\right)\rho_f\gamma\right]X^{\mathrm{rel}} = \ell(\ell+1)\rho_f\gamma\left(Z^s + Z^{\mathrm{rel}}\right). \tag{75}$$

Here,

$$\nabla^2 = \frac{d^2}{dr^2} + \frac{2}{r}\frac{d}{dr} - \frac{\ell(\ell+1)}{r^2}. \tag{76}$$

See Appendix B2 for the derivation. After eliminating Z^{rel} using Equation 74, Equations 72, 73, and 75 can be written in a matrix form:

$$\nabla^2\begin{pmatrix} X^s \\ Z^s \\ X^{\mathrm{rel}} \end{pmatrix} = A\begin{pmatrix} X^s \\ Z^s \\ X^{\mathrm{rel}} \end{pmatrix} = \begin{pmatrix} a_{11} & a_{12} & a_{13} \\ a_{21} & a_{22} & a_{23} \\ a_{31} & a_{32} & a_{33} \end{pmatrix}\begin{pmatrix} X^s \\ Z^s \\ X^{\mathrm{rel}} \end{pmatrix}, \tag{77}$$

where

$$a_{11} = -\frac{\left(\omega^2 + 4\gamma\right)(\rho - \alpha\rho_f)}{\lambda_c + 2\mu_c} + \frac{\ell(\ell+1)(\phi - \alpha)\rho_f^2\gamma^2}{\omega^2\rho_e(\lambda_c + 2\mu_c)}, \tag{78}$$

$$a_{12} = \frac{\ell(\ell+1)\gamma}{\lambda_c + 2\mu_c}\left[\left(\rho - \frac{\phi\rho_f^2}{\rho_e}\right) - \alpha\rho_f\left(1 - \frac{\rho_f}{\rho_e}\right)\right], \tag{79}$$

$$a_{13} = -\frac{\omega^2(\phi\rho_f - \alpha\rho_e)}{\lambda_c + 2\mu_c} - \frac{\left[(\phi - \alpha)\rho + 3\phi(\rho - \alpha\rho_f)\right]\rho_f\gamma}{\rho(\lambda_c + 2\mu_c)} + \frac{\ell(\ell+1)(\phi - \alpha)\rho_f^2\gamma^2}{\omega^2\rho_e(\lambda_c + 2\mu_c)}, \tag{80}$$

$$a_{21} = \left(\rho - \frac{\phi\rho_f^2}{\rho_e}\right)\frac{\gamma}{\mu_c}, \tag{81}$$

$$a_{22} = -\frac{\omega^2}{\mu_c}\left(\rho - \frac{\phi\rho_f^2}{\rho_e}\right), \tag{82}$$

$$a_{23} = \left(1 - \frac{\rho_f}{\rho_e}\right)\frac{\phi\rho_f\gamma}{\mu_c}, \tag{83}$$

$$a_{31} = -\frac{\left(\omega^2 + 4\gamma\right)\rho_f}{\phi M} + \frac{\ell(\ell+1)\rho_f^2\gamma^2}{\omega^2\phi\rho_e M} - \frac{\alpha}{\phi}a_{11}, \tag{84}$$

$$a_{32} = \left(1 - \frac{\rho_f}{\rho_e}\right)\frac{\ell(\ell+1)\rho_f\gamma}{\phi M} - \frac{\alpha}{\phi}a_{12}, \tag{85}$$

$$a_{33} = -\left[\omega^2\rho_e + \left(1 + \frac{3\phi\rho_f}{\rho}\right)\rho_f\gamma\right]\frac{1}{\phi M} + \frac{\ell(\ell+1)\rho_f^2\gamma^2}{\omega^2\phi\rho_e M} - \frac{\alpha}{\phi}a_{13}. \tag{86}$$

Let $-\left(k_i^e\right)^2$ $(i = 1, 2, 3)$ be the eigenvalues of the matrix A, $\boldsymbol{p}_i$ be the corresponding eigenvector, and $P = \left(\boldsymbol{p}_1, \boldsymbol{p}_2, \boldsymbol{p}_3\right)$. Then, we have

$$P^{-1}AP = \begin{pmatrix} -\left(k_1^e\right)^2 & 0 & 0 \\ 0 & -\left(k_2^e\right)^2 & 0 \\ 0 & 0 & -\left(k_3^e\right)^3 \end{pmatrix}, \tag{87}$$

where P^{-1} is the inverse matrix of P. By multiplying P^{-1} from the left, the left-hand side of Equation 77 becomes

$$P^{-1}\nabla^2\begin{pmatrix} X^s \\ Z^s \\ X^{\mathrm{rel}} \end{pmatrix} = \nabla^2 P^{-1}\begin{pmatrix} X^s \\ Z^s \\ X^{\mathrm{rel}} \end{pmatrix}, \tag{88}$$

because P as well as A are independent of r. On the other hand, by multiplying P^{-1} from the left, the right-hand side of Equation 77 becomes

$$P^{-1}A\begin{pmatrix} X^s \\ Z^s \\ X^{\rm rel} \end{pmatrix} = P^{-1}A\left(PP^{-1}\right)\begin{pmatrix} X^s \\ Z^s \\ X^{\rm rel} \end{pmatrix} = \left(P^{-1}AP\right)P^{-1}\begin{pmatrix} X^s \\ Z^s \\ X^{\rm rel} \end{pmatrix} = \begin{pmatrix} -\left(k_1^e\right)^2 & 0 & 0 \\ 0 & -\left(k_2^e\right)^2 & 0 \\ 0 & 0 & -\left(k_3^e\right)^3 \end{pmatrix}P^{-1}\begin{pmatrix} X^s \\ Z^s \\ X^{\rm rel} \end{pmatrix}. \tag{89}$$

If we denote

$$\boldsymbol{X} = P^{-1}\begin{pmatrix} X^s \\ Z^s \\ X^{\rm rel} \end{pmatrix}, \tag{90}$$

we obtain

$$\nabla^2\boldsymbol{X} = \begin{pmatrix} -\left(k_1^e\right)^2 & 0 & 0 \\ 0 & -\left(k_2^e\right)^2 & 0 \\ 0 & 0 & -\left(k_3^e\right)^3 \end{pmatrix}\boldsymbol{X}. \tag{91}$$

The nontrivial (i.e., nonzero) solution of $\left(\nabla^2 + k^2\right)X(r) = 0$ is given by $X(r) = cj_\ell(kr)$, where c is a constant and j_ℓ is the spherical Bessel function of the first kind of the order of ℓ (e.g., Arfken et al., 2013), respectively. Consequently, the solution is given by

$$\begin{pmatrix} X^s \\ Z^s \\ X^{\rm rel} \end{pmatrix} = P\boldsymbol{X} = P\begin{pmatrix} c_1 j_\ell\left(k_1^e r\right) \\ c_2 j_\ell\left(k_2^e r\right) \\ c_3 j_\ell\left(k_3^e r\right) \end{pmatrix} = \begin{pmatrix} \sum_{i=1}^3 c_i p_{1i} j_\ell\left(k_i^e r\right) \\ \sum_{i=1}^3 c_i p_{2i} j_\ell\left(k_i^e r\right) \\ \sum_{i=1}^3 c_i p_{3i} j_\ell\left(k_i^e r\right) \end{pmatrix}, \tag{92}$$

where c_i $(i = 1, 2, 3)$ are constants to be determined by the boundary condition at the surface, and p_{ji} is the jth component of $\boldsymbol{p}_i$. Using k_i^e and p_{ji}, three of the four linearly independent solutions for the y functions can be expressed as follows:

$$y_1 = \frac{\ell h_i^s}{k_i^e r} j_\ell\left(k_i^e r\right) + \frac{p_{1i}}{k_i^e} j_{\ell+1}\left(k_i^e r\right), \tag{93}$$

$$y_2 = -\alpha y_9 + (\lambda_c + 2\mu_c)p_{1i} j_\ell\left(k_i^e r\right) + \frac{2\ell(\ell-1)h_i^s \mu_c}{k_i^e r^2} j_\ell\left(k_i^e r\right) - \frac{2[2p_{1i} - \ell(\ell+1)p_{2i}]\mu_c}{k_i^e r} j_{\ell+1}\left(k_i^e r\right), \tag{94}$$

$$y_3 = \frac{h_i^s}{k_i^e r} j_\ell\left(k_i^e r\right) + \frac{p_{2i}}{k_i^e} j_{\ell+1}\left(k_i^e r\right), \tag{95}$$

$$y_4 = \mu_c\left[\left(p_{2i} + \frac{2(\ell-1)h_i^s}{k_i^e r^2}\right) j_\ell\left(k_i^e r\right) + \frac{2(p_{1i} - p_{2i})}{k_i^e r} j_{\ell+1}\left(k_i^e r\right)\right], \tag{96}$$

$$y_5 = -\frac{3\gamma}{\left(k_i^e\right)^2}\left(p_{1i} + \frac{\phi\rho_f}{\rho} p_{3i}\right) j_\ell\left(k_i^e r\right), \tag{97}$$

$$y_6 = -\frac{3(\ell+1)\gamma}{\left(k_i^e\right)^2 r}\left[p_{1i} - \ell p_{2i} + \frac{\phi\rho_f}{\rho}(p_{3i} - \ell p_{4i})\right] j_\ell\left(k_i^e r\right), \tag{98}$$

$$y_8 = \frac{\ell h_i^{\mathrm{rel}}}{k_i^e r} j_\ell\left(k_i^e r\right) + \frac{p_{3i}}{k_i^e} j_{\ell+1}\left(k_i^e r\right), \tag{99}$$

$$y_9 = -M(\alpha p_{1i} + \phi p_{3i}) j_\ell\left(k_i^e r\right), \tag{100}$$

$$y_{10} = \frac{h_i^{\mathrm{rel}}}{k_i^e r} j_\ell\left(k_i^e r\right) + \frac{p_{4i}}{k_i^e} j_{\ell+1}\left(k_i^e r\right), \tag{101}$$

where

$$p_{4i} = \frac{\rho_f \gamma}{\omega^2 \rho_e}(p_{1i} + p_{3i}) - \frac{\rho_f}{\rho_e} p_{2i}, \tag{102}$$

$$h_i^s = -\frac{p_{1i} + (\ell+1)p_{2i}}{k_i^e}, \tag{103}$$

$$h_i^{\mathrm{rel}} = -\frac{p_{3i} + (\ell+1)p_{4i}}{k_i^e}. \tag{104}$$

The fourth solution is the trivial solution; $X^s = Z^s = X^{\mathrm{rel}} = 0$. It is found that it is the same as the trivial solution for the nonporous case with no relative fluid motion:

$$y_1 = \ell r^{\ell-1}, \tag{105}$$

$$y_2 = 2\ell(\ell-1)\mu_c r^{\ell-2}, \tag{106}$$

$$y_3 = r^{\ell-1}, \tag{107}$$

$$y_4 = 2(\ell-1)\mu_c r^{\ell-2}, \tag{108}$$

$$y_5 = \left(\ell\gamma - \omega^2\right) r^\ell, \tag{109}$$

$$y_6 = \frac{2\ell+1}{r} y_5 - 3\gamma y_1 = \left[2\ell(\ell-1)\gamma - (2\ell+1)\omega^2\right] r^{\ell-1}, \tag{110}$$

$$y_8 = 0, \tag{111}$$

$$y_9 = 0, \tag{112}$$

$$y_{10} = 0. \tag{113}$$

The no relative fluid motion condition can be derived from the equations of motion for solid and fluid.

As discussed in Appendix E, this method can also be applied to the nonporous case. Thus, the eigenvalue approach proposed here is not specific to the porous case but is a comprehensive method that can be applicable to both porous and nonporous cases.

2.3.2. Incompressible Case

If both the solid and fluid are incompressible, $\alpha \to 1$, and $M \to \infty$. Under these limits, the equation system degenerates; both Equations 73 and 75 become

$$\nabla^2\left(X^s + \phi X^{\mathrm{rel}}\right) = 0. \tag{114}$$

To avoid degeneration, y_9, which is given by

$$y_9 = -M\left(X^s + \phi X^{\mathrm{rel}}\right), \tag{115}$$

is chosen as a variable to be solved instead of X^{rel}. Note that y_9 does not diverge even if $M \to \infty$ (at the same time, $X^s + \phi X^{\mathrm{rel}} \to 0$). Then, we have

$$\nabla^2\begin{pmatrix}X^s\\Z^s\end{pmatrix}=A'\begin{pmatrix}X^s\\Z^s\end{pmatrix}=\begin{pmatrix}a'_{11}&a'_{12}\\a'_{21}&a'_{22}\end{pmatrix}\begin{pmatrix}X^s\\Z^s\end{pmatrix}, \tag{116}$$

where

$$a'_{11}=-\frac{\omega^2}{\lambda_c+2\mu_c}\left(\rho-\frac{\rho_e}{\phi}\right)+\left(-4\rho+\frac{\rho_f}{\phi}+\frac{3\rho_f^2}{\rho}\right)\frac{\gamma}{\lambda_c+2\mu_c}-\frac{\ell(\ell+1)\left(1-\phi^2\right)\rho_f^2\gamma^2}{\omega^2\phi^2\rho_e(\lambda_c+2\mu_c)}, \tag{117}$$

$$a'_{12}=\ell(\ell+1)\left(\rho-\rho_f+(1-\phi)\frac{\rho_f^2}{\rho_e}\right)\frac{\gamma}{\lambda_c+2\mu_c}, \tag{118}$$

$$a'_{21}=\left(\rho-\rho_f+(1-\phi)\frac{\rho_f^2}{\rho_e}\right)\frac{\gamma}{\mu_c}, \tag{119}$$

$$a'_{22}=-\frac{\omega^2}{\mu_c}\left(\rho-\frac{\phi\rho_f^2}{\rho_e}\right), \tag{120}$$

and

$$\nabla^2 y_9=a'_{31}X^s+a'_{32}Z^s, \tag{121}$$

where

$$a'_{31}=-\omega^2\left(\rho_f-\frac{\rho_e}{\phi}\right)-4\rho_f\gamma+\left(1+\frac{3\phi\rho_f}{\rho}\right)\frac{\rho_f\gamma}{\phi}-\frac{\ell(\ell+1)(1-\phi)\rho_f^2\gamma^2}{\omega^2\phi\rho_e}, \tag{122}$$

$$a'_{32}=-\ell(\ell+1)\left(1-\frac{\rho_f}{\rho_e}\right)\rho_f\gamma. \tag{123}$$

The following procedure to obtain the solution is similar to the compressible case. Specifically, X^s and Z^s are given by

$$\begin{pmatrix}X^s\\Z^s\end{pmatrix}=\begin{pmatrix}\sum_{i=1}^{2}c'_i p'_{1i}j_\ell\left(k_i^{e\prime}r\right)\\\sum_{i=1}^{2}c'_i p'_{2i}j_\ell\left(k_i^{e\prime}r\right)\end{pmatrix}, \tag{124}$$

where c'_i $(i=1,2)$ is a constant to be determined by the boundary condition at the surface, $-\left(k_i^{e\prime}\right)^2$ is the eigenvalues of the matrix A', and p'_{ij} is the jth component of the corresponding eigenvector. Then, two sets of solutions are given by Equations 93–101 except for replacing k_i^e with $k_i^{e\prime}$, p_{1i} with p'_{1i}, p_{2i} with p'_{2i}, p_{3i} with $p'_{3i}=-p'_{1i}/\phi$, and

$$y_9=-\frac{a'_{31}p'_{1i}+a'_{32}p'_{2i}}{\left(k_i^{e\prime}\right)^2}j_\ell\left(k_i^{e\prime}r\right), \tag{125}$$

respectively. It is noted that since A' is a 2×2 matrix, the eigenvalues $-\left(k_i^{e\prime}\right)^2$ of A' can be easily expressed as

$$-\left(k_i^{e\prime}\right)^2=\frac{1}{2}\left(a'_{11}+a'_{22}\pm\sqrt{\left(a'_{22}-a'_{11}\right)^2+4a'_{12}a'_{21}}\right). \tag{126}$$

The other two sets of solutions are given by $X^s=Z^s=0$. One such solution (i.e., the third solution) is given by

$$y_1=\ell r^{\ell-1}, \tag{127}$$

$$y_2=-y_9+2\ell(\ell-1)\mu_c r^{\ell-2}, \tag{128}$$

$$y_3=r^{\ell-1}, \tag{129}$$

$$y_4 = 2(\ell - 1)\mu_c r^{\ell-2}, \tag{130}$$

$$y_5 = 0, \tag{131}$$

$$y_6 = -3\ell\gamma\left(1 + \frac{\phi\rho_f}{\rho}b_1\right)r^{\ell-1}, \tag{132}$$

$$y_8 = b_1\ell r^{\ell-1}, \tag{133}$$

$$y_9 = b_2 r^{\ell}, \tag{134}$$

$$y_{10} = b_1 r^{\ell-1}, \tag{135}$$

where

$$b_1 = \frac{\left(\ell\gamma - \omega^2\right)(\rho - \rho_f)}{\omega^2(\phi\rho_f - \rho_e) + (1-\phi)\ell\rho_f\gamma}, \tag{136}$$

$$b_2 = \left(\omega^2 - \ell\gamma\right)(\rho + b_1\phi\rho_f). \tag{137}$$

The fourth solution is the trivial solution for a compressible case given by Equations 105–113.

Similar to the compressible case, the eigenvalue approach can be applicable to the nonporous incompressible case. In this case, only one solution can be written using spherical Bessel functions, and the other two solutions can be written using a power of r. See Appendix E for details.

2.4. Boundary Conditions

This theory can be applied to various kinds of problems by choosing appropriate boundary conditions. The boundary conditions for y_1–y_6 are the same for the nonporous case and are already given in previous studies (e.g., Saito, 1974). The boundary conditions for the newly defined y_8 and y_9 depend on whether the boundary is permeable or not. Below, the boundary conditions not only at the surface but also at a layer boundary inside the body that are relevant for planetary applications are summarized. Note that y_1 and y_2 describe radial displacement and stress, y_3 and y_4 describe shear displacement and stress, y_5 and y_6 describe gravitational potential and radial acceleration (Takeuchi & Saito, 1972), y_8 describes radial displacement of fluid relative to solid, and y_9 describes pore pressure.

2.4.1. Free Surface Under Tidal Potential

This is the condition when tidal Love numbers are calculated. In this case, the pore pressure as well as radial and shear stresses needs to be zero. Thus, the boundary conditions are given by

$$y_2 = 0, \quad y_4 = 0, \quad y_6 = \frac{2\ell + 1}{R}, \quad y_9 = 0, \tag{138}$$

where R is the surface radius of the body.

2.4.2. Loaded Surface

This is the condition when load Love numbers are calculated. A difference from the free surface is that radial stress is not zero. For a permeable load,

$$y_2 = -\frac{(2\ell + 1)g(R)}{4\pi GR}, \quad y_4 = 0, \quad y_6 = \frac{2\ell + 1}{R}, \quad y_9 = -y_2, \tag{139}$$

while for an impermeable load,

$$y_2 = -\frac{(2\ell + 1)g(R)}{4\pi GR}, \quad y_4 = 0, \quad y_6 = \frac{2\ell + 1}{R}, \quad y_8 = 0, \tag{140}$$

where $g(R)$ is the gravitational acceleration at the surface (e.g., Saito, 1974).

2.4.3. Pressed Surface

This is the condition when press (or pressure) Love numbers are calculated. This is similar to the case of the loaded surface, but the surface is free from the potential. Thus,

$$y_2 = -\frac{(2\ell+1)g(R)}{4\pi GR}, \quad y_4 = 0, \quad y_6 = 0, \quad y_9 = -y_2 \text{ or } y_8 = 0. \tag{141}$$

The last condition for the pore fluid depends on the permeability of the surface.

2.4.4. Shear-Stressed Surface

This is the condition when shear Love numbers are calculated. In this case, a potential-free shear stress is applied, and shear stress does not introduce pore pressure. Thus, the boundary conditions for this case are (e.g., Saito, 1978):

$$y_2 = 0, \quad y_4 = \frac{(2\ell+1)g(R)}{4\pi\ell(\ell+1)GR}, \quad y_6 = 0, \quad y_9 = 0. \tag{142}$$

2.4.5. Perfect Contact With a Permeable Solid Layer

If two porous layers contact each other, solid displacements, stresses and pore pressure, and gravitational potential and acceleration are continuous. However, the relative displacement of fluid in the vertical direction is not necessarily continuous because the volume of the fluid expelled from a layer must be the same as that entered to the other layer. Then we have

$$y_i^{\text{up}} = y_i^{\text{low}} \quad (i = 1, 2, 3, 4, 5, 6, 9), \tag{143}$$

$$\phi^{\text{up}} y_8^{\text{up}} = \phi^{\text{low}} y_8^{\text{low}}, \tag{144}$$

where superscripts "up" and "low" indicate the upper and lower porous layers, respectively.

2.4.6. Perfect Contact With an Impermeable Solid Layer

In this case, solid displacements, stresses, and gravitational potential and acceleration are continuous. In addition, and the relative displacement of fluid in the vertical direction should be zero. Thus, there are seven conditions as follows:

$$y_i^p = y_i^s \quad (i = 1, 2, 3, 4, 5, 6), \tag{145}$$

$$y_8^p = 0, \tag{146}$$

where superscripts p and s indicate the porous and nonporous solid layers, respectively.

2.4.7. Shear-Free Contact With a Liquid Layer

In this case, radial and shear stresses and gravitational potential and accelaraton are continuous. On the other hand, displacements are not continuous. Specifically, the effective radial displacement ($y_1 + \phi y_8$) of the porous layer should be continuous with the radial displacement (y_1) of the liquid layer. In addition, the pore pressure (y_9) equals the liquid pressure ($-y_2$). Thus, there are six conditions as follows:

$$y_1^p + \phi y_8^p = y_1^l, \tag{147}$$

$$y_i^p = y_i^l \quad (i = 2, 5, 6), \tag{148}$$

$$y_4^p = 0, \tag{149}$$

$$y_9^p = -y_2^l, \tag{150}$$

where superscripts p and l indicate the porous and liquid layers, respectively.

If a liquid layer is modeled as dynamic (i.e., $\omega \neq 0$), y_1, y_2, and y_6 in the liquid layer can be determined separately (Kamata et al., 2015). However, if a liquid layer is modeled as static (i.e., $\omega = 0$), not all y functions can be

determined separately (e.g., Saito, 1974); Only two variables, y_5 and $y_7 = y_6 + 4\pi G y_2/g$, can be calculated, and $y_2 = \rho g y_1 - \rho y_5$ is satisfied in the liquid layer. For such a case, there are five conditions as follows:

$$y_2^p = y_2^l = \rho^l g\left(y_1^p + \phi y_8^p\right) - \rho^l y_5^l, \tag{151}$$

$$y_4^p = 0, \tag{152}$$

$$y_5^p = y_5^l, \tag{153}$$

$$y_6^p + \frac{4\pi G}{g} y_2^p = y_7^l, \tag{154}$$

$$y_9^p = -y_2^l. \tag{155}$$

It is noted that Equation A18b of Rovira-Navarro et al. (2022), which corresponds to Equation 151 of this work, ignores the contribution of the radial displacement of the fluid relative to the solid.

2.5. Heating Rate (Energy Dissipation Rate)

In this subsection, we derive some useful expressions for the heating rate per unit volume. More specifically, we derive the local heating rate (as a function of radius, latitude, and longitude), a horizontally averaged heating rate (which is a function of only radius), and a horizontally and radially integrated heating rate using y functions.

The work $\delta\mathcal{W}$ per unit volume of a fluid-saturated porous material is given by (e.g., Biot, 1956a; Cheng, 2016)

$$\delta\mathcal{W} = \sigma_{ij}\delta e_{ij}^s - p_f \frac{\partial}{\partial x_i}\left(\phi\delta u_i^{\mathrm{rel}}\right) = \sigma_{ij}\delta e_{ij}^s - p_f\left(\phi\delta e_{kk}^{\mathrm{rel}} + \frac{d\phi}{dr}\delta u_r^{\mathrm{rel}}\right). \tag{156}$$

On the other hand, the dissipation δD due to a small fluid motion relative to the solid is given by (e.g., Biot, 1956a; Cheng, 2016)

$$\delta D = \frac{\phi^2\eta_f\,\mathrm{Re}(F_f)}{k}\frac{\partial u_i^{\mathrm{rel}}}{\partial t}\delta u_i^{\mathrm{rel}}, \tag{157}$$

where $\mathrm{Re}(x)$ indicates the real part of x. The imaginary part of F_f introduces an apparent force called the Basset force (e.g., Cheng, 2016), which is in phase with the forcing and thus does not contribute to the energy dissipation.

Then, the rate $\mathcal{P}$ of energy dissipation (i.e., heating rate) per unit volume at a given location (r, θ, φ) averaged over a forcing period T is given by (e.g., Beuthe, 2013; Biot, 1956a; Cheng, 2016; Liao et al., 2020)

$$\begin{aligned}\mathcal{P}(r,\theta,\varphi) &= \frac{1}{T}\int_0^T \frac{\partial\mathcal{W}}{\partial t}dt + \frac{1}{T}\int_0^T \frac{\partial D}{\partial t}dt \\ &= \frac{\omega}{2}\,\mathrm{Im}\left(\widetilde{\sigma}_{ij}\widetilde{e}_{ij}^{s*} - \phi\widetilde{p}_f\widetilde{e}_{kk}^{\mathrm{rel}*} - \frac{d\phi}{dr}\widetilde{p}_f\widetilde{u}_r^{\mathrm{rel}*}\right) + \frac{\omega^2\phi^2\eta_f\,\mathrm{Re}(F_f)}{2k}\left|\widetilde{u}_i^{\mathrm{rel}}\right|^2,\end{aligned} \tag{158}$$

where $\mathrm{Im}(x)$ indicates the imaginary part of x, and the superscript * indicates the complex conjugate, respectively. Equations 5 and 6 yield

$$\widetilde{\sigma}_{ij}\widetilde{e}_{ij}^{s*} = \lambda_c\left|\widetilde{e}_{kk}^s\right|^2 + 2\mu_c\left(\left|\widetilde{e}_{rr}^s\right|^2 + \left|\widetilde{e}_{\theta\theta}^s\right|^2 + \left|\widetilde{e}_{\varphi\varphi}^s\right|^2 + 2\left|\widetilde{e}_{r\theta}^s\right|^2 + 2\left|\widetilde{e}_{r\varphi}^s\right|^2 + 2\left|\widetilde{e}_{\theta\varphi}^s\right|^2\right) + \alpha M\left(\alpha\left|\widetilde{e}_{kk}^s\right|^2 + \phi\widetilde{e}_{kk}^{\mathrm{rel}}\widetilde{e}_{kk}^{s*}\right), \tag{159}$$

$$\widetilde{p}_f\widetilde{e}_{kk}^{\mathrm{rel}*} = -M\left(\alpha\widetilde{e}_{kk}^s\widetilde{e}_{kk}^{\mathrm{rel}*} + \phi\left|\widetilde{e}_{kk}^{\mathrm{rel}}\right|^2\right). \tag{160}$$

Then, $\mathcal{P}$ can be written as the sum of four components

$$\mathcal{P}(r,\theta,\varphi) = \mathcal{P}_K + \mathcal{P}_\mu + \mathcal{P}_M + \mathcal{P}_\eta, \tag{161}$$

where

$$\mathcal{P}_K = \frac{\omega\,\mathrm{Im}(K_d)}{2}\left|\widetilde{e}_{kk}^s\right|^2 \tag{162}$$

is the heating due to dilatation of the solid,

$$\mathcal{P}_\mu = \omega\,\mathrm{Im}(\mu_c)\left(\left|\widetilde{e}^s_{rr}\right|^2 + \left|\widetilde{e}^s_{\theta\theta}\right|^2 + \left|\widetilde{e}^s_{\varphi\varphi}\right|^2 + 2\left|\widetilde{e}^s_{r\theta}\right|^2 + 2\left|\widetilde{e}^s_{r\varphi}\right|^2 + 2\left|\widetilde{e}^s_{\theta\varphi}\right|^2 - \frac{1}{3}\left|\widetilde{e}^s_{kk}\right|^2\right) \tag{163}$$

is that due to the change of solid shape,

$$\mathcal{P}_M = \frac{\omega\,\mathrm{Im}(M)}{2}\left|\alpha\widetilde{e}^s_{kk} + \phi\widetilde{e}^{\mathrm{rel}}_{kk}\right|^2 = \frac{\omega\,\mathrm{Im}(M)}{2}\left|\frac{\widetilde{p}_f}{M}\right|^2 \tag{164}$$

is that due to dilatation of fluid (relative to solid), and

$$\mathcal{P}_\eta = \frac{\omega^2\phi^2\eta_f\,\mathrm{Re}(F_f)}{2k}\left(\left|\widetilde{u}^{\mathrm{rel}}_r\right|^2 + \left|\widetilde{u}^{\mathrm{rel}}_\theta\right|^2 + \left|\widetilde{u}^{\mathrm{rel}}_\varphi\right|^2\right) - \frac{\omega}{2}\frac{d\phi}{dr}\,\mathrm{Im}\left(\widetilde{p}_f\widetilde{u}^{\mathrm{rel}*}_r\right) \tag{165}$$

is due to the fluid flow relative to the solid, respectively. The forms of $\mathcal{P}_K$ and $\mathcal{P}_\mu$ derived above are the same as those found for a nonporous solid material (e.g., Beuthe, 2013). Consequently, the total heating rate is simply the sum of the heating in the solid and that due to relative fluid deformation. It is noted that $\mathrm{Im}(K_d)$ and $\mathrm{Im}(M)$ (consequently, $\mathcal{P}_K$ and $\mathcal{P}_M$) are zero if bulk dissipation is not considered (see Section 2.1.1). The relationship between y functions and strains and displacements can be found in Appendix F.

Next, let us consider the horizontally averaged heating rate. For each $\mathcal{P}_\xi$ ($\xi = K, \mu, M, \eta$), we find

$$h_K(r) = \frac{1}{4\pi}\int_{\varphi=0}^{2\pi}\int_{\theta=0}^{\pi}\mathcal{P}_K\sin\theta\,d\theta\,d\varphi = \sum_\ell \frac{\omega U_\ell^2}{2r^2}\mathrm{Im}(K_d)H_K^\ell, \tag{166}$$

$$h_\mu(r) = \frac{1}{4\pi}\int_{\varphi=0}^{2\pi}\int_{\theta=0}^{\pi}\mathcal{P}_\mu\sin\theta\,d\theta\,d\varphi = \sum_\ell \frac{\omega U_\ell^2}{2r^2}\mathrm{Im}(\mu_c)H_\mu^\ell, \tag{167}$$

$$h_M(r) = \frac{1}{4\pi}\int_{\varphi=0}^{2\pi}\int_{\theta=0}^{\pi}\mathcal{P}_M\sin\theta\,d\theta\,d\varphi = \sum_\ell \frac{\omega U_\ell^2}{2r^2}\mathrm{Im}(M)H_M^\ell, \tag{168}$$

$$h_\eta(r) = \frac{1}{4\pi}\int_{\varphi=0}^{2\pi}\int_{\theta=0}^{\pi}\mathcal{P}_\eta\sin\theta\,d\theta\,d\varphi = \sum_\ell \frac{\omega U_\ell^2}{2r^2}\omega\eta_f\mathrm{Re}(F_f)H_\eta^\ell, \tag{169}$$

where

$$U_\ell^2 = \sum_m N_\ell^m|U_{\ell m}|^2, \tag{170}$$

$$H_K^\ell = \left|r\frac{dy_1}{dr} + 2y_1 - \ell(\ell+1)y_3\right|^2 = \left|\frac{4\mu_c y_1 + ry_2 - 2\ell(\ell+1)\mu_c y_3 + \alpha r y_9}{\lambda_c + 2\mu_c}\right|^2, \tag{171}$$

$$\begin{aligned} H_\mu^\ell &= \frac{1}{3}\left|2r\frac{dy_1}{dr} - 2y_1 + \ell(\ell+1)y_3\right|^2 + \ell(\ell+1)\left|\frac{r}{\mu_c}y_4\right|^2 + (\ell-1)\ell(\ell+1)(\ell+2)|y_3|^2 \\ &= \frac{1}{3}\left|\frac{-6K_d y_1 + 2ry_2 + 3\ell(\ell+1)K_d y_3 + 2\alpha r y_9}{\lambda_c + 2\mu_c}\right|^2 + \ell(\ell+1)\left|\frac{r}{\mu_c}y_4\right|^2 + (\ell-1)\ell(\ell+1)(\ell+2)|y_3|^2, \end{aligned} \tag{172}$$

$$H_M^\ell = \left|\frac{r}{M}y_9\right|^2, \tag{173}$$

$$H_\eta^\ell = \frac{\phi^2 r^2}{k}\left(|y_8|^2 + \ell(\ell+1)|y_{10}|^2\right) - \frac{r^2}{\omega\eta_f\mathrm{Re}(F_f)}\frac{d\phi}{dr}\,\mathrm{Im}\left(y_8^* y_9\right), \tag{174}$$

and N_ℓ^m is the normalization factor given by

$$\begin{aligned} N_\ell^m &= \frac{1}{2}\int_0^\pi P_\ell^m(\cos\theta)P_\ell^m(\cos\theta)\sin\theta\,d\theta = \frac{1}{4\pi}\int_{\varphi=0}^{2\pi}\int_{\theta=0}^{\pi}\left|Y_\ell^m(\theta,\varphi)\right|^2\sin\theta\,d\theta\,d\varphi \\ &= \frac{1}{2\ell+1}\frac{(\ell+m)!}{(\ell-m)!}. \end{aligned} \tag{175}$$

Consequently, the horizontally averaged volumetric heating rate h as a function of radial position r is given by

$$\begin{aligned} h(r) &= \frac{1}{4\pi}\int_{\varphi=0}^{2\pi}\int_{\theta=0}^{\pi}\mathcal{P}(r,\theta,\varphi)\sin\theta\, d\theta\, d\varphi = h_K + h_\mu + h_M + h_\eta \\ &= \sum_\ell \frac{\omega U_\ell^2}{2r^2}\left[\mathrm{Im}(K_d)H_K^\ell + \mathrm{Im}(\mu_c)H_\mu^\ell + \mathrm{Im}(M)H_M^\ell + \omega\eta_f \mathrm{Re}(F_f)H_\eta^\ell\right]. \end{aligned} \tag{176}$$

Here, H_K^ℓ and H_μ^ℓ under the limit of $\alpha \to 0$ are equivalent to H_K and H_μ, respectively, defined by previous studies (Beuthe, 2013; Tobie et al., 2005). In addition, H_η^ℓ under the limit of $d\phi/dr \to 0$ leads to the result equivalent to Equation D12b of Rovira-Navarro et al. (2022). Consequently, above formulation is a generalized expression that can reproduce previous expressions assuming limiting conditions.

Finally, we consider the total heating rate in a poroviscoelastic layer. The horizontally and radially integrated volumetric heating rate Q between $r = r_l$ and $r = r_u$ is given by

$$\begin{aligned} Q(r_u, r_l) &= \int_{\varphi=0}^{2\pi}\int_{\theta=0}^{\pi}\int_{r=r_l}^{r_u}\mathcal{P}(r,\theta,\varphi)r^2\sin\theta\, dr\, d\theta\, d\varphi \\ &= 4\pi\int_{r_l}^{r_u} h(r)\, r^2\, dr \\ &= \sum_\ell 2\pi\omega U_\ell^2\left[r^2\,\mathrm{Im}\left(y_1^* y_2 + \ell(\ell+1)y_3^* y_4 + \frac{1}{4\pi G}y_5^* y_6 - \phi y_8^* y_9\right)\right]_{r_l}^{r_u}, \end{aligned} \tag{177}$$

where $[\, y(r)\,]_{r_b}^{r_u} = y(r_u) - y(r_b)$, and r_u and r_l are the upper and lower bound radii, respectively. See Appendix B3 for the derivation.

It is instructive to derive a well-known formula under a special case: the global tidal heating rate for eccentricity tides considering only degree-2 tidal potentials. In this case,

$$U_{\ell=2}^2 = \frac{21}{5}\omega^4 R^4 e^2, \tag{178}$$

where R is the radius of the body and e is the eccentricity. See Appendix G for further details. Using the values of y at the surface given in Section 2.4.1, the global tidal heating rate $Q_{\mathrm{global}}^{\mathrm{ecc}}$ for eccentricity tides is found to be

$$Q_{\mathrm{global}}^{\mathrm{ecc}} = Q(R,0) = -\frac{21\omega^5 R^5 e^2}{2G}\mathrm{Im}(k_2), \tag{179}$$

which is a well-known equation (e.g., Segatz et al., 1988). Thus, this well-known equation is valid even if the body contains a porous layer.

3. Numerical Calculation

3.1. Numerical Procedure

The ordinary differential equation system given by Equations 57–64 is integrated from the center to the surface. Since there are terms with r^{-1} and r^{-2}, the integration needs to be carried out from a small but non-zero radius r_0 using the homogeneous sphere solution given in Section 2.3. Note that the values of $j_\ell\left(k_i^e r_0\right)$ and $j_{\ell+1}\left(k_i^e r_0\right)$ are not required independently; only the ratio $k_i^e r_0 j_{\ell+1}\left(k_i^e r_0\right)/j_\ell\left(k_i^e r_0\right)$ is required (Takeuchi & Saito, 1972).

In the case where the body is an entirely porous sphere, the number of linearly independent solutions are four:

$$y_i(r) = \sum_{j=1}^{4} C_j y_{ij}(r), \tag{180}$$

where the subscript j is the index specifying the linearly independent solution, and C_j ($j = 1, 2, 3, 4$) is the coefficient determined by the surface boundary condition given in Section 2.4. For example, when tidal Love numbers are calculated, C_j is given by

$$\begin{pmatrix} y_{21}(R) & y_{22}(R) & y_{23}(R) & y_{24}(R) \\ y_{41}(R) & y_{42}(R) & y_{43}(R) & y_{44}(R) \\ y_{61}(R) & y_{62}(R) & y_{63}(R) & y_{64}(R) \\ y_{91}(R) & y_{92}(R) & y_{93}(R) & y_{94}(R) \end{pmatrix} \begin{pmatrix} C_1 \\ C_2 \\ C_3 \\ C_4 \end{pmatrix} = \begin{pmatrix} 0 \\ 0 \\ (2\ell+1)/R \\ 0 \end{pmatrix}, \tag{181}$$

where R is the surface radius.

In the case where the body consists of porous and nonporous layers, the number of linearly independent solutions changes. First, let us consider a two-layer body consisting of an inner nonporous solid layer and an outer porous layer. In this case, the number of linearly independent solutions increases from three to four. The first step is to calculate three sets of y_1–y_6 in the inner layer from a small radius r_0 to the internal boundary radius r_b using a six-component equation system (see Appendix C2). The next step is to calculate four sets of y_1–y_9 in the outer layer from r_b to the surface R using an eight-component equation system given by Equations 57–64. The three sets of y_1–y_6 are simply continuous from the inner layer with $y_8 = y_9 = 0$, and one additional set is the one that determines y_9 at r_b. Consequently, the initial values y^p_{ij} for the outer layer are given by

$$y^p_{ij}(r_b) = y^s_{ij}(r_b) \quad (i = 1, \ldots, 6;\ j = 1, 2, 3), \tag{182}$$

$$y^p_{ij}(r_b) = 0 \qquad (i = 8, 9;\ j = 1, 2, 3), \tag{183}$$

$$y^p_{i4}(r_b) = 0 \qquad (i = 1, \ldots, 6, 8), \tag{184}$$

$$y^p_{94}(r_b) = 1, \tag{185}$$

where $y^s_{ij}(r_b)$ is the y values at the upper bound of the inner layer obtained by the first step. It is clear that these initial values satisfy the boundary condition given in Section 2.4.6. The coefficient of four solutions can be determined by the surface boundary conditions (i.e., Equation 181).

Next, let us consider an inverted case; a two-layer body consisting of an inner porous layer and an outer nonporous solid layer. In this case, the number of linearly independent solutions decreases from four to three. Thus, three conditions for the coefficients such as C_1/C_4, C_2/C_4, C_3/C_4 are necessary to determine the initial values. However, at the internal boundary r_b, there is only one condition except for the continuity in y_1–y_6:

$$y^p_8(r_b) = \sum_{j=1}^{4} C^p_j y^p_{8j}(r_b) = 0. \tag{186}$$

Thus, it is not possible to determine the initial values for the outer layer. In practice, this problem can be avoided by considering four solutions even in the nonporous layer with the initial values y^s_{ij} given by

$$y^s_{ij}(r_b) = y^p_{ij}(r_b) \quad (i = 1, \ldots, 6;\ j = 1, \ldots, 4). \tag{187}$$

After the integration in the outer layer, the coefficients of the solutions can be determined from the boundary conditions at the surface and the internal boundary:

$$\begin{pmatrix} y^s_{21}(R) & y^s_{22}(R) & y^s_{23}(R) & y^s_{24}(R) \\ y^s_{41}(R) & y^s_{42}(R) & y^s_{43}(R) & y^s_{44}(R) \\ y^s_{61}(R) & y^s_{62}(R) & y^s_{63}(R) & y^s_{64}(R) \\ y^p_{81}(r_b) & y^p_{82}(r_b) & y^p_{83}(r_b) & y^p_{84}(r_b) \end{pmatrix} \begin{pmatrix} C_1 \\ C_2 \\ C_3 \\ C_4 \end{pmatrix} = \begin{pmatrix} 0 \\ 0 \\ (2\ell+1)/R \\ 0 \end{pmatrix}. \tag{188}$$

For more complex layered structures, it may be simpler to calculate n solutions for a layer where a n-component equation system is applied (i.e., eight solutions for a porous layer and six solutions for a nonporous solid layer). In this case, a simple set of the initial values can be used. For example, in the case of a porous layer,

$$y_{ij}^{p}(r_b) = \delta_{ij} \quad (i = 1, \ldots, 6, 8, 9, j = 1, \ldots, 6), \tag{189}$$

$$y_{i7}^{p}(r_b) = \delta_{i8} \quad (i = 1, \ldots, 6, 8, 9), \tag{190}$$

$$y_{i8}^{p}(r_b) = \delta_{i9} \quad (i = 1, \ldots, 6, 8, 9). \tag{191}$$

Then, the integration can be carried out separately in each layer. The coefficients for the linearly independent solutions in each layer can be calculated from boundary conditions given in Section 2.4 and boundary values.

3.2. Homogeneous Model

Here, we investigate the dependence of deformation of a macroscopically and microscopically homogeneous porous sphere on permeability and frequency. These two parameters can vary by several orders of magnitude, depending on the subject to be investigated. Table 1 lists the parameter values adopted. Other parameters can be calculated from parameters listed in Table 1. For example, the drained bulk modulus K_d can be calculated from K_s and α using Equation 10. The results shown below assume $\left|k_1^e\right| \geq \left|k_2^e\right| \geq \left|k_3^e\right|$, and the eigenvectors are normalized (i.e., $\sqrt{p_{1i}^2 + p_{2i}^2 + p_{3i}^2} = 1$).

As discussed in Section 2.3, y functions for the homogeneous sphere are given by a linear combination of four linearly independent solutions. An example of such solutions is shown in Figure 1. Here, the real parts of y_1 (i.e., the radial displacement of the solid normalized by the loading potential) and y_8 (i.e., the radial displacement of the fluid relative to the solid normalized by the loading potential) are shown. This figure shows that the first nontrivial solution (labeled k_1^e) has the largest absolute value near the surface. Figure 2 shows the dependence of this first nontrivial solution on permeability, demonstrating that a decrease in permeability leads to a large increase in the absolute value of y_8. The physical meaning of this trend is simple: a decrease in permeability leads to a thinning of the region where the pore fluid flows, as can be easily understood from Figure 2b. In this particular case, the flow of the pore fluid occurs in the entire body if permeability is $\geq 10^{-9}$ m^2 but only within a thin surficial layer if permeability is $\leq 10^{-13}$ m^2.

Table 1
Model Parameters for the Homogeneous Model

Quantity	Symbol	Value	Unit
Radius	R	230	km
Biot effective stress coefficient	α	0.5	–
Porosity	ϕ	0.1	–
Permeability	k	10^{-14}–10^{-6}	m^2
Density of solid	ρ_s	3,000	kg m^{-3}
Density of fluid	ρ_f	1,000	kg m^{-3}
Bulk modulus of solid	K_s	40	GPa
Bulk modulus of pore fluid	K_f	2	GPa
Shear modulus of porous medium	μ	10	GPa
Viscosity of solid	η_s	10^{20}	Pa s
Viscosity of pore fluid	η_f	10^{-3}	Pa s
Harmonic degree	ℓ	2	–
Angular frequency	ω	10^{-10}–10^{2}	rad s^{-1}
Porous-medium added-mass coefficient	C_a	Equation A1	–
Fluid viscosity correction factor[a]	F_f	Equation A2, with $\delta_p = 4$	–

[a]δ_p is the pore geometry factor.

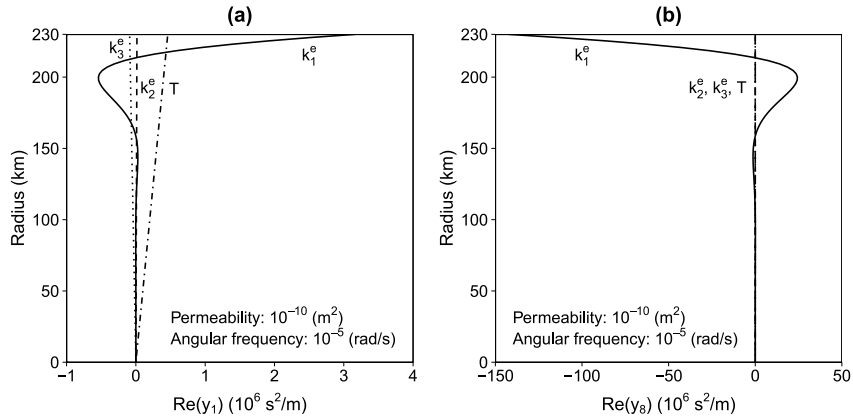

Figure 1. Radial profiles of the real part of the linearly independent solutions of (a) y_1 and (b) y_8. The results for the permeability of 10^{-10} m^2 and the angular frequency of 10^{-5} rad/s are shown. The solid line labeled k_1^e, the dashed line labeled k_2^e, and the dotted line labeled k_3^e represent the first, second, and third nontrivial solutions, respectively. The dot-dashed line labeled T represents the trivial solution.

This thinning of the layer where the pore fluid flows causes a problem when carrying out numerical radial integrations of y functions; unless the layer is very thin, the absolute value of y functions increases rapidly and can exceed the upper limit for the numerical computation (i.e., $\sim 10^{308}$ in the case of a double-precision floating-point format). For example, for the angular frequency of 10^{-5} rad/s, the use of a permeability lower than $\sim 4 \times 10^{-14}$ m^2 results in this problem (see Figure 2a). This value of permeability is not unrealistically low but is a typical terrestrial crustal value at a depth of a few km (Gleeson & Ingebritsen, 2017). Thus, unfortunately, it is difficult to carry out numerical calculations assuming a thick porous layer possessing a permeability typical of terrestrial crust.

However, this numerical problem can be avoided if one adopts an appropriate interior structure model. Because the flow of the pore fluid is limited to a shallow zone, it is reasonable to assume that the inner region is perfectly undrained. The behavior of such a region is equivalent to that of an impermeable pure solid with reduced elastic moduli. Thus, a low-permeability layer can be modeled as a combination of a thin porous layer and a thick nonporous solid layer (Figure 3). Here, the density and the shear modulus of the undrained layer are given by the local mean density and the effective shear modulus, respectively, of the porous case. The bulk modulus of this layer is the undrained bulk modulus K_u given by Cheng (2016).

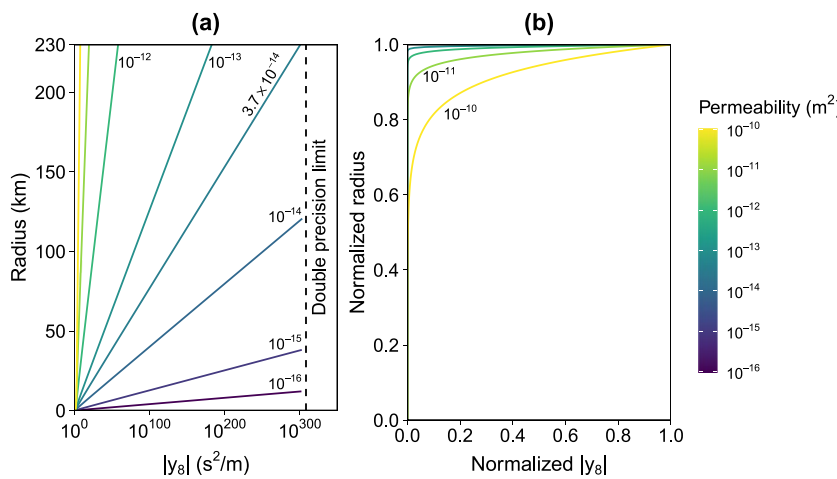

Figure 2. Dependence of the first nontrivial solution for y_8 on permeability. Results for the angular frequency of 10^{-5} rad/s are shown. The left Panel (a) shows the unnormalized (dimensionalized) results, while the right Panel (b) shows the same but normalized results.

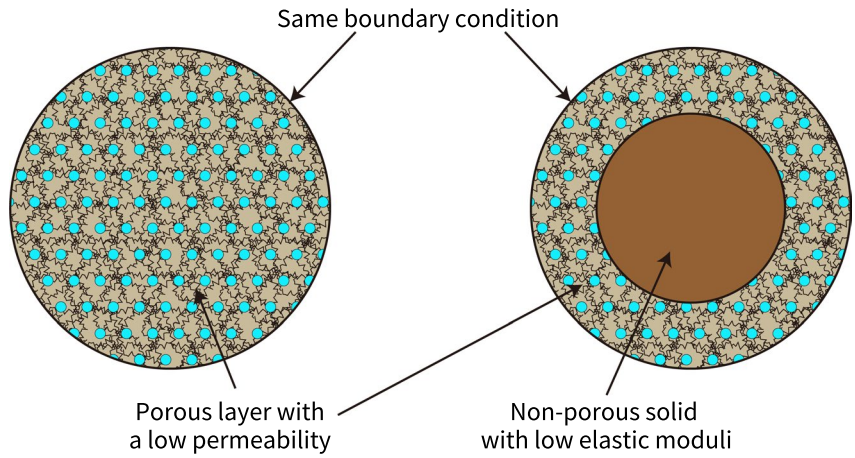

Figure 3. Two numerically equivalent interior structure models. Numerical calculations using the left model may be impossible. In that case, the use of the right model makes numerical calculations possible.

$$K_u = K_d + \alpha^2 M = \left[1 - \alpha + \alpha^2\left(\alpha - \frac{\phi K_s'}{K_s''} + \frac{\phi K_s'}{K_f}\right)^{-1}\right] K_s' = \left[1 - \alpha + \alpha^2\left(\alpha - \phi + \frac{\phi K_s}{K_f}\right)^{-1}\right] K_s. \tag{192}$$

In the case of the parameter values listed in Table 1, $K_u \approx 24.167$ GPa.

The important question that should be addressed here would be where to place the boundary between the drained and undrained layers. Let us first consider a specific calculation condition; as an example, the permeability of 10^{-14} m^2 and the angular frequency of 10^{-5} rad/s are chosen here. Figure 4a shows a shallow part of the radial profile of the amplitude of y_8. Here, the four linearly independent solutions are combined using the boundary conditions given in Section 2.4.1. In this case, a porous layer thicker than ∼5 km leads to numerical instability, while a layer thinner than ∼1 km leads to inaccurate results. Thus, a porous layer thickness of approximately 3 ± 2 km is appropriate. The same conclusion can be obtained from the y values at the surface, as demonstrated in Figure 4b.

Let us now investigate the solution from a mathematical point of view to obtain a guideline value for this porous layer thickness under various calculation conditions. As discussed in Section 2.3, the nontrivial solutions can be

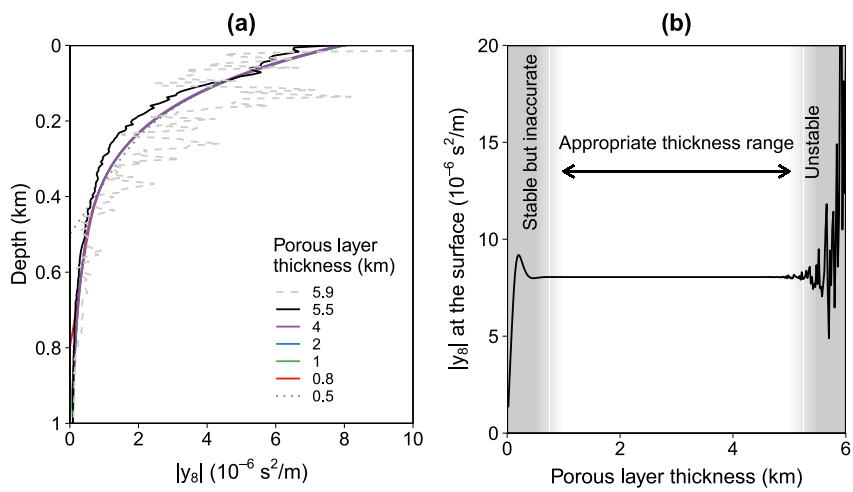

Figure 4. Dependence of the numerical stability and accuracy of the solution on the porous layer thickness. Results for a permeability of 10^{-14} m^2 and an angular frequency of 10^{-5} rad/s are shown. The left Panel (a) shows radial profiles of y_8 for different porous layer thicknesses, while the right Panel (b) shows the value of y_8 at the surface as a function of the porous layer thickness.

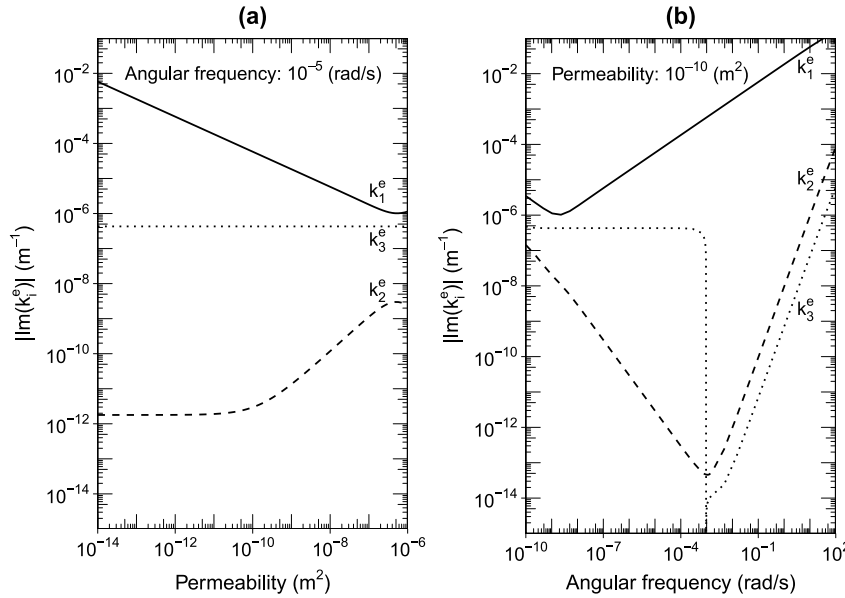

Figure 5. Dependence of the eigenvalue $\left(-\left(k_i^e\right)^2\right)$ on the (a) permeability and (b) angular frequency. Results for (a) an angular frequency of 10^{-5} rad/s and (b) a permeability of 10^{-10} m^2, respectively, are shown. $\left|k_1^e\right| \geq \left|k_2^e\right| \geq \left|k_3^e\right|$ is assumed.

written using spherical Bessel functions (i.e., j_ℓ and $j_{\ell+1}$). In general, the spherical Bessel function for a complex argument can be approximated as

$$j_\ell\left(k_i^e r\right) \approx \frac{e^{\left|\mathrm{Im}\left(k_i^e r\right)\right|}}{2k_i^e r} i^{\pm(\ell+1)} e^{\mp i\mathrm{Re}\left(k_i^e r\right)} \tag{193}$$

for a large $\left|\mathrm{Im}\left(k_i^e r\right)\right|$. Here, the upper (lower) sign is for a positive (negative) $\mathrm{Im}\left(k_i^e r\right)$. See Appendix H for the derivation. Thus, one can expect that the conditions that result in a numerical instability for a given radius (r) have large $\left|\mathrm{Im}\left(k_1^e\right)\right|$ values. As expected, Figure 5a shows that a decrease in permeability leads to an increase in $\left|\mathrm{Im}\left(k_1^e\right)\right|$. Figure 5b shows that an increase in angular frequency also leads to an increase in $\left|\mathrm{Im}\left(k_1^e\right)\right|$, indicating that the attenuation is stronger for a higher frequency. In either case, a rough estimate of an increase in y values due to an increase Δr in the radius is given by

$$\left|\frac{y(r+\Delta r)}{y(r)}\right| \sim \left|\frac{j_\ell\left(k_1^e(r+\Delta r)\right)}{j_\ell\left(k_1^e r\right)}\right| \approx e^{\left|\mathrm{Im}\left(k_1^e \Delta r\right)\right|}. \tag{194}$$

Here, $\left|\mathrm{Im}\left(k_i^e r\right)\right| \gg 1$ and $\Delta r \ll r$ are assumed. In the case of a permeability of 10^{-14} m^2 and an angular frequency of 10^{-5} rad/s, where the appropriate thickness is about 3 ± 2 km, $\mathrm{Im}\left(k_1^e\right) = -5.81 \times 10^{-3}$ m^{-1} (see the left end of Figure 5a). If we substitute 3 km into Δr, we obtain $e^{\left|\mathrm{Im}\left(k_1^e \Delta r\right)\right|} = 3.71 \times 10^7$. Consequently, a rough estimate of the porous layer thickness Δr may be given by

$$\Delta r \sim \frac{\ln\left(3.71 \times 10^7\right)}{\left|\mathrm{Im}\left(k_1^e\right)\right|} \sim \frac{17}{\left|\mathrm{Im}\left(k_1^e\right)\right|}. \tag{195}$$

Figure 6 shows that Equation 195 provides an appropriate porous layer thickness under different parameter conditions. This is found to be true even if we change a parameter other than permeability and frequency (i.e., porosity, density, shear modulus, viscosity, …). Thus, if a porous layer has a large thickness and a large $\left|\mathrm{Im}\left(k_i^e\right)\right|$, such a layer should be divided into two layers, and Equation 195 can be used to obtain a first-order estimate on the boundary depth.

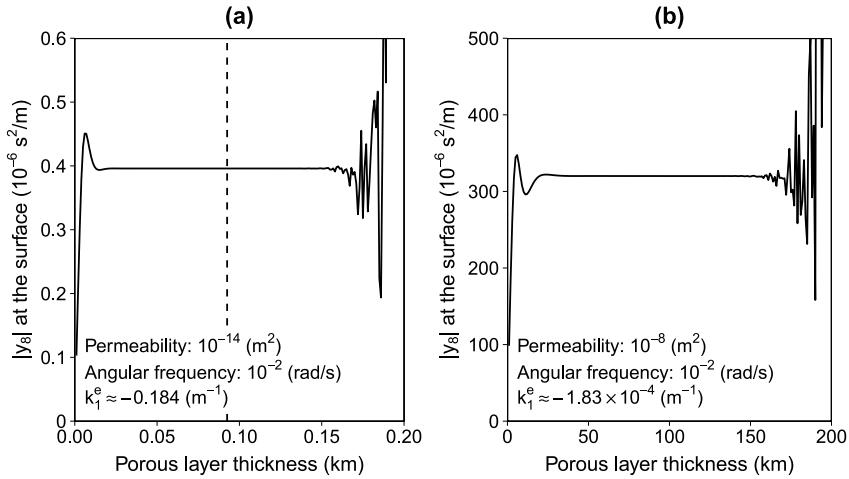

Figure 6. Dependence of the numerical stability and accuracy of the solution on the porous layer thickness under an angular frequency of 10^{-2} rad/s. The results for a permeability of (a) 10^{-14} m^2 and (b) 10^{-8} m^2 are shown. The vertical dashed lines indicate the guideline value given by Equation 195.

3.3. Multilayered, Radially Varying Model

Here, we investigate the effect of the radial variation in porosity on the energy dissipation rate in the porous layer. As an example, we consider tidal heating in the porous rocky core of the Saturnian satellite Enceladus. It is noted that the aim of this subsection is not to constrain parameter ranges that can explain the observed high heating rate of Enceladus; such an investigation is left for another study.

3.3.1. Model

We adopt a simple three-layered Enceladus model consisting of an ice shell, a subsurface ocean, and a rocky core. Table 2 lists the parameter values adopted.

3.3.1.1. Ice Shell

The outermost layer is assumed to be a nonporous, Maxwellian viscoelastic ice shell. Its density is the nominal value adopted in Hemingway and Mittal (2019), and the corresponding thickness is chosen. The bulk and shear moduli of polycrystalline ice are used (Petrenko & Whitworth, 1999).

The viscosity η_i is calculated from a simple Arrhenius-type rheology controlled by temperature T (e.g., Kamata & Nimmo, 2017):

$$\eta_i = \eta_{\rm ref} \exp\left(\frac{E_a}{R_g}\left(\frac{1}{T} - \frac{1}{T_{\rm ref}}\right)\right), \tag{196}$$

where $\eta_{\rm ref}$ is the reference viscosity, E_a is the creep activation energy, R_g is the gas constant, and $T_{\rm ref}$ is the reference temperature, respectively. The temperature profile in the ice shell is calculated by solving the one-dimensional steady-state thermal conduction equation without heating:

$$0 = \frac{1}{r^2}\frac{d}{dr}\left(r^2 k_{\rm th}\frac{dT}{dr}\right), \tag{197}$$

where kth is the thermal conductivity. We use a temperature-dependent thermal conductivity:

$$k_{\rm th}(T) = \frac{k^0_{\rm th}}{T}, \tag{198}$$

where $k^0_{\rm th} = 651\,{\rm W\,m^{-1}}$ (Petrenko & Whitworth, 1999). Then, the temperature profile $T(r)$ is given by

$$T(r) = T_s\left(\frac{T_o}{T_s}\right)^{\frac{r^{-1}-R_s^{-1}}{R_o^{-1}-R_s^{-1}}}, \tag{199}$$

Table 2
Model Parameters for the Three-Layer Enceladus Model

Quantity	Symbol	Value	Unit
Satellite mass[a]	M_s	1.080×10^{20}	kg
Satellite radius[b,c]	R_s	252.22	km
Ice shell thickness[c]	H_i	22	km
Subsurface ocean thickness[c]	H_o	37	km
Density of the ice shell[c]	ρ_i	925	kg m^{-3}
Density of the subsurface ocean[c]	ρ_o	1,020	kg m^{-3}
Density of rocky frame	ρ_s	2,800	kg m^{-3}
Density of pore fluid	ρ_f	$=\rho_o$	kg m^{-3}
Porosity	ϕ	Equation 201	–
Porosity at the core surface	$\phi_{\max}$	0.2375–0.4	–
Permeability	k	Equation 203	m^2
Bulk modulus of ice[d]	K_i	8.9	GPa
Bulk modulus of rocky frame	K_s	74.85	GPa
Bulk modulus of fluid	K_f	2.103	GPa
Shear modulus of ice[d]	μ_i	3.52	GPa
Shear modulus of rocky frame	μ_s	53.58	GPa
Viscosity of ice	η_i	Equation 196	Pa s
Viscosity of rocky frame	η_s	10^{20}	Pa s
Viscosity of pore fluid	η_f	1.860×10^{-3}	Pa s
Reference viscosity of ice	η_{ref}	10^{14}	Pa s
Reference temperature	T_{ref}	273	K
Activation energy of ice creep	E_a	6×10^4	J mol^{-1}
Harmonic degree	ℓ	2	–
Angular frequency[e]	ω	5.31×10^{-5}	rad s^{-1}
Eccentricity[e]	e	0.0047	–
Obliquity[e]	θ_o	4.5×10^{-4}	Degree
Porous-medium added-mass coefficient	C_a	Equation A1	–
Fluid viscosity correction factor[f]	F_f	Equation A2, with $\delta_p = 4$	–

[a]Iess et al. (2014). [b]Tajeddine et al. (2017). [c]Hemingway and Mittal (2019). [d]Petrenko and Whitworth (1999). [e]Matsuyama et al. (2018). [f]δ_p is the pore geometry factor.

where $R_o = R_s - H_i = 230.22$ km is the radius of the ice shell-subsurface ocean boundary, $T_s = T(R_s) = 75$ K is the surface temperature, and $T_o = T(R_o) = 273$ K is the temperature at the base of the ice shell. It is noted that we do not intend to obtain a precise heating rate profile under steady-state conditions. If so, one should include the heating term in Equation 197, and an iterative calculation would be necessary. Instead, we intend to obtain a simple viscosity profile that decreases significantly with depth. If one needs a precise heating rate profile, a more detailed and consistent thermal modeling is needed.

3.3.1.2. Subsurface Ocean

The intermediate layer is assumed to be an inviscid fluid layer. Similar to the ice shell, its density is the nominal value adopted in Hemingway and Mittal (2019), and the corresponding thickness is chosen.

3.3.1.3. Rocky Core

The bottom layer is assumed to be a microscopically homogeneous, porous, water-saturated, Maxwellian viscoelastic rocky core. The densities and thicknesses of the outer layers as well as the satellite mass and radius lead to

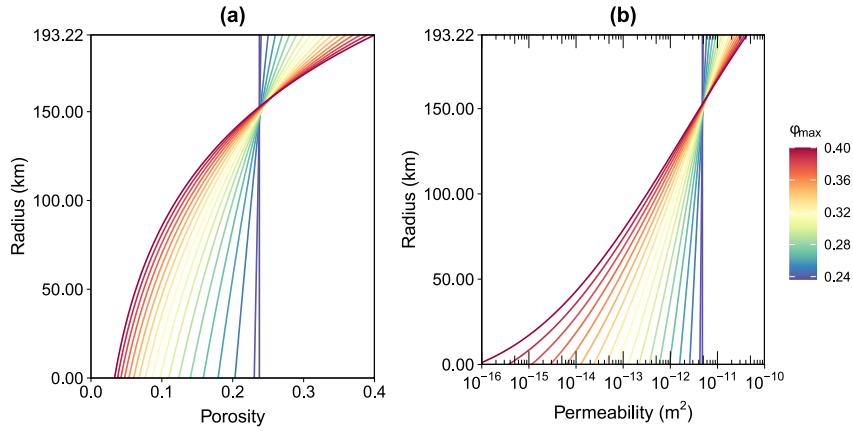

Figure 7. Radial profile of (a) the porosity and (b) permeability for different values of $\phi_{\max}$.

a bulk density of the rocky core of 2,377 kg m^{-3}. For simplicity, we use a solid frame density of 2,800 kg m^{-3}, and the fluid density is assumed to be the same as that of the subsurface ocean. These assumptions lead to a bulk porosity ϕ_{bulk} of 0.2375.

We consider porosity profiles that decrease exponentially with depth:

$$\phi(r) = \phi_{\max}\exp(\lambda_\phi(r - R_c)), \tag{200}$$

where $R_c = R_s - H_i - H_o = 193.22$ km is the core radius, $\phi_{\max}$ is the porosity at the core surface (i.e., $r = R_c$), and λ_ϕ is a constant, respectively. If we denote the porosity at the center (i.e., $\phi(r = 0) = \phi_{\max}e^{-\lambda_\phi R_c}$) as $\phi_{\min}$, Equation 200 can be written as

$$\phi(r) = \phi_{\min}\left(\frac{\phi_{\max}}{\phi_{\min}}\right)^{r/R_c}, \tag{201}$$

and the bulk porosity ϕ_{bulk} can be written as

$$\phi_{\text{bulk}} = 3\phi_{\min}\left[\ln\left(\frac{\phi_{\max}}{\phi_{\min}}\right)\right]^{-3}\left[\left(x^2 + 2x + 2\right)e^x\right]_{x=0}^{\ln(\phi_{\max}/\phi_{\min})}. \tag{202}$$

See Appendix I for the derivation. We consider different values of $\phi_{\max}$ between ϕ_{bulk} and 0.4, but ϕ_{bulk} is fixed to 0.2375. It is found that $\phi_{\min}$ takes a value between ϕ_{bulk} and 0.0333. The resulting porosity profiles are shown in Figure 7a.

For simplicity, the permeability k is calculated using the Kozeny-Carman equation calibrated for pure sands:

$$k = \frac{1}{5\rho_s\rho_f S_s^2}\frac{(\phi - \phi_t)^3}{(1 - \phi + \phi_t)^2}, \tag{203}$$

where $S_s = 14.8$ m^2 kg^{-1} is the specific surface and $\phi_t = 0.027$ is the percolation threshold porosity, respectively (Gleeson & Ingebritsen, 2017). The permeability profiles obtained are shown in Figure 7b. In the case of uniform porosity, Equation 203 leads to a permeability of 4.79×10^{-12} m^2. On the other hand, in the case of $\phi_{\max} = 0.4$, permeability varies between 8.01×10^{-17}–4.22×10^{-11} m^2. It is noted that permeability depends on many factors in addition to porosity; clays are much lower than those estimated from Equation 203, fault permeability is much higher than sediment permeability, and porosity-permeability relations found for granular materials do not work well for vesicular rocks in general (Gleeson & Ingebritsen, 2017; Saar & Manga, 1999). Thus, it is necessary to choose an appropriate model if one specifies a structural model for porous materials.

The bulk and shear moduli of the solid frame are calculated from the Hashin-Shtrikman bounds assuming that the solid frame is composed of a mixture of hydrated (antigorite) and unhydrated (olivine) silicate minerals. First, using the densities of these minerals (Christensen, 2004) as well as the assumed solid density ρ_s, the volume fraction ϕ_A of antigorite and that ϕ_O of olivine are calculated. Specifically, $\phi_A = 0.793$ and $\phi_O = 0.207$, respectively.

Second, the bulk and shear moduli of each component at zero pressure are calculated from pressure-dependent values listed in Christensen (2004). The Hashin-Shtrikman upper limits for the bulk and shear moduli are given by Hashin and Shtrikman (1963).

$$K_{\mathrm{up}} = K_2 + \frac{\phi_1}{\frac{1}{K_1 - K_2} + \frac{3\phi_2}{3K_2 + 4\mu_2}}, \tag{204}$$

$$\mu_{\mathrm{up}} = \mu_2 + \frac{\phi_1}{\frac{1}{\mu_1 - \mu_2} + \frac{6\phi_2(K_2 + 2\mu_2)}{5\mu_2(3K_2 + 4\mu_2)}}, \tag{205}$$

respectively, and the lower limits for the bulk and shear moduli are given by Hashin and Shtrikman (1963).

$$K_{\mathrm{low}} = K_1 + \frac{\phi_2}{\frac{1}{K_2 - K_1} + \frac{3\phi_1}{3K_1 + 4\mu_1}}, \tag{206}$$

$$\mu_{\mathrm{low}} = \mu_1 + \frac{\phi_2}{\frac{1}{\mu_2 - \mu_1} + \frac{6\phi_1(K_1 + 2\mu_1)}{5\mu_1(3K_1 + 4\mu_1)}}, \tag{207}$$

respectively, where ϕ_1 and ϕ_2 are the volume fractions of softer and stiffer materials, K_1 and K_2 are bulk moduli of softer and stiffer materials, and μ_1 and μ_2 are shear moduli for softer and stiffer materials, respectively. In our model, the softer and stiffer materials are antigorite and olivine, respectively. We adopt the means of these limits as the bulk and shear moduli, K_s and μ_s, of the solid:

$$K_s = \frac{1}{2}\left(K_{\mathrm{up}} + K_{\mathrm{low}}\right), \tag{208}$$

$$\mu_s = \frac{1}{2}\left(\mu_{\mathrm{up}} + \mu_{\mathrm{low}}\right). \tag{209}$$

The calculated values are listed in Table 2.

The drained bulk modulus and the effective shear modulus of the porous medium are also calculated using the Hashin-Shtrikman bounds. In this case, the softer and stiffer materials are void and solid, respectively. Consequently, $\phi_1 = \phi$, $\phi_2 = (1 - \phi)$, $K_1 = 0$, $K_2 = K_s$, $\mu_1 = 0$, and $\mu_2 = \mu_s$, respectively (Cheng, 2016). Then, we have

$$K_d = \frac{1 - \phi}{2}\left(\frac{1}{K_s} + \frac{3\phi}{4\mu_s}\right)^{-1}, \tag{210}$$

$$\mu = \frac{(1 - \phi)\mu_s}{2}\left(1 + \frac{6\phi(K_s + 2\mu_s)}{9K_s + 8\mu_s}\right)^{-1}. \tag{211}$$

Here, we again adopt the means of the upper and lower limits. In the case of uniform porosity, the drained bulk modulus and the effective shear modulus are 22.85 and 16.54 GPa, respectively. On the other hand, in the case of $\phi_{\mathrm{max}} = 0.4$, they range between 15.82–34.96 GPa and 11.51–25.07 GPa, respectively. The other poroelastic parameters, such as the Biot effective stress coefficient α and the undrained bulk modulus K_u, can be determined from other parameter values.

The parameters for pore fluids are calculated assuming that the pores are filled by sea water. First, the density ρ_f is assumed to be the same as the ocean density ρ_o. Second, using the formulation by Millero et al. (1982) with this density, the ocean temperature of 0°C, and the mean ocean pressure of 4.610 MPa, the salinity is calculated to be 22.18 g/kg. Then, the bulk modulus K_f and the viscosity η_f are calculated using the formulation by Millero et al. (1982) and by Sharqawy et al. (2010), respectively. The calculated values are listed in Table 2.

3.3.2. Results

As discussed above, a thick porous layer may need to be divided into porous and nonporous layers. In this model calculation, the porous core is thick (i.e., ~200 km), and the permeability can be low (i.e., $<10^{-16}$ m^2). Consequently, we first estimate the appropriate porous layer thickness and then conduct a numerical stability and accuracy test.

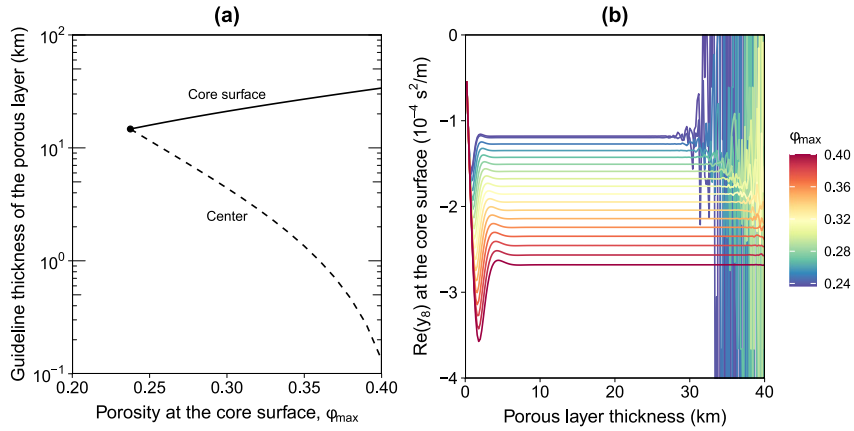

Figure 8. (a) The guideline thickness of the porous layer under different parameter conditions. The solid and dashed curves are obtained using parameter values at the core surface ($r = R_c$) and at the center ($r = 0$), respectively. The filled circle indicates the uniform porosity case. (b) Dependence of the numerical stability and accuracy of the solution on the porous layer thickness. The absolute value of y_8 at the core surface is shown.

Figure 8a shows the guideline thickness for the porous layer obtained using Equation 195. In the case of $\phi_{max} = 0.4$, the permeability at the center is lower than 10^{-16} m^2, leading to a guideline porous layer thickness of <1 km. Such a small thickness, however, is not appropriate because the fluid flow is concentrated near the core surface where the permeability is much higher and thus the permeable (drained) layer is even thicker than the uniform porosity case (i.e., >30 km). Figure 8b shows the results of the numerical stability and accuracy test, demonstrating that the porous layer thickness of ∼10–25 km can be used as a common porous layer thickness under all calculation conditions.

First, we compare the profile of the heating rate in the core for the porous and nonporous cases. Figure 9 shows the radial profile for the volumetric heating rate in the rocky core, assuming uniform porosity (i.e., $\phi_{max} = \phi_{bulk}$) and a porous layer thickness of 25 km. This figure shows that (a) the amount of heating due to fluid flow is several orders of magnitude higher than that of solid frame deformation, and (b) while heating due to fluid flow is concentrated near the surface, heating due to solid frame deformation is highest at the center. These results are consistent with previous studies (Liao et al., 2020; Rovira-Navarro et al., 2022). In this porous case, the total heating rate in the core is ∼0.5 MW. Figure 9 also shows the volumetric heating rate profile for the nonporous case. Here, the bulk and shear moduli for the solid constituent (i.e., K_s and μ_s, respectively) and a viscosity η_s of 4.6×10^{16} Pa s are used. This viscosity is chosen so that the total heating rate in the core becomes the same as that in the porous case. As shown in this figure, the porous and nonporous models lead to an opposite conclusion; the highest heating rate for the porous and nonporous cases is found at the surface and the center, respectively. Thus, a reduction in the viscosity does not mimic the effect of fluid flow, and a porous layer should not be modeled as a nonporous low-viscosity layer.

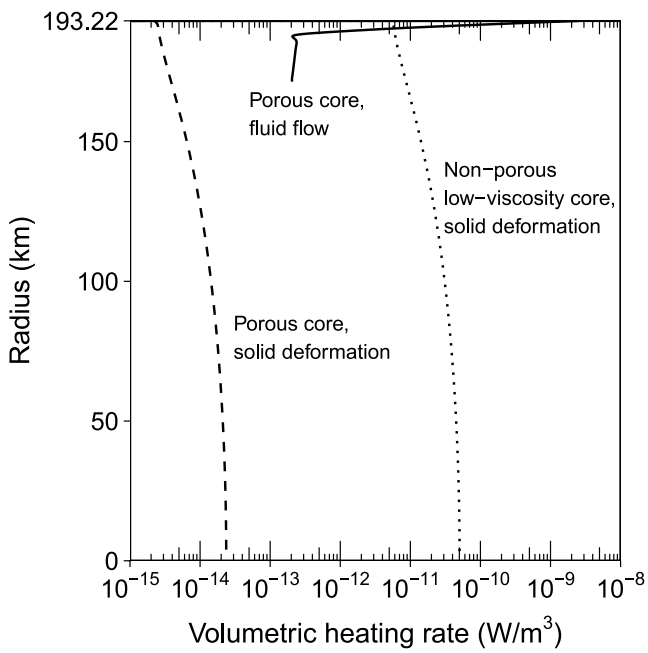

Figure 9. (a) The radial profiles of the volumetric heating rate in the core assuming uniform interior profiles. The solid and dashed lines represent energy dissipation due to fluid flow and solid-frame deformation, respectively. The dotted line shows the result for a nonporous, low-viscosity case, with $K = K_s$, $\mu = \mu_s$, and $\eta_s = 4.6 \times 10^{16}$ Pa s.

Next, we quantify the effect of radial variation in porosity. Figure 10a shows the radial profiles for the volumetric heating rate in the upper 20 km of the rocky core. Again, a porous layer thickness of 25 km is assumed. This figure shows that the thickness of the fluid flow region for $\phi_{max} = \phi_{bulk}$ is ∼5 km, while that for $\phi_{max} = 0.4$ is ∼10 km; an increase in near-surface porosity doubles the thickness of the fluid flow region. In addition, the heating rate due to fluid flow at 5 km depth for $\phi_{max} = \phi_{bulk}$ is $\sim 2 \times 10^{-13}$ W m^{-3}, while that for $\phi_{max} = 0.4$ is $\sim 3 \times 10^{-11}$ W m^{-3}; the latter is more than a hundredfold that of the former. Figure 10b shows the effect of an increase in near-surface porosity on the total heating rate in the core. The total heating rate for $\phi_{max} = \phi_{bulk}$ is ∼0.5 MW, while that for $\phi_{max} = 0.4$ is ∼1.9 MW; a fourfold increase is observed. Consequently, an increase in the maximum porosity increases the heating rate.

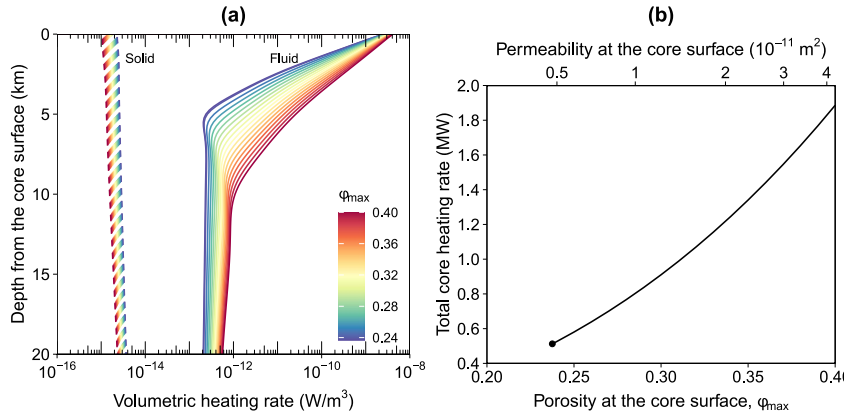

Figure 10. (a) The radial profiles of the volumetric heating rate in the core. The solid and dashed lines represent energy dissipation due to fluid flow and solid-frame deformation, respectively. (b) Tidal heating rate in the core as a function of the core surface porosity. The corresponding core surface permeability is also shown. The filled circle indicates the uniform porosity case.

In the above calculations, the bulk porosity ϕ_{bulk} is fixed to 0.2375. Consequently, a reduced fluid flow (and a decreased heating) in the deep interior for a high ϕ_{max} case is expected. Figure 7b shows that a porosity lower than ϕ_{bulk} can be seen at a depth of >∼40 km from the core surface. This is much deeper than the region of the fluid flow (i.e., <10 km, as mentioned above). Thus, a decrease in the porosity near the center does not contribute to reducing the total heating rate.

The above results demonstrate the importance of the use of a detailed interior structure model when quantifying deformation and energy dissipation in a planetary body. Thus, future works should consider a wide variety of interior profiles. In such works, the theory and numerical procedures described in this work can be used.

4. Concluding Remarks

This study provides poroviscoelastic gravitational theory. This theory combines the classic viscoelastic gravitational theory and the classic poroelastic theory. The governing equations, the ordinary differential equation system of y-functions, and boundary conditions are given. The analytical expression of linearly independent solutions for a uniform sphere is obtained using the eigenvalue approach.

It is found that a low permeability and a high frequency result in numerical instability. The solution for a homogeneous sphere is used to investigate this issue in detail. This instability can be avoided by dividing a porous layer into porous and nonporous layers. The guideline boundary depth for this division is also obtained.

Furthermore, tidal heating in the core of Enceladus is investigated using simple interior models. While a nonporous model can lead to the same total heating rate as the porous model by reducing the viscosity, the radial profile of the heating rate is completely different. In addition, a radial variation in porosity is found to have significant effects on the thickness of the fluid flow region and the heating rate. These results highlight the importance of detailed modeling of the interior structure when quantifying the tidal heating rate.

The theory provided in this study is based on classic theories by Love (1911) and Biot (1956a). Each theory has already been extended in many ways. For example, while this study assumes an isotropic medium, anisotropy can be introduced. In addition, while this study assumes that a porous solid frame is fully saturated with a single-component fluid, partial saturation and multicomponent fluids can be considered. Also, while this study adopts linearized equations in the Eulerian formulation, nonlinear equations and a Lagrangian formulation could be important. Such extensions to the theory are left for future studies.

Appendix A: Poroelastodynamic Parameters

A1. Added-Mass Coefficient C_a

When the frequency is high so that the inertial term (i.e., terms with ω^2) cannot be neglected, the effect of added mass needs to be considered. The porous-medium added-mass coefficient C_a depends on the shape of the body, which is unknown for planetary applications. For such a case,

$$C_a = \frac{\phi}{1-\phi}\left(\frac{1}{\sqrt{\phi}} - 1\right), \tag{A1}$$

where ϕ is the porosity, may be used as a guideline value (Equation 9.28 of Cheng, 2016).

A2. Fluid Viscosity Correction Factor F_f

When the frequency is high, the boundary layer effect on the motion of pore fluid, described by the fluid viscosity correction factor F_f, may need to be considered (e.g., Biot, 1956b). F_f depends on the geometry of the pores, which is unknown for planetary applications. For such a case,

$$F_f = \sqrt{1 + i\left(\frac{\delta_p}{4}\right)^2 \frac{\omega}{\omega_c}}, \tag{A2}$$

may be used as a guideline value (Equations 9.57, 9.66, and 9.68 of Cheng, 2016). Here, i is the imaginary number, δ_p is the pore geometry factor, ω is the (angular) frequency, and ω_c is the characteristic frequency, respectively. The characteristic frequency ω_c is given by

$$\omega_c = \frac{\phi \eta_f}{k \rho_f}, \tag{A3}$$

where η_f is the fluid viscosity, k is the intrinsic permeability, and ρ_f is the fluid density, respectively. The pore geometry factor δ_p is 3.2 for spheres and 6.3 for slits (Cheng, 2016). It is noted that the sign before the imaginary number is opposite to the formulation by Cheng (2016) who assumes a time factor of $e^{-i\omega t}$.

For simplicity, this study uses an intermediate value of $\delta_p = 4$, which leads to $F_f(\delta_p = 4) = \sqrt{1 + i\omega/\omega_c}$. It can be shown that $F_f(\delta_p = 4) \approx 1$ for $\omega/\omega_c < 0.1$. For $\phi = 0.1$, $\eta_f = 2 \times 10^{-3}$ Pa s (viscosity of water), $\rho_f = 1{,}000$ kg m^{-3} (density of water), and $k = 10^{-10}$ m^2 (typical crustal permeability), the characteristic frequency f_c ($=\omega_c/2\pi$) is ≈ 318 Hz. Consequently, under this parameter condition, one can assume $F_f = 1$ if deformation of a frequency f ($=\omega/2\pi$) less than $\sim$30 Hz is considered.

Appendix B: Derivation

B1. Ordinary Differential Equation System for the y Functions

In this study, a linearized equation system is adopted. Consequently, when deriving the differential equation system for y functions, we can consider deformation only due to a single forcing component. For example, Equation 50 can be replaced with

$$\widetilde{u}_i^s = \frac{x_i}{r} y_1(\ell, r) Y_\ell^m + r y_3(\ell, r) \frac{\partial Y_\ell^m}{\partial x_i} \tag{B1}$$

without loss of generality. Below we adopt this simplified definition of y functions.

First, the constitutive equation (Equation 5) and the pore pressure equation (Equation 6) are expressed using y functions. Specifically,

$$y_2 = \lambda_c \left(\frac{dy_1}{dr} + \frac{2}{r} y_1 - \frac{\ell(\ell+1)}{r} y_3\right) + 2\mu_c \frac{dy_1}{dr} - \alpha y_9, \tag{B2}$$

$$y_4 = \mu_c \left(\frac{dy_3}{dr} + \frac{1}{r} y_1 - \frac{1}{r} y_3\right), \tag{B3}$$

$$y_9 = -M\left[\alpha\left(\frac{dy_1}{dr} + \frac{2}{r} y_1 - \frac{\ell(\ell+1)}{r} y_3\right) + \phi\left(\frac{dy_8}{dr} + \frac{2}{r} y_8 - \frac{\ell(\ell+1)}{r} y_{10}\right)\right]. \tag{B4}$$

These equations yield Equations 57 and 59, and

$$\frac{dy_8}{dr} = -\frac{4\alpha\mu_c}{\phi(\lambda_c+2\mu_c)r}y_1 - \frac{\alpha}{\phi(\lambda_c+2\mu_c)}y_2 + \frac{2\ell(\ell+1)\alpha\mu_c}{\phi(\lambda_c+2\mu_c)r}y_3 - \frac{2}{r}y_8 - \frac{1}{\phi}\left(\frac{1}{M}+\frac{\alpha^2}{\lambda_c+2\mu_c}\right)y_9 + \frac{\ell(\ell+1)}{r}y_{10}. \tag{B5}$$

Second, the Poisson equation (Equation 22) is expressed using y functions. Its left-hand side is given by

$$\frac{\partial^2\widetilde{\psi}_1}{\partial x_i \partial x_i} = -\left(\frac{d^2y_5}{dr^2} + \frac{2}{r}\frac{dy_5}{dr} - \frac{\ell(\ell+1)}{r^2}y_5\right)Y_\ell^m, \tag{B6}$$

and its right-hand side is given by

$$\begin{aligned} &-4\pi G\left(\widetilde{u}_r^s\frac{d\rho}{dr} + \rho\widetilde{e}_{kk}^s + \widetilde{u}_r^{\mathrm{rel}}\frac{d}{dr}(\phi\rho_f) + \phi\rho_f\widetilde{e}_{kk}^{\mathrm{rel}}\right) \\ &= -4\pi G\left(\frac{d}{dr}(\rho y_1 + \phi\rho_f y_8) + \frac{2}{r}(\rho y_1 + \phi\rho_f y_8) - \frac{\ell(\ell+1)}{r}(\rho y_3 + \phi\rho_f y_{10})\right)Y_\ell^m. \end{aligned} \tag{B7}$$

By introducing y_6, which is a function of dy_5/dr, Equation B6 can be divided into two first-order ordinary differential equations (e.g., Alterman et al., 1959; Takeuchi & Saito, 1972). As mentioned in the main text, this study adopts a new definition of y_6 that is modified for the relative motion of fluid (i.e., Equation 56). Equation 56 leads to Equation 61 and substituting Equations 56, B6, and B7 into Equation 22 yields

$$\frac{dy_6}{dr} = \frac{4\pi(\ell+1)G\rho}{r}y_1 - \frac{4\pi\ell(\ell+1)G\rho}{r}y_3 + \frac{\ell-1}{r}y_6 + \frac{4\pi(\ell+1)G\phi\rho_f}{r}y_8 - \frac{4\pi\ell(\ell+1)G\phi\rho_f}{r}y_{10}. \tag{B8}$$

Third, the dynamic equation for the bulk motion (Equation 48) is expressed using y functions. Specifically,

$$\begin{aligned} 0 &= \frac{\partial\widetilde{\sigma}_{ij}}{\partial x_j} + \omega^2\left(\rho\widetilde{u}_i^s + \phi\rho_f\widetilde{u}_i^{\mathrm{rel}}\right) - \rho\frac{\partial}{\partial x_i}\left(g\widetilde{u}_r^s\right) - \phi\rho_f\frac{\partial}{\partial x_i}\left(g\widetilde{u}_r^{\mathrm{rel}}\right) - \rho\frac{\partial\widetilde{\psi}_1}{\partial x_i} + \frac{gx_i}{r}\left(\rho\widetilde{e}_{kk}^s + \phi\rho_f\widetilde{e}_{kk}^{\mathrm{rel}}\right) \\ &= \frac{\partial\widetilde{\sigma}_{ij}}{\partial x_j} + \frac{x_i}{r}\left\{\omega^2(\rho y_1 + \phi\rho_f y_8) - \rho\frac{d}{dr}(gy_1) - \phi\rho_f\frac{d}{dr}(gy_8) + \rho\frac{dy_5}{dr} + \rho g\left(\frac{dy_1}{dr} + \frac{2}{r}y_1 - \frac{\ell(\ell+1)}{r}y_3\right)\right. \\ &\quad \left. + \phi\rho_f g\left(\frac{dy_8}{dr} + \frac{2}{r}y_8 - \frac{\ell(\ell+1)}{r}y_{10}\right)\right\}Y_\ell^m + r\left(\omega^2(\rho y_3 + \phi\rho_f y_{10}) - \frac{g}{r}(\rho y_1 + \phi\rho_f y_8) + \frac{\rho}{r}y_5\right)\frac{\partial Y_\ell^m}{\partial x_i}. \end{aligned} \tag{B9}$$

Here, the divergence of the stress tensor is given by

$$\begin{aligned} \frac{\partial\widetilde{\sigma}_{ij}}{\partial x_j} &= \frac{x_i}{r}\left[\frac{dy_2}{dr} - \frac{\ell(\ell+1)}{r}y_4 + \frac{2\mu_c}{r}\left(2\frac{dy_1}{dr} - \frac{2}{r}y_1 + \frac{\ell(\ell+1)}{r}y_3\right)\right]Y_\ell^m \\ &\quad + r\left(\frac{1}{r}y_2 - \frac{2\mu_c}{r}\frac{dy_1}{dr} + \frac{dy_4}{dr} + \frac{3}{r}y_4 + \frac{2\mu_c}{r^2}\left[y_1 + \left(1-\ell-\ell^2\right)y_3\right]\right)\frac{\partial Y_\ell^m}{\partial x_i}. \end{aligned} \tag{B10}$$

See Appendix B4 for the derivation. Consequently,

$$\begin{aligned} 0 &= \frac{x_i}{r}\left\{\omega^2(\rho y_1 + \phi\rho_f y_8) - \rho\frac{d}{dr}(gy_1) - \phi\rho_f\frac{d}{dr}(gy_8) + \rho\frac{dy_5}{dr}\right. \\ &\quad + \rho g\left(\frac{dy_1}{dr} + \frac{2}{r}y_1 - \frac{\ell(\ell+1)}{r}y_3\right) + \phi\rho_f g\left(\frac{dy_8}{dr} + \frac{2}{r}y_8 - \frac{\ell(\ell+1)}{r}y_{10}\right) \\ &\quad \left. + \frac{dy_2}{dr} - \frac{\ell(\ell+1)}{r}y_4 + \frac{2\mu_c}{r}\left(2\frac{dy_1}{dr} - \frac{2}{r}y_1 + \frac{\ell(\ell+1)}{r}y_3\right)\right\}Y_\ell^m \\ &\quad + r\left(\omega^2(\rho y_3 + \phi\rho_f y_{10}) - \frac{g}{r}(\rho y_1 + \phi\rho_f y_8) + \frac{\rho}{r}y_5 + \frac{1}{r}y_2\right. \\ &\quad \left. - \frac{2\mu_c}{r}\frac{dy_1}{dr} + \frac{dy_4}{dr} + \frac{3}{r}y_4 + \frac{2\mu_c}{r^2}\left[y_1 + \left(1-\ell-\ell^2\right)y_3\right]\right)\frac{\partial Y_\ell^m}{\partial x_i}. \end{aligned} \tag{B11}$$

Then, two equations are obtained:

$$0 = \omega^2(\rho y_1 + \phi\rho_f y_8) - \rho\frac{d}{dr}(g y_1) - \phi\rho_f\frac{d}{dr}(g y_8) + \rho\frac{dy_5}{dr} + \rho g\left(\frac{dy_1}{dr} + \frac{2}{r}y_1 - \frac{\ell(\ell+1)}{r}y_3\right) + \phi\rho_f g\left(\frac{dy_8}{dr} + \frac{2}{r}y_8 - \frac{\ell(\ell+1)}{r}y_{10}\right) + \frac{dy_2}{dr} - \frac{\ell(\ell+1)}{r}y_4 + \frac{2\mu_c}{r}\left(2\frac{dy_1}{dr} - \frac{2}{r}y_1 + \frac{\ell(\ell+1)}{r}y_3\right) \tag{B12}$$

and

$$0 = \omega^2(\rho y_3 + \phi\rho_f y_{10}) - \frac{g}{r}(\rho y_1 + \phi\rho_f y_8) + \frac{\rho}{r}y_5 + \frac{1}{r}y_2 - \frac{2\mu_c}{r}\frac{dy_1}{dr} + \frac{dy_4}{dr} + \frac{3}{r}y_4 + \frac{2\mu_c}{r^2}\left[y_1 + \left(1 - \ell - \ell^2\right)y_3\right]. \tag{B13}$$

Equation B12 yields

$$\begin{aligned}\frac{dy_2}{dr} &= -\omega^2\left(\rho y_1 + \phi\rho_f y_8\right) + \rho\frac{d}{dr}(g y_1) + \phi\rho_f\frac{d}{dr}(g y_8) - \rho\frac{dy_5}{dr} - \rho g\left(\frac{dy_1}{dr} + \frac{2}{r}y_1 - \frac{\ell(\ell+1)}{r}y_3\right)\\ &\quad -\phi\rho_f g\left(\frac{dy_8}{dr} + \frac{2}{r}y_8 - \frac{\ell(\ell+1)}{r}y_{10}\right) + \frac{\ell(\ell+1)}{r}y_4 - \frac{2\mu_c}{r}\left(2\frac{dy_1}{dr} - \frac{2}{r}y_1 + \frac{\ell(\ell+1)}{r}y_3\right)\\ &= \left(-\omega^2\rho - \frac{4\rho g}{r} + \frac{12K_d\mu_c}{(\lambda_c+2\mu_c)r^2}\right)y_1 - \frac{4\mu_c}{(\lambda_c+2\mu_c)r}y_2 + \frac{\ell(\ell+1)}{r}\left(\rho g - \frac{6K_d\mu_c}{(\lambda_c+2\mu_c)r}\right)y_3\\ &\quad + \frac{\ell(\ell+1)}{r}y_4 + \frac{(\ell+1)\rho}{r}y_5 - \rho y_6 + \left(-\omega^2\phi\rho_f - \frac{4\phi\rho_f g}{r}\right)y_8 - \frac{4\alpha\mu_c}{(\lambda_c+2\mu_c)r}y_9 + \frac{\ell(\ell+1)\phi\rho_f g}{r}y_{10}.\end{aligned} \tag{B14}$$

On the other hand, Equation B13 yields

$$\begin{aligned}\frac{dy_4}{dr} &= \frac{2\mu_c}{r}\frac{dy_1}{dr} - \omega^2(\rho y_3 + \phi\rho_f y_{10}) + \frac{g}{r}(\rho y_1 + \phi\rho_f y_8) - \frac{\rho}{r}y_5 - \frac{1}{r}y_2\\ &\quad -\frac{3}{r}y_4 - \frac{2\mu_c}{r^2}\left[y_1 + \left(1 - \ell - \ell^2\right)y_3\right]\\ &= \left(\frac{\rho g}{r} - \frac{6K_d\mu_c}{(\lambda_c+2\mu_c)r^2}\right)y_1 - \frac{\lambda_c}{(\lambda_c+2\mu_c)r}y_2 + \left[-\omega^2\rho + \frac{2\mu_c}{r^2}\left(\frac{2\ell(\ell+1)(\lambda_c+\mu_c)}{\lambda_c+2\mu_c} - 1\right)\right]y_3\\ &\quad -\frac{3}{r}y_4 - \frac{\rho}{r}y_5 + \frac{\phi\rho_f g}{r}y_8 + \frac{2\alpha\mu_c}{(\lambda_c+2\mu_c)r}y_9 - \omega^2\phi\rho_f y_{10}.\end{aligned} \tag{B15}$$

Finally, the dynamic equation for the fluid (Equation 49) is expressed using y functions. Specifically,

$$\begin{aligned}0 &= -i\frac{\omega\phi\eta_f F_f}{k}\widetilde{u}_i^{\mathrm{rel}} - \frac{\partial\widetilde{p}_f}{\partial x_i} - \rho_f\frac{\partial}{\partial x_i}\left[g\left(\widetilde{u}_r^{\mathrm{rel}} + \widetilde{u}_r^{s}\right)\right] - \rho_f\frac{\partial\widetilde{\psi}_1}{\partial x_i}\\ &\quad + \frac{\rho_f g x_i}{r}\left(\widetilde{u}_r^{\mathrm{rel}}\frac{d\phi}{dr} + \widetilde{e}_{kk}^{\mathrm{rel}} + \widetilde{e}_{kk}^{s}\right) + \omega^2\rho_f\left[\left(1 + \frac{1-\phi}{\phi}C_a\right)\widetilde{u}_i^{\mathrm{rel}} + \widetilde{u}_i^{s}\right]\\ &= \frac{x_i}{r}\left\{\left(\omega^2\rho_f + \frac{2\rho_f g}{r}\right)y_1 - \frac{\ell(\ell+1)\rho_f g}{r}y_3 + \left[\omega^2\rho_f\left(1 + \frac{1-\phi}{\phi}C_a\right)\right.\right.\\ &\quad \left.-i\frac{\omega\phi\eta_f F_f}{k} + \frac{2\rho_f g}{r} + \rho_f g\frac{d\phi}{dr}\right]y_8 - \frac{\ell(\ell+1)\rho_f g}{r}y_{10} - \frac{dy_9}{dr}\\ &\quad -\rho_f\frac{d}{dr}[g(y_8 + y_1)] + \rho_f\left(g\frac{dy_1}{dr} + \frac{dy_5}{dr} + g\frac{dy_8}{dr}\right)\Big\}Y_\ell^m\\ &\quad + r\left\{-\frac{\rho_f g}{r}y_1 + \omega^2\rho_f y_3 + \frac{\rho_f}{r}y_5 - \frac{\rho_f g}{r}y_8 - \frac{y_9}{r} + \left[\omega^2\rho_f\left(1 + \frac{1-\phi}{\phi}C_a\right) - i\frac{\omega\phi\eta_f F_f}{k}\right]y_{10}\right\}\frac{\partial Y_\ell^m}{\partial x_i}.\end{aligned} \tag{B16}$$

The term proportional to Y_ℓ leads to

$$\begin{aligned}\frac{dy_9}{dr} &= \rho_f\left(\omega^2 + \frac{4g}{r}\right)y_1 - \frac{\ell(\ell+1)\rho_f g}{r}y_3 - \frac{(\ell+1)\rho_f}{r}y_5 + \rho_f y_6\\ &\quad + \left[\omega^2\rho_f\left(1 + \frac{1-\phi}{\phi}C_a\right) - i\frac{\omega\phi\eta_f F_f}{k} + \frac{4\rho_f g}{r} + \rho_f g\frac{d\phi}{dr} - 4\pi G\rho_f(\rho - \phi\rho_f)\right]y_8 - \frac{\ell(\ell+1)\rho_f g}{r}y_{10}.\end{aligned} \tag{B17}$$

On the other hand, the term proportional to $\partial Y_\ell/\partial x_i$ yields

$$y_{10} = \frac{\rho_f g y_1 - \omega^2 \rho_f r y_3 - \rho_f y_5 + \rho_f g y_8 + y_9}{\omega^2 \left[\rho_f \left(1 + \frac{1-\phi}{\phi} C_a\right) - i \frac{\phi \eta_f F_f}{\omega k}\right] r}. \tag{B18}$$

Substitution of Equation B18 into Equations B14, B15, B8, B5, and B17 leads to Equations 58, 60 and 62–64, respectively.

B2. Fundamental Equations for the Homogeneous Solution

If one differentiates Equation B13 (multiplied by r) and subtracts Equation B12 from the result, one can obtain Equation 72. Additionally, if one differentiates Equation B12 (multiplied by r) and adds multiples of Equation B13 to the results to give $\omega^2 \rho X^s$, one can obtain Equation 73. On the other hand, if one differentiates Equation 66 (multiplied by r) and subtracts Equation B17 from the result, one can obtain Equation 74. Additionally, if one differentiates Equation B17 and adds multiples of Equations B17 and 66 to the results to give $\omega^2 \rho_f X^s$, one can obtain Equation 75.

B3. Total Heating Rate

The radial integration of the volumetric heating rate h can be obtained as follows (e.g., Takeuchi & Saito, 1972; Tobie et al., 2005). For any smooth function x within a layer (i.e., $r_l < r < r_u$), one can obtain

$$\begin{aligned}
\frac{d}{dr}\left(r^2 x_1 y_2\right) &= \left(r^2 \frac{dx_1}{dr} + 2r x_1\right) y_2 + r^2 x_1 \frac{dy_2}{dr} \\
&= \left(r^2 \frac{dx_1}{dr} + 2r x_1\right)\left[\lambda_c \left(\frac{dy_1}{dr} + \frac{2}{r} y_1 - \frac{\ell(\ell+1)}{r} y_3\right) + 2\mu_c \frac{dy_1}{dr} - \alpha y_9\right] \\
&\quad + r^2 x_1 \left[-\omega^2(\rho y_1 + \phi \rho_f y_8) + \rho\left(\frac{\ell+1}{r} y_5 - y_6\right) - \rho g \left(\frac{4}{r} y_1 - \frac{\ell(\ell+1)}{r} y_3\right)\right. \\
&\quad \left. - \phi \rho_f g \left(\frac{4}{r} y_8 - \frac{\ell(\ell+1)}{r} y_{10}\right) + \frac{\ell(\ell+1)}{r} y_4 - \frac{2\mu_c}{r}\left(2\frac{dy_1}{dr} - \frac{2}{r} y_1 + \frac{\ell(\ell+1)}{r} y_3\right)\right],
\end{aligned} \tag{B19}$$

$$\begin{aligned}
\frac{d}{dr}\left(r^2 x_3 y_4\right) &= \left(r^2 \frac{dx_3}{dr} + 2r x_3\right) y_4 + r^2 x_3 \frac{dy_4}{dr} \\
&= r^2 \frac{dx_3}{dr} y_4 + r x_3 \left(2\mu_c \frac{dy_1}{dr} - \omega^2 r(\rho y_3 + \phi \rho_f y_{10}) + g(\rho y_1 + \phi \rho_f y_8) - \rho y_5 - y_2\right. \\
&\quad \left. - y_4 - \frac{2\mu_c}{r}\left[y_1 + \left(1 - \ell - \ell^2\right) y_3\right]\right),
\end{aligned} \tag{B20}$$

$$\begin{aligned}
\frac{d}{dr}\left(r^2 x_5 y_6\right) &= \left(r^2 \frac{dx_5}{dr} + 2r x_5\right) y_6 + r^2 x_5 \frac{dy_6}{dr} \\
&= r^2 \left(\frac{dx_5}{dr} + \frac{\ell+1}{r} x_5\right) y_6 + 4\pi(\ell+1) G r x_5 (\rho y_1 - \ell \rho y_3 + \phi \rho_f y_8 - \ell \phi \rho_f y_{10}),
\end{aligned} \tag{B21}$$

$$\begin{aligned}
\frac{d}{dr}\left(r^2 x_8 y_9\right) &= \left(r^2 \frac{dx_8}{dr} + 2r x_8\right) y_9 + r^2 x_8 \frac{dy_9}{dr} \\
&= \left(r^2 \frac{dx_8}{dr} + 2r x_8\right) y_9 \\
&\quad + r^2 x_8 \left[\rho_f \left(\omega^2 + \frac{4g}{r}\right) y_1 - \frac{\ell(\ell+1)\rho_f g}{r} y_3 - \frac{(\ell+1)\rho_f}{r} y_5 + \rho_f y_6\right. \\
&\quad \left. + \left(\omega^2 \rho_e + \frac{4\rho_f g}{r} + \rho_f g \frac{d\phi}{dr} - 4\pi G \rho_f (\rho - \phi \rho_f)\right) y_8 - \frac{\ell(\ell+1)\rho_f g}{r} y_{10}\right].
\end{aligned} \tag{B22}$$

If $x_i = y_i^*$,

$$\begin{aligned}\frac{d}{dr}\left(r^2 y_1^* y_2\right) &= \left(r^2\frac{dy_1^*}{dr}+2ry_1^*\right)\left[\lambda_c\left(\frac{dy_1}{dr}+\frac{2}{r}y_1-\frac{\ell(\ell+1)}{r}y_3\right)+2\mu_c\frac{dy_1}{dr}-\alpha y_9\right]\\ &\quad+r^2 y_1^*\left[-\omega^2(\rho y_1+\phi\rho_f y_8)+\rho\left(\frac{\ell+1}{r}y_5-y_6\right)\right.\\ &\quad-\rho g\left(\frac{4}{r}y_1-\frac{\ell(\ell+1)}{r}y_3\right)-\phi\rho_f g\left(\frac{4}{r}y_8-\frac{\ell(\ell+1)}{r}y_{10}\right)\\ &\quad\left.+\frac{\ell(\ell+1)}{r}y_4-\frac{2\mu_c}{r}\left(2\frac{dy_1}{dr}-\frac{2}{r}y_1+\frac{\ell(\ell+1)}{r}y_3\right)\right],\\ &= K_d H_K^\ell+\frac{\mu_c}{3}\left|2r\frac{dy_1}{dr}-2y_1+\ell(\ell+1)y_3\right|^2-\mu_c\ell^2(\ell+1)^2|y_3|^2\\ &\quad-\omega^2\rho|ry_1|^2-4\rho g r|y_1|^2\\ &\quad+\ell(\ell+1)\left[\rho g r y_1^* y_3+ry_1^* y_4+2\mu_c y_3^* y_1+ry_3^*\left(y_2-2\mu_c\frac{dy_1}{dr}\right)\right]\\ &\quad+\rho r\left[(\ell+1)y_1^* y_5-ry_1^* y_6\right]\\ &\quad-\omega^2\phi\rho_f r^2 y_1^* y_8-\alpha r^2\left(\frac{dy_1^*}{dr}+\frac{2}{r}y_1^*-\frac{\ell(\ell+1)}{r}y_3^*\right)y_9\\ &\quad-\phi\rho_f g r y_1^*(4y_8-\ell(\ell+1)y_{10}),\end{aligned}\tag{B23}$$

$$\begin{aligned}\frac{d}{dr}\left(r^2 y_3^* y_4\right) &= r^2\frac{dy_3^*}{dr}y_4+ry_3^*\left(2\mu_c\frac{dy_1}{dr}-\omega^2 r(\rho y_3+\phi\rho_f y_{10})+g(\rho y_1+\phi\rho_f y_8)\right.\\ &\quad\left.-\rho y_5-y_2-y_4-\frac{2\mu_c}{r}\left[y_1+\left(1-\ell-\ell^2\right)y_3\right]\right)\\ &= \mu_c\left|\frac{r}{\mu_c}y_4\right|^2-2[1-\ell(\ell+1)]\mu_c|y_3|^2-\omega^2\rho|ry_3|^2\\ &\quad+\rho g r y_3^* y_1-ry_1^* y_4-2\mu_c y_3^* y_1-ry_3^*\left(y_2-2\mu_c\frac{dy_1}{dr}\right)-\rho ry_3^* y_5+\phi\rho_f ry_3^*\left(gy_8-\omega^2 ry_{10}\right),\end{aligned}\tag{B24}$$

$$\begin{aligned}\frac{d}{dr}\left(r^2 y_5^* y_6\right) &= r^2\left(\frac{dy_5^*}{dr}+\frac{\ell+1}{r}y_5^*\right)y_6\\ &\quad+4\pi(\ell+1)Gry_5^*(\rho y_1-\ell\rho y_3+\phi\rho_f y_8-\ell\phi\rho_f y_{10})\\ &= |ry_6|^2+4\pi G\rho r\left[(\ell+1)y_5^* y_1+ry_1^* y_6\right]-4\pi\ell(\ell+1)G\rho ry_5^* y_3\\ &\quad+4\pi G\phi\rho_f r\left[(\ell+1)y_5^* y_8-\ell(\ell+1)y_5^* y_{10}+ry_8^* y_6\right],\end{aligned}\tag{B25}$$

$$\begin{aligned}\frac{d}{dr}\left(r^2 y_8^* y_9\right) &= r^2\left(\frac{dy_8^*}{dr}+\frac{2}{r}y_8^*\right)y_9+r^2 y_8^*\frac{dy_9}{dr}\\ &= r^2\left(\frac{dy_8^*}{dr}+\frac{2}{r}y_8^*\right)y_9\\ &\quad+r^2 y_8^*\left[\left(\omega^2\rho_f+\frac{4\rho_f g}{r}\right)y_1-\frac{\ell(\ell+1)\rho_f g}{r}y_3-\frac{(\ell+1)\rho_f}{r}y_5+\rho_f y_6\right.\\ &\quad\left.+\left(\omega^2\rho_e+\frac{4\rho_f g}{r}+\rho_f g\frac{d\phi}{dr}-4\pi G\rho_f(\rho-\phi\rho_f)\right)y_8-\frac{\ell(\ell+1)\rho_f g}{r}y_{10}\right]\\ &= -\frac{M}{\phi}\left|\frac{r}{M}y_9\right|^2+\omega^2\rho_e\left[|ry_8|^2+\ell(\ell+1)|ry_{10}|^2\right]\\ &\quad-\ell(\ell+1)\rho_f g r\left(y_8^* y_{10}+y_{10}^* y_8\right)\\ &\quad+\omega^2\rho_f r^2 y_8^* y_1-\frac{\alpha r^2}{\phi}\left(\frac{dy_1^*}{dr}+\frac{2}{r}y_1^*-\frac{\ell(\ell+1)}{r}y_3^*\right)y_9\\ &\quad+\rho_f g r\left(4y_8^*-\ell(\ell+1)y_{10}^*\right)y_1-\ell(\ell+1)\rho_f r\left(gy_8^*-\omega^2 ry_{10}^*\right)y_3\\ &\quad-\rho_f r\left[(\ell+1)y_8^* y_5-\ell(\ell+1)y_{10}^* y_5-ry_8^* y_6\right]\\ &\quad+\left(\frac{4\rho_f g}{r}+\rho_f g\frac{d\phi}{dr}-4\pi G\rho_f(\rho-\phi\rho_f)\right)|ry_8|^2.\end{aligned}\tag{B26}$$

Consequently,

$$\begin{aligned}
&\frac{d}{dr}\left(r^2 y_1^* y_2\right) + \ell(\ell+1)\frac{d}{dr}\left(r^2 y_3^* y_4\right) + \frac{1}{4\pi G}\frac{d}{dr}\left(r^2 y_5^* y_6\right) - \frac{d}{dr}\left(\phi r^2 y_8^* y_9\right) \\
&= K_d H_K^\ell + \mu_c H_\mu^\ell + M H_M^\ell + i\omega\eta_f \mathrm{Re}(F_f) H_\eta^\ell \\
&\quad - \omega^2\rho\left(|r y_1|^2 + \ell(\ell+1)|r y_3|^2\right) \\
&\quad - \omega^2\phi\,\mathrm{Re}(\rho_e)\left(|r y_8|^2 + \ell(\ell+1)|r y_{10}|^2\right) \\
&\quad - 2\omega^2\phi\rho_f r^2\,\mathrm{Re}\left(y_1^* y_8 + \ell(\ell+1) y_3^* y_{10}\right) \\
&\quad - 4\rho g r|y_1|^2 + \frac{1}{4\pi G}|r y_6|^2 \\
&\quad - \phi\left(\frac{4\rho_f g}{r} - 4\pi G\rho_f(\rho - \phi\rho_f) + \rho_f g\frac{d\phi}{dr}\right)|r y_8|^2 \\
&\quad + 2\ell(\ell+1) g r\,\mathrm{Re}\left(\rho y_1^* y_3 + \phi\rho_f y_3^* y_8 + \phi\rho_f y_1^* y_{10} + \phi\rho_f y_8^* y_{10}\right) \\
&\quad - 8\phi\rho_f g r\,\mathrm{Re}\left(y_1^* y_8\right) - \frac{d\phi}{dr} r^2\,\mathrm{Re}\left(y_8^* y_9\right) \\
&\quad + 2(\ell+1) r\,\mathrm{Re}\left(y_5^*\left[\rho(y_1 - \ell y_3) + \phi\rho_f(y_8 - \ell y_{10})\right]\right).
\end{aligned} \tag{B27}$$

Thus,

$$\begin{aligned}
&\frac{d}{dr}\left[r^2 \mathrm{Im}\left(y_1^* y_2 + \ell(\ell+1) y_3^* y_4 + \frac{1}{4\pi G} y_5^* y_6 - \phi y_8^* y_9\right)\right] \\
&\quad = \mathrm{Im}\left(K_d H_K^\ell + \mu_c H_\mu^\ell + M H_M^\ell + \omega\eta_f \mathrm{Re}(F_f) H_\eta^\ell\right).
\end{aligned} \tag{B28}$$

Equations B28 and 176 lead to Equation 177.

B4. Divergence of Stress Tensor

From Equation 5, the divergence of the stress tensor is given by

$$\begin{aligned}
\frac{\partial\tilde{\sigma}_{ij}}{\partial x_j} &= \frac{\partial}{\partial x_j}\left(\lambda_c \tilde{e}_{kk}^s \delta_{ij} + 2\mu_c \tilde{e}_{ij}^s - \alpha\tilde{p}_f \delta_{ij}\right) \\
&= \frac{\partial}{\partial x_i}\left(\lambda_c \tilde{e}_{kk}^s - \alpha\tilde{p}_f\right) + \frac{\partial}{\partial x_j}\left(2\mu_c \tilde{e}_{ij}^s\right).
\end{aligned} \tag{B29}$$

The first term of the right-hand side of this equation is given by

$$\begin{aligned}
\frac{\partial}{\partial x_i}\left(\lambda_c \tilde{e}_{kk}^s - \alpha\tilde{p}_f\right) &= \frac{\partial}{\partial x_i}\left(y_2 Y_\ell - 2\mu_c \frac{dy_1}{dr} Y_\ell\right) \\
&= \frac{x_i}{r}\frac{d}{dr}\left(y_2 - 2\mu_c\frac{dy_1}{dr}\right) Y_\ell + r\left(\frac{1}{r} y_2 - \frac{2\mu_c}{r}\frac{dy_1}{dr}\right)\frac{\partial Y_\ell}{\partial x_i},
\end{aligned} \tag{B30}$$

and the second term is given by

$$\frac{\partial}{\partial x_j}\left(2\mu_c \tilde{e}_{ij}^s\right) = \mu_c\left(\frac{\partial}{\partial x_i}\tilde{e}_{kk}^s + \frac{\partial}{\partial x_j}\frac{\partial}{\partial x_j}\tilde{u}_i^s\right) + \frac{1}{r}\frac{d\mu_c}{dr}\left(x_j\frac{\partial}{\partial x_j}\tilde{u}_i^s + x_j\frac{\partial}{\partial x_i}\tilde{u}_j^s\right). \tag{B31}$$

Here,

$$\begin{aligned}
\frac{\partial}{\partial x_j}\frac{\partial}{\partial x_j}\tilde{u}_i^s &= \frac{x_i}{r}\left(\frac{d^2 y_1}{dr^2} + \frac{2}{r}\frac{dy_1}{dr} - \frac{2 + \ell(\ell+1)}{r^2} y_1 + \frac{2\ell(\ell+1)}{r^2} y_3\right) Y_\ell \\
&\quad + r\left(\frac{d^2 y_3}{dr^2} + \frac{2}{r}\frac{dy_3}{dr} + \frac{2}{r^2} y_1 - \frac{\ell(\ell+1)}{r^2} y_3\right)\frac{\partial Y_\ell}{\partial x_i},
\end{aligned} \tag{B32}$$

and

$$x_j\frac{\partial}{\partial x_j}\tilde{u}_i^s + x_j\frac{\partial}{\partial x_i}\tilde{u}_j^s = 2x_i\frac{dy_1}{dr} Y_\ell + r\left(r\frac{dy_3}{dr} + y_1 - y_3\right)\frac{\partial Y_\ell}{\partial x_i}. \tag{B33}$$

Consequently,

$$\begin{aligned}\frac{\partial}{\partial x_j}\left(2\mu_c\widetilde{e}^{s}_{ij}\right) &= \mu_c\frac{x_i}{r}\frac{d}{dr}\left(\frac{dy_1}{dr}+\frac{2}{r}y_1-\frac{\ell(\ell+1)}{r}y_3\right)Y_\ell\\ &+\mu_c\frac{x_i}{r}\left(\frac{d^2y_1}{dr^2}+\frac{2}{r}\frac{dy_1}{dr}-\frac{2+\ell(\ell+1)}{r^2}y_1+\frac{2\ell(\ell+1)}{r^2}y_3\right)Y_\ell+\frac{1}{r}\frac{d\mu_c}{dr}\left(2x_i\frac{dy_1}{dr}\right)Y_\ell\\ &+\mu_c\left(\frac{dy_1}{dr}+\frac{2}{r}y_1-\frac{\ell(\ell+1)}{r}y_3\right)\frac{\partial Y_\ell}{\partial x_i}+\mu_c\left(r\frac{d^2y_3}{dr^2}+2\frac{dy_3}{dr}+\frac{2}{r}y_1-\frac{\ell(\ell+1)}{r}y_3\right)\frac{\partial Y_\ell}{\partial x_i}\\ &+\frac{d\mu_c}{dr}\left(r\frac{dy_3}{dr}+y_1-y_3\right)\frac{\partial Y_\ell}{\partial x_i}\\ &=\frac{x_i}{r}\left[\frac{d}{dr}\left(2\mu_c\frac{dy_1}{dr}\right)-\frac{\ell(\ell+1)}{r}y_4+\frac{2\mu_c}{r}\left(2\frac{dy_1}{dr}-\frac{2}{r}y_1+\frac{\ell(\ell+1)}{r}y_3\right)\right]Y_\ell\\ &+r\left(\frac{dy_4}{dr}+\frac{3}{r}y_4+\frac{2\mu_c}{r^2}\left[y_1+\left(1-\ell-\ell^2\right)y_3\right]\right)\frac{\partial Y_\ell}{\partial x_i}.\end{aligned}\tag{B34}$$

Equations B29, B30, and B34 lead to

$$\begin{aligned}\frac{\partial\widetilde{\sigma}_{ij}}{\partial x_j} &= \frac{x_i}{r}\left[\frac{dy_2}{dr}-\frac{\ell(\ell+1)}{r}y_4+\frac{2\mu_c}{r}\left(2\frac{dy_1}{dr}-\frac{2}{r}y_1+\frac{\ell(\ell+1)}{r}y_3\right)\right]Y_\ell\\ &+r\left(\frac{1}{r}y_2-\frac{2\mu_c}{r}\frac{dy_1}{dr}+\frac{dy_4}{dr}+\frac{3}{r}y_4+\frac{2\mu_c}{r^2}\left[y_1+\left(1-\ell-\ell^2\right)y_3\right]\right)\frac{\partial Y_\ell}{\partial x_i}.\end{aligned}\tag{B35}$$

Appendix C: Differential Equation System of y Functions Under Some Limiting Conditions

C1. Slow Deformation

For a slow but not static deformation, the inertial effects may be ignored. This is the limit of $\omega^2 \to 0$ (but not $\omega \to 0$). In this case, the differential equation system becomes

$$\begin{aligned}\frac{dy_2}{dr} &= \left(-\frac{4\rho g}{r}+\frac{12K_d\mu_c}{(\lambda_c+2\mu_c)r^2}+i\frac{\ell(\ell+1)k\rho_f^2g^2}{\omega\eta_f r^2}\right)y_1-\frac{4\mu_c}{(\lambda_c+2\mu_c)r}y_2\\ &+\frac{\ell(\ell+1)}{r}\left(\rho g-\frac{6K_d\mu_c}{(\lambda_c+2\mu_c)r}\right)y_3+\frac{\ell(\ell+1)}{r}y_4+\frac{\ell+1}{r}\left(\rho-i\frac{\ell k\rho_f^2 g}{\omega\eta_f r}\right)y_5-\rho y_6\\ &+\left(-4\phi+i\frac{\ell(\ell+1)k\rho_f g}{\omega\eta_f r}\right)\frac{\rho_f g}{r}y_8+\left(-\frac{4\alpha\mu_c}{(\lambda_c+2\mu_c)r}+i\frac{\ell(\ell+1)k\rho_f g}{\omega\eta_f r^2}\right)y_9,\end{aligned}\tag{C1}$$

$$\begin{aligned}\frac{dy_4}{dr} &= \left(\frac{\rho g}{r}-\frac{6K_d\mu_c}{(\lambda_c+2\mu_c)r^2}\right)y_1-\frac{\lambda_c}{(\lambda_c+2\mu_c)r}y_2+\frac{2\mu_c}{r^2}\left(\frac{2\ell(\ell+1)(\lambda_c+\mu_c)}{\lambda_c+2\mu_c}-1\right)y_3\\ &-\frac{3}{r}y_4-\frac{\rho}{r}y_5+\frac{\phi\rho_f g}{r}y_8+\frac{2\alpha\mu_c}{(\lambda_c+2\mu_c)r}y_9\end{aligned}\tag{C2}$$

$$\begin{aligned}\frac{dy_6}{dr} &= \frac{4\pi(\ell+1)G}{r}\left(\rho-i\frac{\ell k\rho_f^2 g}{\omega\eta_f r}\right)y_1-\frac{4\pi\ell(\ell+1)G\rho}{r}y_3+i\frac{4\pi\ell(\ell+1)Gk\rho_f^2}{\omega\eta_f r^2}y_5+\frac{\ell-1}{r}y_6\\ &+\frac{4\pi(\ell+1)G\rho_f}{r}\left(\phi-i\frac{\ell k\rho_f g}{\omega\eta_f r}\right)y_8-i\frac{4\pi\ell(\ell+1)Gk\rho_f}{\omega\eta_f r^2}y_9,\end{aligned}\tag{C3}$$

$$\begin{aligned}\frac{dy_8}{dr} &= \frac{1}{\phi r}\left(-\frac{4\alpha\mu_c}{\lambda_c+2\mu_c}+i\frac{\ell(\ell+1)k\rho_f g}{\omega\eta_f r}\right)y_1-\frac{\alpha}{\phi(\lambda_c+2\mu_c)}y_2+\frac{2\ell(\ell+1)\alpha\mu_c}{\phi(\lambda_c+2\mu_c)r}y_3-i\frac{\ell(\ell+1)k\rho_f}{\omega\phi\eta_f r^2}y_5\\ &+\left(-\frac{2}{r}+i\frac{\ell(\ell+1)k\rho_f g}{\omega\phi\eta_f r^2}\right)y_8-\frac{1}{\phi}\left(\frac{1}{M}+\frac{\alpha^2}{\lambda_c+2\mu_c}-i\frac{\ell(\ell+1)k}{\omega\eta_f r^2}\right)y_9,\end{aligned}\tag{C4}$$

$$\begin{aligned}\frac{dy_9}{dr} &= \left(4-i\frac{\ell(\ell+1)k\rho_f g}{\omega\phi\eta_f r}\right)\frac{\rho_f g}{r}y_1-\frac{\ell(\ell+1)\rho_f g}{r}y_3-\frac{(\ell+1)\rho_f}{r}\left(1-i\frac{\ell k\rho_f g}{\omega\phi\eta_f r}\right)y_5+\rho_f y_6\\ &+\left[-i\frac{\omega\phi\eta_f}{k}+\left(4-i\frac{\ell(\ell+1)k\rho_f g}{\omega\phi\eta_f r}+r\frac{d\phi}{dr}\right)\frac{\rho_f g}{r}-4\pi G\rho_f(\rho-\phi\rho_f)\right]y_8-i\frac{\ell(\ell+1)k\rho_f g}{\omega\phi\eta_f r^2}y_9.\end{aligned}\tag{C5}$$

The equations for dy_1/dr, dy_3/dr, and dy_5/dr remain the same. y_{10} is given by

$$y_{10} = i\frac{k}{\omega\phi\eta_f r}(\rho_f g y_1 - \rho_f y_5 + \rho_f g y_8 + y_9). \tag{C6}$$

Here, $F_f = 1$ is also assumed (see Appendix A).

C2. Nonporous Condition

It would be useful to confirm that the equation system for a nonporous material can be obtained under the limits of $\alpha \to 0$ and $\phi \to 0$. It can be easily shown that

$$\frac{dy_1}{dr} = -\frac{2\lambda_c}{(\lambda_c + 2\mu_c)r}y_1 + \frac{1}{\lambda_c + 2\mu_c}y_2 + \frac{\ell(\ell+1)\lambda_c}{(\lambda_c + 2\mu_c)r}y_3, \tag{C7}$$

$$\frac{dy_2}{dr} = \left(-\omega^2\rho - \frac{4\rho g}{r} + \frac{12K_d\mu_c}{(\lambda_c + 2\mu_c)r^2}\right)y_1 - \frac{4\mu_c}{(\lambda_c + 2\mu_c)r}y_2 + \frac{\ell(\ell+1)}{r}\left(\rho g - \frac{6K_d\mu_c}{(\lambda_c + 2\mu_c)r}\right)y_3 + \frac{\ell(\ell+1)}{r}y_4 + \frac{(\ell+1)\rho}{r}y_5 - \rho y_6, \tag{C8}$$

$$\frac{dy_3}{dr} = -\frac{1}{r}y_1 + \frac{1}{r}y_3 + \frac{1}{\mu_c}y_4, \tag{C9}$$

$$\frac{dy_4}{dr} = \left(\frac{\rho g}{r} - \frac{6K_d\mu_c}{(\lambda_c + 2\mu_c)r^2}\right)y_1 - \frac{\lambda_c}{(\lambda_c + 2\mu_c)r}y_2 + \left[-\omega^2\rho + \frac{2\mu_c}{r^2}\left(\frac{2\ell(\ell+1)(\lambda_c + \mu_c)}{\lambda_c + 2\mu_c} - 1\right)\right]y_3 - \frac{3}{r}y_4 - \frac{\rho}{r}y_5 \tag{C10}$$

$$\frac{dy_5}{dr} = 4\pi G\rho y_1 - \frac{\ell+1}{r}y_5 + y_6, \tag{C11}$$

$$\frac{dy_6}{dr} = \frac{4\pi(\ell+1)G\rho}{r}y_1 - \frac{4\pi\ell(\ell+1)G\rho}{r}y_3 + \frac{\ell-1}{r}y_6, \tag{C12}$$

can be obtained under these limits. As expected, these equations are exactly the same as those obtained by Takeuchi and Saito (1972) for a nonporous material.

C3. Inviscid Fluid Layer

The differential equation system of y functions for an inviscid fluid layer is given by Kamata et al. (2015) and Takeuchi and Saito (1972).

$$\frac{dy_1}{dr} = \left(-\frac{2}{r} + \frac{\ell(\ell+1)g}{\omega^2 r^2}\right)y_1 + \left(\frac{1}{\lambda} - \frac{\ell(\ell+1)}{\omega^2\rho r^2}\right)y_2 - \frac{\ell(\ell+1)}{\omega^2 r^2}y_5, \tag{C13}$$

$$\frac{dy_2}{dr} = \left(-\omega^2\rho - \frac{4\rho g}{r} + \frac{\ell(\ell+1)\rho g^2}{\omega^2 r^2}\right)y_1 - \frac{\ell(\ell+1)g}{\omega^2 r^2}y_2 + \frac{(\ell+1)\rho}{r}\left(1 - \frac{\ell g}{\omega^2 r}\right)y_5 - \rho y_6, \tag{C14}$$

$$\frac{dy_5}{dr} = 4\pi G\rho y_1 - \frac{\ell+1}{r}y_5 + y_6, \tag{C15}$$

$$\frac{dy_6}{dr} = \frac{4\pi(\ell+1)G\rho}{r}\left(1 - \frac{\ell g}{\omega^2 r}\right)y_1 + \frac{4\pi\ell(\ell+1)G}{\omega^2 r^2}y_2 + \frac{4\pi\ell(\ell+1)G\rho}{\omega^2 r^2}y_5 + \frac{\ell-1}{r}y_6. \tag{C16}$$

Here, y_3 and y_4 are not obtained by the differential equations but are given by

$$y_3 = \frac{1}{\omega^2\rho r}(\rho g y_1 - y_2 - \rho y_5), \tag{C17}$$

$$y_4 = 0. \tag{C18}$$

The above equations are not obtained simply by considering the limits of $\alpha \to 1$ and $\phi \to 1$ because the pore fluid is assumed to be a viscous fluid. Instead, it can be obtained by taking the limit of $\mu_c \to 0$ for the equation system for a nonporous case given in Appendix C2.

If a static deformation (i.e., $\omega = 0$) is considered, the above equation system cannot be used because it contains terms with $1/\omega^2$. Even if $\omega \neq 0$, the equation system becomes numerically unstable under a small ω and a large liquid-layer thickness. For such cases, one can use the two-component equation system given by Saito (1974).

$$\frac{dy_5}{dr} = \left(\frac{4\pi G\rho}{g} - \frac{\ell+1}{r}\right) y_5 + y_7, \tag{C19}$$

$$\frac{dy_7}{dr} = \frac{2(\ell-1)}{r}\frac{4\pi G\rho}{g} y_5 + \left(\frac{\ell-1}{r} - \frac{4\pi G\rho}{g}\right) y_7, \tag{C20}$$

where

$$y_7 = \frac{4\pi G}{g} y_2 + y_6. \tag{C21}$$

Appendix D: Static Deformation

As mentioned in Section 2.2, static deformation can be calculated using a six-component equation system given in Appendix C2 or a two-component equation system given in Appendix C3 depending on the behavior of the solid frame at $\omega = 0$. Below, we directly substitute $\omega = 0$ into Equation 49 (i.e., the equation of motion for fluid) to show that the equation system degenerates; one cannot use an eight-component system.

Substitution of $\omega = 0$ into Equation B16 yields

$$\begin{aligned} 0 = \frac{x_i}{r}\Bigg[&\frac{2\rho_f g}{r} y_1 - \frac{\ell(\ell+1)\rho_f g}{r} y_3 + \left(\frac{2\rho_f g}{r} + \rho_f g\frac{d\phi}{dr}\right) y_8 - \frac{\ell(\ell+1)\rho_f g}{r} y_{10} - \frac{dy_9}{dr} \\ &-\rho_f \frac{d}{dr}[g(y_8+y_1)] + \rho_f\left(g\frac{dy_1}{dr} + \frac{dy_5}{dr} + g\frac{dy_8}{dr}\right)\Bigg] Y_\ell^m - (\rho_f g y_1 - \rho_f y_5 + \rho_f g y_8 + y_9)\frac{\partial Y_\ell^m}{\partial x_i}. \end{aligned} \tag{D1}$$

The term proportional to $\partial Y_\ell / \partial x_i$ leads to

$$y_9 = -\rho_f g y_1 + \rho_f y_5 - \rho_f g y_8. \tag{D2}$$

Using Equation D2, the term proportional to Y_ℓ leads to

$$\begin{aligned} 0 = &\frac{4(\phi-\alpha)\rho_f g\mu_c}{(\lambda_c+2\mu_c)r} y_1 + \frac{(\phi-\alpha)\rho_f g}{\lambda_c+2\mu_c} y_2 - \frac{2\ell(\ell+1)(\phi-\alpha)\rho_f g\mu_c}{(\lambda_c+2\mu_c)r} y_3 \\ &+\phi\rho_f g\frac{d\phi}{dr} y_8 - \left(\frac{\rho_f g}{M} - \frac{(\phi-\alpha)\alpha\rho_f g}{\lambda_c+2\mu_c} + \frac{\phi}{\rho_f}\frac{d\rho_f}{dr}\right) y_9. \end{aligned} \tag{D3}$$

Using Equations D2 and D3, y_8 and y_9 (and thus y_{10} from Equation B4) can be obtained from other y functions. Consequently, one can construct a differential equation system free of y_8 and y_9; the number of ordinary differential equations becomes six.

The fact that y_8 and y_9 are calculated uniquely from y_1–y_6 indicates that the boundary condition given in Section 2.4 does not necessarily meet. For example, consider a porous layer that has a free surface. In this case, y_9 should be zero at the surface, although y_9 calculated from other y functions may not equal zero.

This apparent inconsistency under the static condition would be the result of a shear-stress-free condition for the pore fluid. As mentioned in Section 2.1, we consider the macroscopic motion of the pore fluid, and in this case, one can use a shear-free stress tensor for the pore fluid (e.g., Neuman, 1977; Whitaker, 1986). It is known that the use of a shear-stress-free constitutive equation leads to the system being overdetermined and causing an apparent contradiction; for example, the solution yields an unrealistic cavitation at the core-mantle boundary (e.g., Dahlen & Fels, 1978; Longman, 1963; Saito, 1974; Smylie & Mansinha, 1971). A reasonable way to avoid such a contradiction is to reduce the number of y functions to be determined and to leave some y functions undetermined (see

Appendix C3 and Saito (1974)). However, introducing a new set of y functions for the static case is beyond the scope of this study and is left for another study.

Finally, the homogeneous solution under the static condition is summarized below. As expected from the fact that the number of ordinary differential equations is six, the number of linearly independent solutions is three for the homogeneous sphere. Substitution of $\omega = 0$ into Equation 74 yields

$$X^{\mathrm{rel}} = -X^s. \tag{D4}$$

Consequently, Equations 72, 73, and 75 become

$$\mu_c \nabla^2 Z^s = (\rho - \phi\rho_f)\gamma X^s, \tag{D5}$$

$$\left[(\lambda_c + 2\mu_c + \alpha(\alpha - \phi)M)\nabla^2 + 4(\rho - \phi\rho_f)\gamma\right] X^s = \ell(\ell+1)\gamma\left(\rho Z^s + \phi\rho_f Z^{\mathrm{rel}}\right), \tag{D6}$$

$$\left[(\alpha - \phi)M\nabla^2 + 3\left(1 - \frac{\phi\rho_f}{\rho}\right)\rho_f\gamma\right] X^s = \ell(\ell+1)\rho_f\gamma\left(Z^s + Z^{\mathrm{rel}}\right). \tag{D7}$$

Equation D7 yields

$$Z^{\mathrm{rel}} = \frac{1}{\ell(\ell+1)}\left[\frac{(\alpha - \phi)M}{\rho_f\gamma}\nabla^2 + 3\left(1 - \frac{\phi\rho_f}{\rho}\right)\right] X^s - Z^s. \tag{D8}$$

Then, one can obtain

$$\nabla^2\begin{pmatrix} X^s \\ Z^s \end{pmatrix} = A''\begin{pmatrix} X^s \\ Z^s \end{pmatrix} = \begin{pmatrix} a''_{11} & a''_{12} \\ a''_{21} & a''_{22} \end{pmatrix}\begin{pmatrix} X^s \\ Z^s \end{pmatrix}, \tag{D9}$$

where

$$a''_{11} = -\frac{\left(1 - \frac{\phi\rho_f}{\rho}\right)(4\rho - 3\phi\rho_f)\gamma}{\lambda_c + 2\mu_c + (\alpha - \phi)^2 M}, \tag{D10}$$

$$a''_{12} = \frac{\ell(\ell+1)(\rho - \phi\rho_f)\gamma}{\lambda_c + 2\mu_c + (\alpha - \phi)^2 M}, \tag{D11}$$

$$a''_{21} = \frac{(\rho - \phi\rho_f)\gamma}{\mu_c}, \tag{D12}$$

$$a''_{22} = 0. \tag{D13}$$

Equation D9 yields

$$X^s = c_1 p''_{11} j_\ell\left(k_1^{e''} r\right) + c_2 p''_{12} j_\ell\left(k_2^{e''} r\right), \tag{D14}$$

$$Z^s = c_1 p''_{21} j_\ell\left(k_1^{e''} r\right) + c_2 p''_{22} j_\ell\left(k_2^{e''} r\right), \tag{D15}$$

where c_i $(i = 1, 2)$ are constants to be determined by the boundary condition at the surface, $-\left(k_i^{e''}\right)^2$ $(i = 1, 2)$ are the eigenvalues of the matrix A'', and p''_{ij} is the jth component of the corresponding eigenvector, respectively. Equations D4, D8, D14, and D15 yield

$$X^{\mathrm{rel}} = c_1 p''_{31} j_\ell\left(k_1^{e''} r\right) + c_2 p''_{32} j_\ell\left(k_2^{e''} r\right), \tag{D16}$$

$$Z^{\mathrm{rel}} = c_1 p''_{41} j_\ell\left(k_1^{e''} r\right) + c_2 p''_{42} j_\ell\left(k_2^{e''} r\right), \tag{D17}$$

where

$$p''_{3i} = -p''_{1i}, \tag{D18}$$

$$p''_{4i} = \frac{1}{\ell(\ell+1)}\left[-\frac{(\alpha-\phi)M\left(k_i^{e\prime\prime}\right)^2}{\rho_f\gamma} + 3\left(1-\frac{\phi\rho_f}{\rho}\right)\right]p''_{1i} - p''_{2i}. \tag{D19}$$

Then, two sets of solutions for the y functions can be obtained from Equations 93–101 replacing k_i^e and p_{ij} with $k_i^{e\prime\prime}$ and p''_{ij}, respectively. The third solution is given by Equations 105–113.

Appendix E: Solution for a Homogeneous Nonporous Solid Sphere

E1. Compressible Case

In this case, X^{rel} does not appear, and the matrix A in Equation 77 becomes a 2×2 matrix. More specifically,

$$\nabla^2\begin{pmatrix}X^s\\Z^s\end{pmatrix} = A\begin{pmatrix}X^s\\Z^s\end{pmatrix} = \begin{pmatrix}a_{11} & a_{12}\\ a_{21} & a_{22}\end{pmatrix}\begin{pmatrix}X^s\\Z^s\end{pmatrix}, \tag{E1}$$

where

$$a_{11} = -\frac{\left(\omega^2+4\gamma\right)\rho}{\lambda_c+2\mu_c}, \tag{E2}$$

$$a_{12} = \frac{\ell(\ell+1)\rho\gamma}{\lambda_c+2\mu_c}, \tag{E3}$$

$$a_{21} = \frac{\rho\gamma}{\mu_c}, \tag{E4}$$

$$a_{22} = -\frac{\omega^2\rho}{\mu_c}. \tag{E5}$$

The eigenvalues $-\left(k_i^e\right)^2$ $(i=1,2)$ of A are then given by

$$\begin{aligned}-\left(k_i^e\right)^2 &= \frac{1}{2}\left(a_{11}+a_{22}\pm\sqrt{(a_{22}-a_{11})^2+4a_{12}a_{21}}\right)\\ &= -\frac{\rho}{2}\left(\frac{\omega^2+4\gamma}{\lambda_c+2\mu_c}+\frac{\omega^2}{\mu_c}\mp\sqrt{\left(\frac{\omega^2}{\mu_c}-\frac{\omega^2+4\gamma}{\lambda_c+2\mu_c}\right)^2+\frac{4\ell(\ell+1)\gamma^2}{(\lambda_c+2\mu_c)\mu_c}}\right),\end{aligned} \tag{E6}$$

and the eigenvectors p_{ji} satisfy

$$\frac{p_{1i}}{p_{2i}} = \frac{1}{\gamma}\left(\omega^2-\frac{\mu}{\rho}\left(k_i^e\right)^2\right). \tag{E7}$$

Then, Equations 98 and 99 of Takeuchi and Saito (1972) can be obtained by substituting $p_{2i}=\left(k_i^e\right)^2$ and $\alpha = p_{3i} = p_{4i} = 0$ into Equations 93–98. The third solution is the trivial solution given by Equations 105–110.

E2. Incompressible Case

In this case, $\lambda_c\to\infty$, $X^s\to 0$, while $\lambda_c X^s$ approaches a finite value. Thus, Equations 72 and 73 can be written as

$$\nabla^2\begin{pmatrix}Z^s\\ \lambda_c X^s\end{pmatrix} = \begin{pmatrix}-\frac{\omega^2\rho}{\mu_c} & 0\\ \ell(\ell+1)\rho\gamma & 0\end{pmatrix}\begin{pmatrix}Z^s\\ \lambda_c X^s\end{pmatrix}. \tag{E8}$$

The eigenvalues of the matrix on the right-hand side of this equation are given by $-\left(k_1^{e\prime}\right)^2 = -\omega^2\rho/\mu_c$ and $-\left(k_2^{e\prime}\right)^2 = 0$. The first solution for a nonzero eigenvalue is given by

$$y_1 = -\frac{\ell(\ell+1)}{r}j_\ell\left(k_1^{e\prime}r\right), \tag{E9}$$

$$y_2 = -\ell(\ell+1)\left[\left(\rho\gamma + \frac{2(\ell-1)\mu_c}{r^2}\right) j_\ell\left(k_1^{e\prime} r\right) - \frac{2k_1^{e\prime}\mu_c}{r} j_{\ell+1}\left(k_1^{e\prime} r\right)\right], \tag{E10}$$

$$y_3 = -\frac{\ell+1}{r} j_\ell\left(k_1^{e\prime} r\right) + k_1^{e\prime} j_{\ell+1}\left(k_1^{e\prime} r\right), \tag{E11}$$

$$y_4 = \mu_c\left[\left(\left(k_1^{e\prime}\right)^2 - \frac{2\left(\ell^2-1\right)}{r^2}\right) j_\ell\left(k_1^{e\prime} r\right) - \frac{2k_1^{e\prime}}{r} j_{\ell+1}\left(k_1^{e\prime} r\right)\right], \tag{E12}$$

$$y_5 = 0, \tag{E13}$$

$$y_6 = \frac{3\ell(\ell+1)\gamma}{r} j_\ell\left(k_1^{e\prime} r\right), \tag{E14}$$

which can be obtained by substituting $\lambda_c p_{11} = -\ell(\ell+1)\rho\gamma$, $p_{21} = \left(k_1^{e\prime}\right)^2 = \omega^2\rho/\mu_c$, and $\alpha = p_{11} = p_{31} = p_{41} = 0$ into Equations 93–98. The second solution is given by

$$y_1 = 0, \tag{E15}$$

$$y_2 = -\rho r^\ell, \tag{E16}$$

$$y_3 = 0, \tag{E17}$$

$$y_4 = 0, \tag{E18}$$

$$y_5 = r^\ell, \tag{E19}$$

$$y_6 = \frac{2\ell+1}{r} y_5 - 3\gamma y_1 \;=\; (2\ell+1) r^{\ell-1}. \tag{E20}$$

The third solution is the trivial solution for a compressible case given by Equations 105–110.

Appendix F: Stress and Strain Variables Using *y* Functions

Below are some fundamental variables of stress and strain expressed using y functions:

$$\widetilde{u}_r^s = \frac{x_i \widetilde{u}_i^s}{r} = \sum_{\ell,m} U_{\ell m} y_1(\ell, r) Y_\ell^m = \sum_\ell \left(y_1(\ell, r) \sum_m U_{\ell m} Y_\ell^m \right), \tag{F1}$$

$$\widetilde{u}_\theta^s = \frac{1}{r}\left(\frac{z\left(x\widetilde{u}_x^s + y\widetilde{u}_y^s\right)}{\sqrt{x^2+y^2}} - \sqrt{x^2+y^2}\widetilde{u}_z^s \right) = \sum_{\ell,m} U_{\ell m} y_3(\ell, r) \frac{\partial Y_\ell^m}{\partial\theta} = \sum_\ell \left(y_3(\ell, r) \sum_m U_{\ell m} \frac{\partial Y_\ell^m}{\partial\theta} \right), \tag{F2}$$

$$\widetilde{u}_\varphi^s = \frac{-y\left(x\widetilde{u}_x^s + x\widetilde{u}_y^s\right)}{\sqrt{x^2+y^2}} = \sum_{\ell,m} U_{\ell m} \frac{y_3(\ell, r)}{\sin\theta} \frac{\partial Y_\ell^m}{\partial\varphi} = \sum_\ell \left(\frac{y_3(\ell, r)}{\sin\theta} \sum_m U_{\ell m} \frac{\partial Y_\ell^m}{\partial\varphi} \right), \tag{F3}$$

$$\begin{aligned} \widetilde{e}_{rr}^s = \frac{\partial \widetilde{u}_r^s}{\partial r} &= \sum_{\ell,m} U_{\ell m} \frac{d y_1(\ell, r)}{d r} Y_\ell^m = \sum_\ell \left(\frac{d y_1(\ell, r)}{d r} \sum_m U_{\ell m} Y_\ell^m \right) \\ &= \sum_\ell \left(\frac{-2\lambda_c y_1 + r y_2 + \ell(\ell+1)\lambda_c y_3 + \alpha r y_9}{(\lambda_c + 2\mu_c) r} \sum_m U_{\ell m} Y_\ell^m \right), \end{aligned} \tag{F4}$$

$$\begin{aligned} \widetilde{e}_{\theta\theta}^s = \frac{1}{r}\left(\frac{\partial \tilde{u}_\theta}{\partial\theta} + \tilde{u}_r \right) &= \sum_{\ell,m} U_{\ell m} \left(\frac{y_1(\ell, r)}{r} Y_\ell^m + \frac{y_3(\ell, r)}{r} \frac{\partial^2 Y_\ell^m}{\partial\theta^2} \right) \\ &= \sum_\ell \left(\frac{y_1(\ell, r)}{r} \sum_m U_{\ell m} Y_\ell^m + \frac{y_3(\ell, r)}{r} \sum_m U_{\ell m} \frac{\partial^2 Y_\ell^m}{\partial\theta^2} \right), \end{aligned} \tag{F5}$$

$$\tilde{e}^{s}_{\varphi\varphi} = \frac{1}{r}\left(\frac{1}{\sin\theta}\frac{\partial \tilde{u}_\varphi}{\partial \varphi} + \cot\theta \tilde{u}_\theta + \tilde{u}_r\right) = \sum_{\ell,m} U_{\ell m}\left[\frac{y_1(\ell,r)}{r}Y^m_\ell + \frac{y_3(\ell,r)}{r}\left(\frac{\cos\theta}{\sin\theta}\frac{\partial Y^m_\ell}{\partial\theta} + \frac{1}{\sin^2\theta}\frac{\partial^2 Y^m_\ell}{\partial\varphi^2}\right)\right]$$
$$= \sum_{\ell}\left[\frac{y_1(\ell,r)}{r}\sum_m U_{\ell m}Y^m_\ell + \frac{y_3(\ell,r)}{r}\sum_m U_{\ell m}\left(\frac{\cos\theta}{\sin\theta}\frac{\partial Y^m_\ell}{\partial\theta} + \frac{1}{\sin^2\theta}\frac{\partial^2 Y^m_\ell}{\partial\varphi^2}\right)\right], \tag{F6}$$

$$\tilde{e}^{s}_{r\theta} = \frac{1}{2}\left(\frac{\partial \tilde{u}^s_\theta}{\partial r} - \frac{1}{r}\tilde{u}^s_\theta + \frac{1}{r}\frac{\partial \tilde{u}^s_r}{\partial\theta}\right) = \sum_{\ell,m} U_{\ell m}\frac{y_4(\ell,r)}{2\mu_c}\frac{\partial Y^m_\ell}{\partial\theta} = \sum_\ell\left(\frac{y_4(\ell,r)}{2\mu_c}\sum_m U_{\ell m}\frac{\partial Y^m_\ell}{\partial\theta}\right), \tag{F7}$$

$$\tilde{e}^{s}_{r\varphi} = \frac{1}{2}\left(\frac{1}{r\sin\theta}\frac{\partial \tilde{u}_r}{\partial\varphi} + \frac{\partial \tilde{u}_\varphi}{\partial r} - \frac{1}{r}\tilde{u}_\varphi\right) = \sum_{\ell,m} U_{\ell m}\frac{y_4(\ell,r)}{2\mu_c\sin\theta}\frac{\partial Y^m_\ell}{\partial\varphi} = \sum_\ell\left(\frac{y_4(\ell,r)}{2\mu_c\sin\theta}\sum_m U_{\ell m}\frac{\partial Y^m_\ell}{\partial\varphi}\right), \tag{F8}$$

$$\tilde{e}^{s}_{\theta\varphi} = \frac{1}{2r}\left(\frac{\partial \tilde{u}_\varphi}{\partial\theta} - \cot\theta\tilde{u}_\varphi + \frac{1}{\sin\theta}\frac{\partial \tilde{u}_\theta}{\partial\varphi}\right) = \sum_{\ell,m} U_{\ell m}\frac{y_3(\ell,r)}{r}\left(\frac{1}{\sin\theta}\frac{\partial^2 Y^m_\ell}{\partial\theta\partial\varphi} - \frac{\cos\theta}{\sin^2\theta}\frac{\partial Y^m_\ell}{\partial\varphi}\right)$$
$$= \sum_\ell\left[\frac{y_3(\ell,r)}{r}\sum_m U_{\ell m}\left(\frac{1}{\sin\theta}\frac{\partial^2 Y^m_\ell}{\partial\theta\partial\varphi} - \frac{\cos\theta}{\sin^2\theta}\frac{\partial Y^m_\ell}{\partial\varphi}\right)\right], \tag{F9}$$

$$\tilde{e}^{s}_{kk} = \frac{\partial \tilde{u}^s_i}{\partial x_i} = \sum_{\ell,m} U_{\ell m}\left(\frac{dy_1(\ell,r)}{dr} + \frac{2y_1(\ell,r)}{r} - \frac{\ell(\ell+1)y_3(\ell,r)}{r}\right)Y^m_\ell$$
$$= \sum_\ell\left(\frac{4\mu_c y_1 + r y_2 - 2\ell(\ell+1)\mu_c y_3 + \alpha r y_9}{(\lambda_c+2\mu_c)r}\sum_m U_{\ell m}Y^m_\ell\right), \tag{F10}$$

$$\tilde{u}^{\mathrm{rel}}_r = \frac{x_i\tilde{u}^{\mathrm{rel}}_i}{r} = \sum_{\ell,m} U_{\ell m}y_8(\ell,r)Y^m_\ell = \sum_\ell\left(y_8(\ell,r)\sum_m U_{\ell m}Y^m_\ell\right), \tag{F11}$$

$$\tilde{u}^{\mathrm{rel}}_\theta = \frac{1}{r}\left(\frac{z\left(x\tilde{u}^{\mathrm{rel}}_x + y\tilde{u}^{\mathrm{rel}}_y\right)}{\sqrt{x^2+y^2}} - \sqrt{x^2+y^2}\tilde{u}^{\mathrm{rel}}_z\right) = \sum_{\ell,m} U_{\ell m}y_{10}(\ell,r)\frac{\partial Y^m_\ell}{\partial\theta} = \sum_\ell\left(y_{10}(\ell,r)\sum_m U_{\ell m}\frac{\partial Y^m_\ell}{\partial\theta}\right), \tag{F12}$$

$$\tilde{u}^{\mathrm{rel}}_\varphi = \frac{-y\left(x\tilde{u}^{\mathrm{rel}}_x + x\tilde{u}^{\mathrm{rel}}_y\right)}{\sqrt{x^2+y^2}} = \sum_{\ell,m} U_{\ell m}\frac{y_{10}(\ell,r)}{\sin\theta}\frac{\partial Y^m_\ell}{\partial\varphi} = \sum_\ell\left(\frac{y_{10}(\ell,r)}{\sin\theta}\sum_m U_{\ell m}\frac{\partial Y^m_\ell}{\partial\varphi}\right), \tag{F13}$$

$$\tilde{e}^{\mathrm{rel}}_{kk} = \frac{\partial \tilde{u}^{\mathrm{rel}}_i}{\partial x_i} = \sum_{\ell,m} U_{\ell m}\left(\frac{dy_8(\ell,r)}{dr} + \frac{2y_8(\ell,r)}{r} - \frac{\ell(\ell+1)y_{10}(\ell,r)}{r}\right)Y^m_\ell$$
$$= -\sum_\ell\left[\frac{\alpha}{\phi}\left(\frac{4\mu_c y_1 + r y_2 - 2\ell(\ell+1)\mu_c y_3 + \alpha r y_9}{(\lambda_c+2\mu_c)r} + \frac{y_9}{\alpha M}\right)\sum_m U_{\ell m}Y^m_\ell\right], \tag{F14}$$

$$\tilde{\sigma}_{rr} = \frac{x_i\tilde{\sigma}_{ri}}{r} = \sum_{\ell,m} U_{\ell m}y_2(\ell,r)Y^m_\ell = \sum_\ell\left(y_2(\ell,r)\sum_m U_{\ell m}Y^m_\ell\right), \tag{F15}$$

$$\tilde{\sigma}_{r\theta} = \frac{1}{r}\left(\frac{z\left(x\tilde{\sigma}_{rx} + y\tilde{\sigma}_{ry}\right)}{\sqrt{x^2+y^2}} - \sqrt{x^2+y^2}\tilde{\sigma}_{rz}\right) = \sum_{\ell,m} U_{\ell m}y_4(\ell,r)\frac{\partial Y^m_\ell}{\partial\theta} = \sum_\ell\left(y_4(\ell,r)\sum_m U_{\ell m}\frac{\partial Y^m_\ell}{\partial\theta}\right). \tag{F16}$$

Here, no summation is applied for the left hand sides of Equations F4–F6 and F15.

Appendix G: Spherical Harmonic Expansion of the Tidal Potential

The tidal potential U can be written as (e.g., Beuthe, 2013; Matsuyama et al., 2018)

$$U(t,r,\theta,\varphi) = \mathrm{Re}\left[\sum_{\ell,m,\xi} U^\xi_{\ell m}(r)P^m_\ell(\cos\theta)e^{i(m\varphi-\omega_\xi t)}\right], \tag{G1}$$

where θ is the colatitude, φ is the latitude, ℓ is the spherical harmonic degree, m is the spherical harmonic order, $U^{\xi}_{\ell m}$ is the coefficient describing the amplitude of the forcing traveling in the ξ-direction, P^m_ℓ is the associated Legendre function, and ω_ξ is the frequency. The direction $\xi = E$ denotes eastward, while $\xi = W$ denotes westward. In this notation, positive and negative frequencies indicate eastward and westward components, respectively (i.e., $\omega_E = |\omega|$ and $\omega_W = -|\omega|$, where ω is the tidal frequency) (Matsuyama et al., 2018). The degree-two coefficients for eccentricity tides are given by

$$U^E_{2,0} = -\frac{3}{2}\omega^2 r^2 e, \tag{G2}$$

$$U^E_{2,2} = \frac{7}{8}\omega^2 r^2 e, \tag{G3}$$

$$U^W_{2,2} = -\frac{1}{8}\omega^2 r^2 e, \tag{G4}$$

and those for obliquity tides are given by

$$U^E_{2,1} = U^W_{2,1} = -\frac{1}{2}\omega^2 r^2 \sin\theta_o, \tag{G5}$$

where e is the eccentricity and θ_o is the obliquity. The other degree-two coefficients are zero. In contrast to Matsuyama et al. (2018), the minus signs appear on the coefficients for obliquity tides because this study uses P^m_ℓ containing the Condon-Shortley phase factor (i.e., $(-1)^m$).

Appendix H: Approximation of the Spherical Bessel Function of the First Kind for a Large Complex Argument

An asymptotic expansion of the Bessel function of the first kind for large values of $|z|$ is given by Watson (1966).

$$J_\ell(z) \approx \sqrt{\frac{2}{\pi z}}\left[\cos\left(z - \frac{\ell\pi}{2} - \frac{\pi}{4}\right)\sum_{m=0}^{\infty}\frac{(-1)^m f(\ell, 2m)}{(2z)^{2m}} - \sin\left(z - \frac{\ell\pi}{2} - \frac{\pi}{4}\right)\sum_{m=0}^{\infty}\frac{(-1)^m f(\ell, 2m+1)}{(2z)^{2m+1}}\right], \tag{H1}$$

where J_ℓ is the Bessel function of the first kind of the order of ℓ, z is a complex number, and

$$f(\ell, m) = \frac{1}{2^{2m} m!}\prod_{n=1}^{m}\left(4\ell^2 - (2n-1)^2\right). \tag{H2}$$

It can be shown that

$$\sum_{m=0}^{\infty}\frac{(-1)^m f(\ell, 2m)}{(2z)^{2m}} = 1 + \mathcal{O}\left(|z|^{-2}\right), \tag{H3}$$

$$\sum_{m=0}^{\infty}\frac{(-1)^m f(\ell, 2m+1)}{(2z)^{2m+1}} = \frac{4\ell^2 - 1}{8z} + \mathcal{O}\left(|z|^{-3}\right), \tag{H4}$$

$$\begin{aligned}\cos(\mathrm{Re}(z) + i\ \mathrm{Im}(z)) &= \frac{1}{2}\left(e^{i(\mathrm{Re}(z)+i\mathrm{Im}(z))} + e^{-i(\mathrm{Re}(z)+i\mathrm{Im}(z))}\right)\\ &= \frac{1}{2}\left(e^{-\mathrm{Im}(z)}e^{i\mathrm{Re}(z)} + e^{\mathrm{Im}(z)}e^{-i\mathrm{Re}(z)}\right),\end{aligned} \tag{H5}$$

$$\begin{aligned}\sin(\mathrm{Re}(z) + i\ \mathrm{Im}(z)) &= \frac{1}{2i}\left(e^{i(\mathrm{Re}(z)+i\mathrm{Im}(z))} - e^{-i(\mathrm{Re}(z)+i\mathrm{Im}(z))}\right)\\ &= \frac{1}{2i}\left(e^{-\mathrm{Im}(z)}e^{i\mathrm{Re}(z)} - e^{\mathrm{Im}(z)}e^{-i\mathrm{Re}(z)}\right).\end{aligned} \tag{H6}$$

Substitution of Equations H3–H6 into Equation H1 yields

$$\begin{aligned}J_\ell(z) &\approx \frac{e^{-\mathrm{Im}(z)}}{\sqrt{2\pi z}}\left[e^{i(\mathrm{Re}(z)-\ell\pi/2-\pi/4)} + \mathcal{O}\left(|z|^{-1}\right)\right] + \frac{e^{\mathrm{Im}(z)}}{\sqrt{2\pi z}}\left[e^{-i(\mathrm{Re}(z)-\ell\pi/2-\pi/4)} + \mathcal{O}\left(|z|^{-1}\right)\right]\\ &= \frac{e^{-\mathrm{Im}(z)}}{\sqrt{2\pi z}}\left[e^{i\mathrm{Re}(z)}i^{-\left(\ell+\frac{1}{2}\right)} + \mathcal{O}\left(|z|^{-1}\right)\right] + \frac{e^{\mathrm{Im}(z)}}{\sqrt{2\pi z}}\left[e^{-i\mathrm{Re}(z)}i^{\ell+\frac{1}{2}} + \mathcal{O}\left(|z|^{-1}\right)\right].\end{aligned} \tag{H7}$$

Thus, for the spherical Bessel function, one obtains

$$\begin{aligned} j_\ell(z) &= \sqrt{\frac{\pi}{2z}} J_{\ell+\frac{1}{2}}(z) \\ &\approx \frac{e^{-\mathrm{Im}(z)}}{2z}\left[i^{-(\ell+1)}e^{i\mathrm{Re}(z)} + \mathcal{O}\left(|z|^{-1}\right)\right] + \frac{e^{\mathrm{Im}(z)}}{2z}\left[i^{\ell+1}e^{-i\mathrm{Re}(z)} + \mathcal{O}\left(|z|^{-1}\right)\right], \end{aligned} \tag{H8}$$

which is equivalent to Equation 193.

Appendix I: Bulk Porosity for a Porosity Profile Exponentially Decreasing With Depth

The local density $\rho(r)$ is given by

$$\rho(r) = [1 - \phi(r)]\rho_s + \phi(r)\rho_f. \tag{I1}$$

Here, the solid and fluid densities, ρ_s and ρ_f, are fixed. Then, the total mass M of the core for a porosity profile given by Equation 200 is given by

$$\begin{aligned} M &= 4\pi \int_0^{R_c} \rho(r) r^2 dr \\ &= \frac{4\pi}{3}\rho_s R_c^3 - 4\pi\phi_{\max}(\rho_s - \rho_f)\int_0^{R_c} \exp(\lambda_\phi(r - R_c)) r^2 dr \\ &= \frac{4\pi}{3}\rho_s R_c^3 - 4\pi\phi_{\max}(\rho_s - \rho_f)\lambda_\phi^{-3} e^{-\lambda_\phi R_c}\int_0^{\lambda_\phi R_c} e^x x^2 dx \\ &= \frac{4\pi}{3}R_c^3\left\{\rho_s - 3\phi_{\min}(\rho_s - \rho_f)\left[\ln\left(\frac{\phi_{\max}}{\phi_{\min}}\right)\right]^{-3}\int_0^{\ln\left(\frac{\phi_{\max}}{\phi_{\min}}\right)} e^x x^2 dx\right\}. \end{aligned} \tag{I2}$$

Here,

$$\int_0^{x_0} e^x x^2 dx = \left[\left(x^2 + 2x + 2\right)e^x\right]_{x=0}^{x_0} = \left(x_0^2 + 2x_0 + 2\right)e^{x_0} - 2. \tag{I3}$$

Consequently,

$$M = \frac{4\pi}{3}R_c^3\left\{\rho_s - 3\phi_{\min}(\rho_s - \rho_f)\left[\ln\left(\frac{\phi_{\max}}{\phi_{\min}}\right)\right]^{-3}\left[\left(x^2 + 2x + 2\right)e^x\right]_{x=0}^{\ln\left(\phi_{\max}/\phi_{\min}\right)}\right\}. \tag{I4}$$

On the other hand, using the bulk porosity ϕ_{bulk}, the total mass M can be written as

$$\begin{aligned} M &= \frac{4\pi}{3}\{[1 - \phi_{\mathrm{bulk}}]\rho_s + \phi_{\mathrm{bulk}}\rho_f\}R_c^3 \\ &= \frac{4\pi}{3}\left[\rho_s - (\rho_s - \rho_f)\phi_{\mathrm{bulk}}\right]R_c^3. \end{aligned} \tag{I5}$$

Comparing Equations I4 and I5, one can obtain Equation 202.

Data Availability Statement

The numerical code developed and scripts used in this study can be obtained at Kamata (2023).

Acknowledgments
The author thanks Dr. Gabriel Tobie, Mr. Ryu Akiba, and an anonymous reviewer for careful reviews and constructive comments. The author also thanks Dr. Jun Kimura and Dr. Taichi Kawamura for fruitful discussions. No actual field data are used. This work was supported by JSPS KAKENHI Grants 17H06457 and 21K03637.

References

Allen, M. B. (2021). *The mathematics of fluid flow through porous media*. Wiley.

Alterman, Z., Jarosch, H., & Pekeris, C. L. (1959). Oscillations of the Earth. *Proceedings of the Royal Society of London A*, *252*, 80–95. https://doi.org/10.1098/rspa.1959.0138

Arfken, G. B., Weber, H. J., & Harris, F. E. (2013). Legendre functions. In G. B. Arfken, H. J. Weber, & F. E. Harris (Eds.), *Mathematical methods for physicists* (7th ed., pp. 715–772). Academic Press. https://doi.org/10.1016/B978-0-12-384654-9.00015-3

Auriault, J.-L. (2009). On the domain of validity of Brinkman´s equation. *Transport in Porous Media*, *79*(2), 215–223. https://doi.org/10.1007/s11242-008-9308-7

Beuthe, M. (2013). Spatial patterns of tidal heating. *Icarus*, *223*(1), 308–329. https://doi.org/10.1016/j.icarus.2012.11.020
Biot, M. A. (1941). General theory of three-dimensional consolidation. *Journal of Applied Physics*, *12*(2), 155–164. https://doi.org/10.1063/1.1712886
Biot, M. A. (1956a). Theory of propagation of elastic waves in a fluid-saturated porous solid. I. Low-frequency range. *Journal of the Acoustical Society of America*, *28*(2), 168–178. https://doi.org/10.1121/1.1908239
Biot, M. A. (1956b). Theory of propagation of elastic waves in a fluid-saturated porous solid. II. Higher frequency range. *Journal of the Acoustical Society of America*, *28*(2), 179–191. https://doi.org/10.1121/1.1908241
Biot, M. A., & Willis, D. G. (1957). The elastic coefficients of the theory of consolidation. *Journal of Applied Mechanics*, *24*(4), 594–601. https://doi.org/10.1115/1.4011606
Čadek, O., Tobie, G., Hoolst, T. V., Massé, M., Choblet, G., Lefèvre, A., et al. (2016). Enceladus's internal ocean and ice shell constrained from Cassini gravity, shape and libration data. *Geophysical Research Letters*, *43*(11), 5653–5660. https://doi.org/10.1002/2016GL068634
Cheng, A. H.-D. (2016). *Poroelasticity*. Springer. https://doi.org/10.1007/978-3-319-25202-5
Choblet, G., Tobie, G., Sotin, C., Běhounková, M., Čadek, O., Postberg, F., & Souček, O. (2017). Powering prolonged hydrothermal activity inside Enceladus. *Nature Astronomy*, *1*(12), 841–847. https://doi.org/10.1038/s41550-017-0289-8
Christensen, N. I. (2004). Serpentinites, peridotites, and seismology. *International Geology Review*, *46*(9), 795–816. https://doi.org/10.2747/0020-6814.46.9.795
Corapcioglu, M. Y., & Tuncay, K. (1996). Propagation of waves in porous media. In *Advances in porous media* (Vol. 3, pp. 361–440). Elsevier. https://doi.org/10.1016/S1873-975X(96)80007-2
Dahlen, F. A., & Fels, S. B. (1978). A physical explanation of the static core paradox. *Geophysical Journal International*, *55*(2), 317–331. https://doi.org/10.1111/j.1365-246X.1978.tb04274.x
Fjær, E., Holt, R. M., Horsrud, P., Raaen, A. M., & Risnes, R. (2008). *Petroleum related rock mechanics*. Elsevier.
Gleeson, T., & Ingebritsen, S. E. (2017). *Crustal permeability*. Wiley. https://doi.org/10.1002/9781119166573
Harada, Y., Goossens, S., Matsumoto, K., Yan, J., Ping, J., Noda, H., & Haruyama, J. (2014). Strong tidal heating in an ultralow-viscosity zone at the core-mantle boundary of the Moon. *Nature Geoscience*, *7*(8), 569–572. https://doi.org/10.1038/ngeo2211
Hashin, Z., & Shtrikman, S. (1963). A variational approach to the theory of the elastic behaviour of multiphase materials. *Journal of the Mechanics and Physics of Solids*, *11*(2), 127–140. https://doi.org/10.1016/0022-5096(63)90060-7
Hemingway, D. J., & Mittal, T. (2019). Enceladus's ice shell structure as a window on internal heat production. *Icarus*, *332*, 111–131. https://doi.org/10.1016/j.icarus.2019.03.011
Howett, C. J. A., Spencer, J. R., Pearl, J., & Segura, M. (2011). High heat flow from Enceladus' South Polar Region measured using 10–600 cm^{-1} Cassini/CIRS data. *Journal of Geophysical Research*, *116*(E3), E03003. https://doi.org/10.1029/2010JE003718
Hsu, H.-W., Postberg, F., Sekine, Y., Shibuya, T., Kempf, S., Horányi, M., et al. (2015). Ongoing hydrothermal activities within Enceladus. *Nature*, *519*(7542), 207–210. https://doi.org/10.1038/nature14262
Iess, L., Stevenson, D. J., Parisi, M., Hemingway, D., Jacobson, R. A., Lunine, J. I., et al. (2014). The gravity field and interior structure of Enceladus. *Science*, *344*(6179), 78–80. https://doi.org/10.1126/science.1250551
Kamata, S. (2023). *LNTools (version 230406)*. Zenodo. https://doi.org/10.5281/zenodo.7804175
Kamata, S., Matsuyama, I., & Nimmo, F. (2015). Tidal resonance in icy satellites with subsurface oceans. *Journal of Geophysical Research: Planets*, *120*(9), 1528–1542. https://doi.org/10.1002/2015JE004821
Kamata, S., & Nimmo, F. (2017). Interior thermal state of Enceladus inferred from the viscoelastic state of the ice shell. *Icarus*, *284*, 387–393. https://doi.org/10.1016/j.icarus.2016.11.034
Kervazo, M., Tobie, G., Choblet, G., Dumoulin, C., & Behounková, M. (2021). Solid tides in Io´s partially molten interior—Contribution of bulk dissipation. *Astronomy & Astrophysics*, *650*, A72. https://doi.org/10.1051/0004-6361/202039433
Khurana, K. K., Jia, X., Kivelson, M. G., Nimmo, F., Schubert, G., & Russell, C. T. (2011). Evidence of a global magma ocean in Io's interior. *Science*, *332*(6034), 1186–1189. https://doi.org/10.1126/science.1201425
Liao, Y., Nimmo, F., & Neufeld, J. A. (2020). Heat production and tidally driven fluid flow in the permeable core of Enceladus. *Journal of Geophysical Research: Planets*, *125*(9), e2019JE006209. https://doi.org/10.1029/2019JE006209
Longman, I. M. (1963). A green's function for determining the deformation of the Earth under surface mass loads: 2. Computations and numerical results. *Journal of Geophysical Research*, *68*, 485–496. https://doi.org/10.1029/JZ068i002p00485
Love, A. E. H. (1911). *Some problems of geodynamics*. Cambridge University Press.
Matsuyama, I., Beuthe, M., Hay, H. C., Nimmo, F., & Kamata, S. (2018). Ocean tidal heating in icy satellites with solid shells. *Icarus*, *312*, 208–230. https://doi.org/10.1016/j.icarus.2018.04.013
McCarthy, C., & Castillo-Rogez, J. C. (2013). Planetary ices attenuation properties. In M. S. Gudipati & J. Castillo-Rogez (Eds.), *The science of solar system ices* (pp. 183–225). Springer. https://doi.org/10.1007/978-1-4614-3076-6
McKenzie, D. (1984). The generation and compaction of partially molten rock. *Journal of Petrology*, *25*(3), 713–765. https://doi.org/10.1093/petrology/25.3.713
Millero, F. J., Chen, C.-T., Bradshaw, A., & Schleicher, K. (1982). A new high pressure equation of state for seawater. *Marine Geodesy*, *5*(4), 367–370. https://doi.org/10.1080/15210608209379435
Neuman, S. P. (1977). Theoretical derivation of Darcy's law. *Acta Mechanica*, *25*(3–4), 153–170. https://doi.org/10.1007/BF01376989
Pekeris, C. L., & Jarosch, H. (1958). The free oscillations of the Earth. In E. Ingerson (Ed.), *Contributions in geophysics* (Vol. 1, pp. 171–192). Pergamon Press.
Petrenko, V. F., & Whitworth, R. W. (1999). *Physics of ice*. Oxford University Press.
Rice, J. R., & Cleary, M. P. (1976). Some basic stress diffusion solutions for fluid-saturated elastic porous media with compressible constituents. *Review of Geophysics*, *14*(2), 227–241. https://doi.org/10.1029/RG014i002p00227
Roberts, J. H. (2015). The fluffy core of Enceladus. *Icarus*, *258*, 54–66. https://doi.org/10.1016/j.icarus.2015.05.033
Roberts, J. H., & Nimmo, F. (2008). Tidal heating and the long-term stability of a subsurface ocean on Enceladus. *Icarus*, *194*(2), 675–689. https://doi.org/10.1016/j.icarus.2007.11.010
Rovira-Navarro, M., Katz, R. F., Liao, Y., van der Wal, W., & Nimmo, F. (2022). The tides of Enceladus' porous core. *Journal of Geophysical Research: Planets*, *127*(5), e2021JE007117. https://doi.org/10.1029/2021JE007117
Saar, M. O., & Manga, M. (1999). Permeability-porosity relationship in vesicular basalts. *Geophysical Research Letters*, *26*(1), 111–114. https://doi.org/10.1029/1998GL900256
Saito, M. (1974). Some problems of static deformation of the Earth. *Journal of Physics of the Earth*, *22*(1), 123–140. https://doi.org/10.4294/jpe1952.22.123

Saito, M. (1978). Relationship between tidal and load love numbers. *Journal of Physics of the Earth*, *26*(1), 13–16. https://doi.org/10.4294/jpe1952.26.13

Segatz, M., Spohn, T., Ross, M., & Schubert, G. (1988). Tidal dissipation, surface heat flow, and figure of viscoelastic models of Io. *Icarus*, *75*(2), 187–206. https://doi.org/10.1016/0019-1035(88)90001-2

Sharqawy, M. H., Lienhard, J. H., & Zubair, S. M. (2010). Thermophysical properties of seawater: A review of existing correlations and data. *Desalination and Water Treatment*, *16*(1–3), 354–380. https://doi.org/10.5004/dwt.2010.1079

Smylie, D. E., & Mansinha, L. (1971). The elasticity theory of dislocations in real Earth models and changes in the rotation of the Earth. *Geophysical Journal International*, *23*(3), 329–354. https://doi.org/10.1111/j.1365-246X.1971.tb01824.x

Spencer, J. R., Pearl, J. C., Segura, M., Flasar, F. M., Mamoutkine, A., Romani, P., et al. (2006). Cassini encounters Enceladus: Background and the discovery of a south polar hot spot. *Science*, *311*(5766), 1401–1405. https://doi.org/10.1126/science.1121661

Tajeddine, R., Soderlund, K. M., Thomas, P. C., Helfenstein, P., Hedman, M. M., Burns, J. A., & Schenk, P. M. (2017). True polar wander of Enceladus from topographic data. *Icarus*, *295*, 46–60. https://doi.org/10.1016/j.icarus.2017.04.019

Takeuchi, H., & Saito, M. (1972). Seismic surface waves. *Methods in Computational Physics*, *11*, 217–295.

Thomas, P., Tajeddine, R., Tiscareno, M., Burns, J., Joseph, J., Loredo, T., et al. (2016). Enceladus's measured physical libration requires a global subsurface ocean. *Icarus*, *264*, 37–47. https://doi.org/10.1016/j.icarus.2015.08.037

Tobie, G., Mocquet, A., & Sotin, C. (2005). Tidal dissipation within large icy satellites: Applications to Europa and Titan. *Icarus*, *177*(2), 534–549. https://doi.org/10.1016/j.icarus.2005.04.006

Travis, B., & Schubert, G. (2015). Keeping Enceladus warm. *Icarus*, *250*, 32–42. https://doi.org/10.1016/j.icarus.2014.11.017

Waite, J. H., Glein, C. R., Perryman, R. S., Teolis, B. D., Magee, B. A., Miller, G., et al. (2017). Cassini finds molecular hydrogen in the Enceladus plume: Evidence for hydrothermal processes. *Science*, *356*(6334), 155–159. https://doi.org/10.1126/science.aai8703

Watson, G. N. (1966). *A treatise on the theory of Bessel functions*. Cambridge University Press.

Whitaker, S. (1986). Flow in porous media I: A theoretical derivation of Darcy's law. *Transport in Porous Media*, *1*, 3–25. https://doi.org/10.1007/BF01036523